# Autonomous Air-to-Air Refuelling: A Comparison of Control Strategies

by

Jeanne Marie Venter

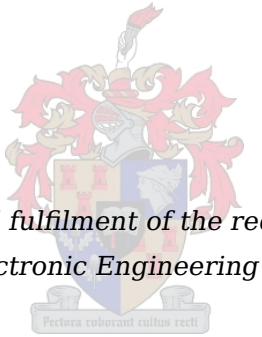


*Thesis presented in partial fulfilment of the requirements for the degree of Master of Science in Electronic Engineering at Stellenbosch University*

Supervisor: Mr JAA Engelbrecht

March 2012

# Declaration

By submitting this thesis electronically, I declare that the entirety of the work contained therein is my own, original work, that I am the sole author thereof (save to the extent explicitly otherwise stated), that reproduction and publication thereof by Stellenbosch University will not infringe any third party rights and that I have not previously in its entirety or in part submitted it for obtaining any qualification.

March 2012

# Abstract

The air-to-air refuelling of large aircraft presents challenges such as a long fuel transfer time, slow aircraft responses and a large distance between the aircraft CG and the receptacle position. This project addresses some of these issues by adding a control system to keep the receiver aircraft in the correct position relative to the tanker to enable fuel transfer.

This project investigates different control strategies which are designed to control the A330-300 during refuelling at one trim condition. The controllers are based on a mathematical aircraft model which was derived from a simulation model received from Airbus.

The first set of controllers uses the aircraft actuators directly. Controllers that are based on the CG dynamics and the receptacle dynamics are compared. Due to the large distance between the CG and the receptacle it was found to be essential to control the receptacle position, and not only the CG position. Also, a controller that is based on a model of the receptacle dynamics performs better.

The second set of controllers uses the aircraft manual control laws as an inner loop controller. This set of controllers and the last direct actuator controller use the same axial controller that uses the engine thrust to control axial position.

It was found that both the direct actuator controller and the manual control laws controller are able to keep the receptacle within the disconnect envelope in moderate turbulence. In both sets of controllers the axial controller fails to keep the receptacle reliably within the disconnect envelope in light turbulence.

From the results it is concluded that both the direct actuator control and manual control laws can be used to successfully control the receptacle position in the normal and lateral positions as long as the receptacle kinematics are included in the control design. Using only the engine thrust for axial control is insufficient. Several recommendations are made to improve the axial control and also how these results can be used in future work.

# Uittreksel

Die lug-tot-lug brandstof hervulling van groot vliegtuie het uitdagings soos ’n lang hervullingstyd, stadige vliegtuig dinamika en ’n groot afstand tussen die hervullingspoort en die vliegtuig massamiddelpunt. Hierdie projek spreek sommige van hierdie uitdagings aan deur ’n beheerstelsel by te voeg wat die vliegtuig in die korrekte posisie relatief tot die tenker hou vir brandstofoordrag om plaas te vind.

Hierdie projek ondersoek verskillende beheerstrategieë wat ontwerp is om die A330-300 te beheer by ’n enkele gestadigde toestand. Die beheerders is gebaseer op ’n wiskundige vliegtuigmodel wat vanaf ’n simulasiemodel afgelei is. Die simulasiemodel is vanaf Airbus verkry.

Die eerste stel beheerders beheer direk die vliegtuig se beheeroppervlakke. Beheerders wat onderskeidelik die massamiddelpunt en die hervullingspoort beheer word vergelyk. Daar is gevind dat dit essensieel is om die hervullingspoort te beheer en nie slegs die massamiddelpunt nie, as gevolg van die groot afstand tussen hierdie twee punte.

Die tweede stel beheerders gebruik die vliegtuig se eie beheerwette as ’n binnelus-beheerder en vorm self die buitelus. Albei stelle beheerders gebruik dieselfde aksiale beheerder wat enjin stukrag gebruik om die aksiale posisie te beheer.

Daar is gevind dat beide stelle beheerders die hervullingspoort binne die ontkoppelings-bestek kan hou in die normale en laterale rigtings tydens matige turbulensie. In beide stelle beheerders is dit die aksiale beheerder wat faal om die hervullingspoort betroubaar in posisie te hou, selfs in ligte turbulensie.

Vanaf die resultate word afgelei dat beide die direkte beheerder en die buitelusbeheerder gepas is om die laterale en normale posisiebeheer toe te pas mits die dinamika van die hervullingspoort in ag geneem word. Om slegs stukrag te gebruik vir aksiale beheer is nie voldoende nie, en verskeie voorstelle word gemaak om die aksiale beheer te verbeter in toekomstige navorsing.

# Contents

# List of Figures

# List of Tables

# Nomenclature

### Abbreviations and Acronyms

| | |
|---|---|
| AAR | Autonomous Aerial Refuelling |
| AoA | Angle-of-attack |
| CAS | Calibrated airspeed |
| CG | Centre of gravity |
| DAC | Direct actuator controllers |
| DOF | Degree-of-freedom |
| DTI | Department of Trade and Industry |
| ESL | Electronic Systems Laboratory |
| FBW | Fly-by-wire |
| FPA | Flight path angle |
| HTP | Horizontal tail plane |
| IRS | Inertial reference system |
| LQR | Linear-quadratic regulator |
| MAC | Mean aerodynamic chord |
| MCL | Manual control laws |
| MIMO | Multi input, multi output |
| MRTT | Multi-Role tanker transport |
| MTOW | Maximum take-off weight |

| | |
|---|---|
| NAC | National Aerospace Centre |
| NED | North-East-Down |
| PI | Proportional integral |
| PIO | Pilot-induced oscillations |
| RMS | Root mean square |
| SISO | Single input, single output |
| SLC | Successive loop closure |
| SSC | Side-stick controllers |
| SU | Stellenbosch University |
| TAS | True airspeed |
| UCT | University of Cape Town |

**Greek Symbols**

| | |
|---|---|
| $\alpha$ | Angle of attack |
| $\beta$ | Angle of side-slip |
| $\delta$ | Control surface deflection |
| $\zeta$ | Place holder angle variable |
| $\theta$ | Pitch angle |
| $\lambda$ | Side stick position |
| $\sigma$ | RMS turbulence intensity |
| $\tau$ | Time constant or thrust |
| $\phi$ | Roll or bank angle |
| $\psi$ | Yaw or heading angle |
| $\omega$ | Angular velocity |

**Lower-case Letters**

| | |
|---|---|
| b | Wingspan |
| g | Gravitational constant |
| l, m, n | Roll, pitch and yaw moment perturbations |
| m | Mass |
| p, q, r | Roll, pitch and yaw rate perturbations |
| s | Laplace variable |
| u, v, w | Axial, lateral and normal velocity perturbations |
| x, y, z | Axial, lateral and normal force perturbations |

**Upper-case Letters**

| | |
|---|---|
| F | Force |
| I | Moment of inertia tensor, or identity matrix |
| K | Feedback gain |
| L | Turbulence scale length |
| L, M, N | Total roll, pitch and yaw moments |
| N | Load factor |
| O | Order of magnitude |
| P, Q, R | Total roll, pitch and yaw rate |
| T | Time constant |
| U, V, W | Total axial, lateral and normal velocity |
| V | Wind velocity |
| X, Y, Z | Axis directions, of forces in those directions |

**Subscripts**

| | |
|---|---|
| a | Aerodynamic (forces and moments) |
| $ail_{in}$, $ail_{out}$ | Inner and outer ailerons |
| B | Body axis system |
| c | Control (forces and moments), or commanded |
| e | Steady state or trim |
| e | Equivalent (Manual control laws) |
| E | Earth axis system |
| elv | Elevator |
| g | Gravitational (forces and moments) |
| HTP | Horizontal tail plane |
| I | Inertial reference frame |
| I | Integral |
| ih | Horizontal tail plane (Manual control laws) |
| lat | Lateral |
| left, right | Engine positions |
| long | Longitudinal |
| R | Rotary reference frame, or Receptacle |
| rud | Rudder |
| sp | Spoilers |
| t | Thrust (forces and moments) |
| u, v, w, p | Axial, lateral, normal and roll (turbulence directions) |
| p | Perturbation |
| p, q, r | Roll, pitch, yaw, or aileron, elevator, rudder (Manual control laws) |

| | |
|---|---|
| x, y, z | X, Y and Z axis directions |

**Syntax and Style**

| | |
|---|---|
| $\boldsymbol{x}$ | The vector $\boldsymbol{x}$ (usually lower-case) |
| $\mathbf{A}$ | The matrix $\mathbf{A}$ (usually upper-case) |
| $\left[\mathbf{I}\right]$ | The Identity matrix |
| $\left[\mathbf{0}\right]$ | The Zero matrix |
| $\mathrm{d}x$ | Differential element $x$ |
| $\frac{\mathrm{d}f}{\mathrm{d}x}$ | Derivative of function, $f$, with respect to $x$ |
| $\frac{\partial f}{\partial x}$ | The partial derivative of function, $f$, with respect to $x$ |

# Acknowledgements

Finishing this project would have been impossible without the help and guidance of Mr Japie Engelbrecht. His support and advice was invaluable and he also did excellent work in coordinating all the different Airbus projects and students.

Thank you to Airbus and the National Aerospace Centre for making this project possible, and for sponsoring this research and the unforgettable visit to Airbus in Toulouse. Thanks also go to the staff from Airbus who was involved in this project, I learned a great deal from them.

The technical discussions with Professor Thomas Jones and Dr Iain Peddle were a great source of inspiration. Thank also go to the other students working on the AAR project for their ideas and friendly help.

Special thanks go to Messrs Chris Jaquet, AM de Jager and Steven Kriel for proofreading this document and their continuous support and friendship.

To my parents and the rest of my family, thank you for always being there for me.

Arno, you are my pillar. Thank you for always believing in me.

And my deepest thanks go to the Creator of all knowledge, from whom I humbly strive to learn...

# Chapter 1

# Introduction and Problem Description

## 1.1 Background

### 1.1.1 Air-to-air Refuelling

Air-to-air refuelling is the process of transferring fuel between two aircraft during flight. It takes place between a tanker and one or multiple receivers, for instance the A330-Multi-Role Tanker Transport (MRTT) aircraft is capable of refuelling three fighter-sized aircraft simultaneously. It is used to extend the range of aircraft, e.g. for transcontinental flights of smaller aircraft or to increase cargo capacity because a smaller fraction of the maximum take-off weight (MTOW) needs to be used for fuel. It is also used in special cases where the airframe needs to reach its operational temperature before the fuel tanks are able to safely contain the fuel which is needed for the mission, which is the case for the SR-71 Blackbird.

There are two types of physical refuelling systems in use today: probe-and-drogue and rigid boom systems.

The probe-and-drogue system consists of a flexible hose which is trailed behind the tanker. The hose is ended off with a basket which is aerodynamically stable and contains the coupling mechanism. The receiver has to position itself to insert a rigid probe into the basket at the end of the hose. Coupling between the aircraft is thus initiated by the receiver. This system is used by large tankers to refuel smaller aircraft and helicopters. It is also used for buddy-to-buddy refuelling between two smaller aircraft, because the hardware needed is compact enough to fit into a pod that can be attached under a wing.

The rigid boom refuelling system uses a rigid instrumented boom which is on the mid line of the tanker. It is hinged at both ends and is also extendible. The boom is equipped


**Figure 1.1** – Artist's representation of two A330 aircraft during refuelling [1].

with aerodynamic control surfaces that enable the boom operator to accurately position the coupling end of the boom. The receiver takes position behind the tanker after which the boom operator directs the boom into the receptacle of the receiver aircraft. Coupling between the aircraft is initiated by die boom operator who is a crew member of the tanker. This type of system is capable of a much higher flow rate than the probe-and-drogue system. It is preferred where a larger amount of fuel needs to be transferred or where the installation of an external probe on the receiver aircraft will have too much negative effect on the aircraft's performance. For example the external shape of the F117 is designed to have very specific radar reflection properties for stealth purposes which will be severely degraded by fitting an external probe.

This project will focus on refuelling between two similarly sized large aircraft using the rigid boom refuelling system as shown in Figure 1.1.

### 1.1.2 National Aerospace Centre Collaboration with Airbus

The National Aerospace Centre (NAC), in collaboration with the Department of Trade and Industry (DTI) and Airbus, proposed a project investigating the possibility of au-

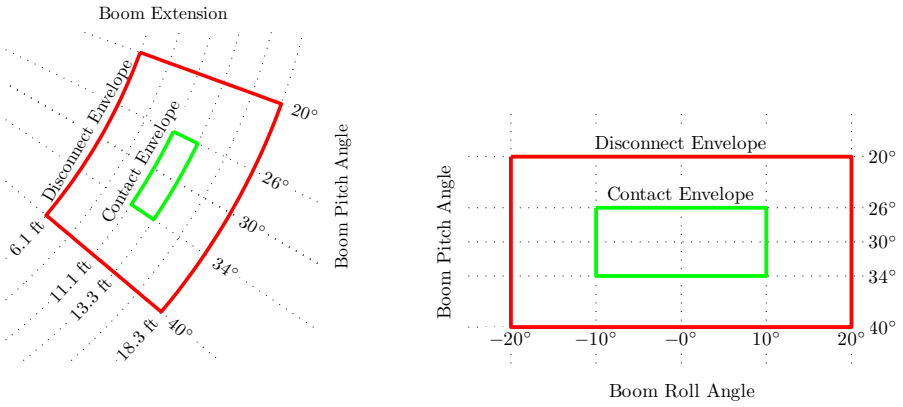


(a) Boom pitch and extension.

(b) Boom pitch and roll angles.

**Figure 1.2** – Specifications of the contact envelope (green) and disconnect envelope (red).

tomating air-to-air refuelling between two large aircraft, more specifically the variants of the Airbus A330. This is one of three Airbus projects managed by the NAC, involving Stellenbosch University and other South African tertiary institutions. The second project is *Control Surfaces in Confined Spaces* [5][6] which investigates methods to reduce actuator size by reducing the aerodynamic hinge moment or by using alternative actuator types, like smart materials. The third project is *Upset Recovery*, in which an aircraft must be returned to its normal flight envelope after being disturbed out of its normal flight domain.

The aim of the Autonomous Air-to-Air Refuelling (AAR) project is to develop techniques and algorithms that enables the automation of air-to-air refuelling between two large aircraft without any changes to the hardware of either aircraft. The designs are tested in simulation using a representative aircraft simulation model which was supplied by Airbus.

The AAR project started in the Electronic Systems Laboratory (ESL) at Stellenbosch University (SU) with a PhD project and this Masters project. The PhD project uses novel control methods to control the receiver aircraft over the entire required flight domain. The focus of this project is controlling the receiver at only one flight condition, but using different control techniques for comparative purposes. Four other Masters projects have started during the course of this project: Estimation of the relative state information of two aircraft during refuelling [7], control using frequency domain disturbance rejection methods, and two projects by students from the University of Cape Town (UCT) investigating the aerodynamic effects that large aircraft have on each other while flying in close proximity.

### 1.1.3 Airbus Requirements for the AAR Project

The following requirements for the automation system were provided by Airbus.

1. The refuelling function must enable the aircraft to:
   a) move from the observation position to the pre-contact position
   b) move from pre-contact to contact position,
   c) stay within the contact envelope until the boom is connected (up to five minutes),
   d) stay within the disconnect envelope until the fuel transfer is complete (up to 20 minutes) and
   e) move back to the pre-contact position after disconnection.
2. These functions must be performed under the following conditions:
   a) Altitude between $10\,000\,\mathrm{ft}$ and $30\,000\,\mathrm{ft}$.
   b) Calibrated airspeed (CAS) between $225\,\mathrm{kts}$ and $300\,\mathrm{kts}$.
   c) Weight between $110\,000\,\mathrm{kg}$ and $230\,000\,\mathrm{kg}$.
   d) Centre of gravity (CG) position between 17% and 41% of the mean aerodynamic chord, measured from the leading edge.
   e) Bank angle up to $25\,^{\circ}$.
   f) Descent rate up to $500\,\mathrm{ft/min}$ (called the Toboggan manoeuvre).
   g) Up to moderate turbulence as defined by MIL-HDBK-1797 [2].
3. The system should be compatible with realistic sensor accuracies and delays. The values for these were not given.
4. The contact and disconnect envelopes are defined in terms of the angular position of the joint between the boom and the tanker and the length that the boom is extended. The two envelopes are illustrated in Figure 1.2.

## 1.2 Problem Description

In this Master's project, the following subtask of the AAR project is addressed: *Investigate the performance of different control strategies in performing the refuelling task.*

The two control strategies that are addressed here are performing the task while controlling the positions of the aerodynamic actuators directly, or performing the task by using the pilots' stick and pedal inputs. In each case the engine thrust is also commanded. The refuelling is performed at an altitude of $20\,000\,\mathrm{ft}$ and an average true airspeed (TAS)

of $352\,\mathrm{kts}$ which is equivalent to a CAS of $251{,}5\,\mathrm{kts}$ at that altitude. Both the tanker and receiver aircraft are A330-300's with a mass of $200\,000\,\mathrm{kg}$ and CG position of 30% of the mean aerodynamic chord (MAC). The task is performed during straight and level flight and a constant banked turn of $20^\circ$ in a calm atmosphere, light turbulence and moderate turbulence as defined in MIL-HDBK-1797 [2]. The advantages and disadvantages of each control strategy are investigated under each flight condition. The assumption is made that all the aircraft data and measurements are available to the controller, therefore no state estimation is required.

## 1.3 Previous Research

Air-to-air refuelling has been used in military applications since the Second World War [8][9], but it was not until the 1980's that refuelling was investigated using analytical methods. This research was motivated by the need for mathematical models of the refuelling scenarios that could be used in simulation software for pilot training [8].

Some of the first in-depth investigations into the aerodynamics of aircraft during refuelling was performed by Bloy et al [10][11][12][13][14]. Their research included the mathematical modelling of the tanker's wing-tip vortices on the receiver aircraft using various modelling techniques. The models were verified with wind tunnel tests using two simplified aircraft models with a similar wingspan. Several combinations of tanker wing shape and receiver stabiliser position were tested. These tests highlighted the need for additional stability and control derivatives to model the aerodynamic behaviour of the receiver aircraft, e.g. roll moment due to lateral offset between the tanker and receiver aircraft. Later advances uses the tanker coordinate system to model the dynamics of the receiver aircraft, thereby reducing the complexity involved in modelling the aerodynamic coupling [15].

An aerodynamic model for the hose-and-drogue system was developed by the NASA Dryden Labs [16]. Although this is interesting research, it cannot be applied to the boom refuelling system as well.

Dogan et al performed research on the flight control design for automated refuelling of a tailless fighter aircraft with innovative control effectors and thrust vectoring [17] using the tanker coordinate system for aerodynamic modelling. Due to the agility and thrust vectoring capabilities of the tailless aircraft the control challenges is very different from this project.

Advanced control methods were performed by Pachter et al [18], using quantitative feedback theory. This is the control method currently being investigated by another student involved in the AAR project.

A study into the potential economic benefits of air-to-air refuelling for commercial aircraft was performed by Bennington and Visser [19], giving some valuable insights into alternative motivations for autonomous air-to-air refuelling.

## 1.4 Project Approach

At the beginning of this project no specific information about the aircraft or refuelling requirements were known. The initial background study was thus very wide.

As soon as the simulation model was received it was analysed in order to fully understand its contents. All the information for the mathematical model had to be extracted from the simulation model, which necessitated a very thorough understanding of the model. The analysis was not trivial, because the Airbus simulation model is much more sophisticated than any aircraft model that has previously been used in the ESL. Other challenges included that most of the block and signal variable names as well as comments and other annotations below the second level of the simulation model were in French. The numerous unit conversions between standard aeronautical (kts and ft), SI and nondimentional values slowed the analysis down considerably.

In the first version of the simulation model the manual control laws were a black box which contents could not be seen directly. A system identification would have had to be performed in order to determine the dynamics of the manual control laws. It was decided to first design controllers that do not use the manual control laws, but control the actuators directly. During the time that these controllers were designed, more information about the manual control laws were received, thus making a system ID unnecessary. The manual control laws still had to be reverse-engineered in order to obtain a mathematical model which is suitable for control system design.

During the project, two main types of controllers were designed: controllers that use the aerodynamic actuators directly, and controllers that use the manual control laws of the aircraft. Within these two main strategies, other comparisons were also made, for instance whether the receptacle kinematics should be modelled or the CG dynamics are sufficient for control purposes. All these investigations were made to identify the direction in which future work of the AAR project should be done.

## 1.5 Thesis Layout

The structure of this thesis is as follows: Chapter 2 provides an overview of the A330 aircraft simulation model that was received form Airbus. This simulation model is used to represent both the tanker and receiver aircraft and to serve as the testing platform for the evaluation of the AAR control algorithms. The next three chapters focus on the

control systems which control the actuators directly. Chapter 3 describes how a mathematical model was derived from the simulation model to serve as the basis for analysis and control system design. Chapter 4 describes the design of the controllers that use direct actuator control while Chapter 5 presents and evaluates the simulation results for the direct actuator controller. Chapters 6 to 8 follow the same structure as Chapters 3 to 5, for the controller that makes use of the pilot inputs. Chapter 6 describes the architecture of the existing manual control laws through which the pilot flies the aircraft. Chapter 7 describes the design of the controller that uses the existing manual control laws. Chapter 8 presents and evaluates the simulation results for the controller that uses the manual control laws. In Chapter 9 a comparison is made between the performances of the direct actuator control and the manual control laws. Chapter 10 presents the conclusions of the research and gives recommendations for future work.

# Chapter 2

# A330 Simulation Model

This project is based on the A330-300 model that was received from Airbus. A thorough understanding of the model is necessary before a control system can be designed for it. Firstly the method in which the model will be used in simulations is explained. Thereafter a general overview of the Simulink model is given. More detail explanations and descriptions of the model follow in the rest of the chapter.

## 2.1 The Refuelling Simulation

To simulate a refuelling scenario, both the tanker and the receiver aircraft need to be simulated. The aerodynamic interaction between the two aircraft is not included in this model and thus cannot be simulated. The tanker aircraft is thus unaffected by the presence of the receiver in this simulation. It was decided to simulate the tanker on its own, and then use the recorded tanker data when the receiver aircraft is simulated. This decreases the processing power required by the simulation, because only one aircraft is simulated at a time. Also, once the tanker data is recorded, it can be re-used for multiple receiver simulations, thus eliminating the need to simulate any given tanker scenario more than once.

For this project, the tanker and receiver aircraft are the same, namely the Airbus A330-300. The same Simulink model was used to simulate the tanker and the receiver aircraft. For the tanker simulations, no modifications were made to the supplied model. The hold modes that are included in the model were used to keep the tanker flying at the required altitude and bank angle. For the receiver aircraft different modifications were made to the model by adding control systems for refuelling. These controllers are discussed in Chapters 4 and 7.

The model that was received is a non-linear simulation model of the Airbus A330-300. It is built in Simulink and makes use of Matlab code and S-functions. It was provided

by Airbus in Toulouse. The model is intended as a platform on which the initial control designs can be tested. If the control systems perform well enough further testing will be performed on the higher fidelity simulation models at Airbus.

The model provides sufficiently accurate results over a wide range of flight conditions. It provides significantly more accurate results than could have been achieved by adapting existing ESL models. This is mainly due to the method used to calculate the aerodynamic forces and moments, which is described in §2.3.

## 2.2 Model Overview

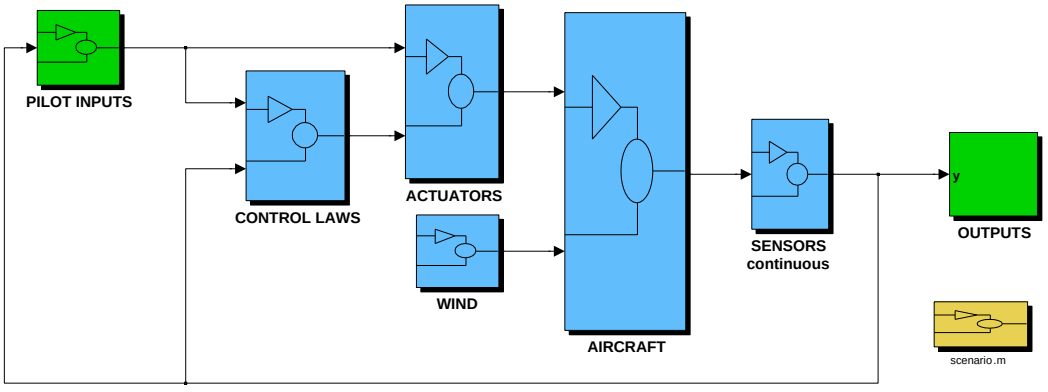


**Figure 2.1** – Top level view of the Simulink model supplied by Airbus.

At the highest level, the Airbus simulation model consists of seven sections, shown in Figure 2.1:

**Aircraft** This section contains all the rigid-body dynamics of the aircraft. The aerodynamic forces and moments are calculated with a neural network. See §3.3.

**Actuators** Each of the aircraft actuators has a unique dynamic response. The actuators receive commands from the control laws, or from the pilot inputs if the control laws are deactivated.

**Sensors** It takes a finite amount of time for the avionics in an aircraft to estimate the velocity, attitude and other dynamic states of the aircraft. These can only be calculated to a certain accuracy, depending on sensor noise and other factors. The sensor and measurement delays are modelled in this block. Measurement inaccuracies are not modelled.

**Wind** The only external influence on the aircraft that is modelled is the air movement present in the atmosphere. Two types of air movement are modelled: wind, which

has a low bandwidth and a non-zero mean, and turbulence which has a higher bandwidth but zero mean velocity. The turbulence can be set up to generate wind inputs that correspond to the light, moderate or severe turbulence levels as defined in MIL-HDBK-1797.

**Control Laws** The control laws of the aircraft translate the stick inputs from the pilot or autopilot into actuator commands. The commands depend on, among other things, the velocity and attitude of the aircraft. All the necessary aircraft measurements are fed back into the control laws block.

**Pilot Inputs** This section represents the pilot or autopilot. This simulation model has three autopilot modes: yaw-hold, side-slip-hold and flight-path-angle-hold mode. These are described in more detail in §2.8. Manual inputs can also be programmed.

**Outputs** The graphical representations of the simulation data are in this block. The measurements are grouped by category and can easily be viewed by opening the relevant Simulink scope.

For ease of use a link to the variable initialisation script is included in the Simulink block diagram. This includes a trimming function.

The first six sections of the simulation model are described in more detail in the rest of this chapter.

## 2.3 Aircraft

The aircraft model consists of three main sections: The force and moment calculations, the six-degree-of-freedom (6-DOF) dynamic equations, and the output calculations.

### 2.3.1 Force and Moment Calculations

The force and moment coefficients are calculated by S-functions implementing a neural network. Each force and moment calculation is represented with a piecewise defined function. The curve fit for each piece of the function has between five and twenty terms, of which each term has the form $(\sum a_i u_i)/(\sum b_i u_i)$ where $u_i$ are all the input variables, $a_i$ are the numerator coefficients and $b_i$ are the denominator coefficients corresponding to each input variable. The numerator and denominator coefficients are unique for each term. In the transition area between two sections the values of the two pieces are linearly interpolated.

The inputs that are used by both the longitudinal and lateral calculations are angle-of-attack, Mach number, altitude, CG position, deflection of each of the four ailerons,

deflection of each of the 12 spoilers and aerodynamic configuration (flap and slat positions). The inputs that are unique to the longitudinal calculations are: side-slip angle (magnitude only), aircraft mass, pitch rate, horizontal tail-plane (HTP) position and elevator deflection. The inputs that are unique to the lateral calculations are: side-slip angle, roll rate, yaw rate and rudder deflection.

### 2.3.2 Aircraft Dynamics

The aircraft dynamics are modelled with standard 6-DOF dynamic equations for a rigid body, using quaternions for the attitude definition. The dynamics can be grouped into four parts: linear velocity, angular velocity, position and orientation quaternions.

Quaternions are used for the attitude calculations since they do not have the same limitations as Euler angles, such as Gimbal lock. This phenomenon and the use of quaternions are explained in [8] or most aircraft dynamics textbooks.

### 2.3.3 Output Calculations

The aircraft states are used to calculate the output variables used by the rest of the simulation. The calculations include unit conversions, conversion from quaternions to Euler angles and airspeed computation. Ten sets containing a total of more than 30 output variables are calculated. All the variables associated with the aircraft dynamics that are used by other sections of the simulation are calculated here.

## 2.4 Actuators

This section models the dynamics between the actuator commands and the physical displacement of the control surfaces. This approximates any intermediate control systems, electrical systems and mechanical actuators. The actuator types are shown in Figure 2.2 and discussed below.

### 2.4.1 Ailerons

These aerodynamic control surfaces are on the trailing edge of the wings, near the wing-tips. Their purpose is to control the rolling movement of the aircraft. The A330-300 has four ailerons, two on each wing. They work together in two sets, the inner and the outer aileron pairs. When a set of ailerons is actuated, the surfaces on the two wings deflect in opposite directions, resulting in a net rolling moment on the airframe. The convention is that a positive command results in a downward deflection of the control surface. When the actuators are paired, the convention is that the positive control

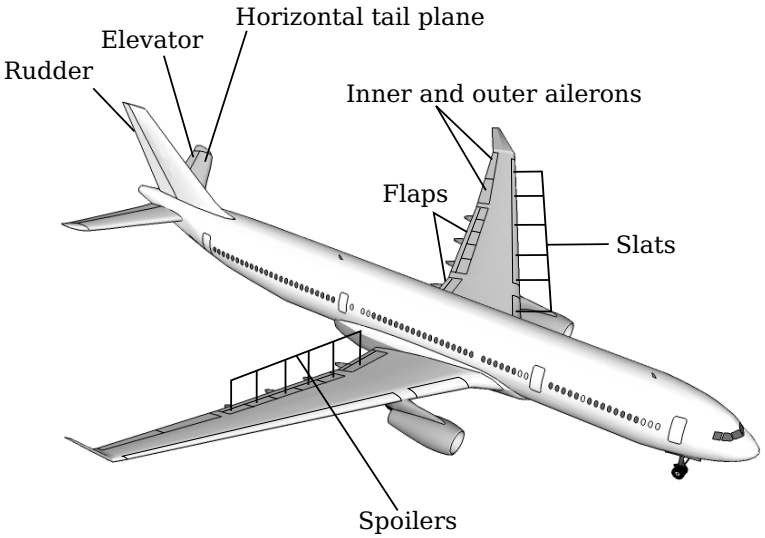


**Figure 2.2** – Aircraft control surfaces.

signal is sent to the aileron on the right-hand wing, while the opposite (negative) of the control signal is sent to the aileron on the left-hand wing, i.e. a positive aileron command results in a negative rolling moment.

The simplified aileron model included in the simulation has the structure shown in Figure 2.3 and consists of the following components:

- First order dynamics approximation with time constant $T$.
- Maximum positive and negative deflection limits. These are the mechanical deflection limits of the control surface independent of airspeed and other parameters.
- Servo slew rate. This is the maximum deflection rate that the control surface can be actuated at.

All the aerodynamic actuators have the same general structure.

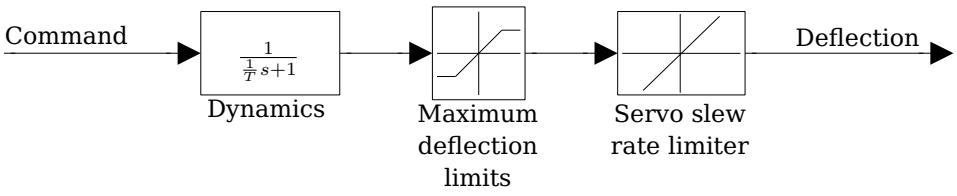


**Figure 2.3** – General representation of an aerodynamic control surface actuator model.

### 2.4.2 Elevator

The elevator is an aerodynamic control surface along the trailing edge of the horizontal tail plane (HTP). It controls the pitching motion of the aircraft. Due to its distance from the aircraft CG it does not need to generate a large force in order to cause a significant pitching moment on the aircraft. A positive elevator command is a downward deflection of the control surface. This leads to an increased lift force on the HTP, which causes a nose-down pitching moment on the aircraft. A positive pitching moment is defined as a nose-up moment, thus a positive elevator deflection leads to a negative pitching moment.

The elevator simulation model has the same structure as shown in Figure 2.3.

### 2.4.3 Rudder

The rudder is the moveable trailing edge of the vertical stabilizer of the aircraft. It generates a yawing moment, allowing the side-slip angle to be controlled. The rudder causes an effective yawing moment due to its long moment arm. A positive rudder deflection is when the control surface is deflected toward the left-hand side of the aircraft. This has a negative yawing moment as a result.

The rudder model has the same structure as shown in Figure 2.3.

### 2.4.4 Horizontal Tail Plane

The angle of the entire HTP can be changed, but by a much smaller amount than any of the other aerodynamic control surfaces. The HTP cannot move quickly enough to control fast pitching movements of the aircraft. The HTP is only used to control the steady-state angle-of-attack and pitching moment of the aircraft. This removes the need for a constant elevator deflection during trimmed flight. Positioning the HTP such that the elevator does not need to be deflected in trimmed flight, results in less aerodynamic drag, making the aircraft more efficient. A positive deflection causes a negative pitching moment. The HTP model shares the structure shown in Figure 2.3 although the range and bandwidth are lower than for other control surfaces.

### 2.4.5 Spoilers

The spoilers are located on the top surface of the wings, between the aircraft fuselage and the ailerons. They are located toward the rear of the wings but do not form part of the trailing edge. They decrease lift and increase drag when deflected. For this reason they are also known as the air brakes. The A330-300 has six spoilers on each wing.

They are used primarily during landing for manoeuvring at low airspeed by causing differential lift and drag on the wings, and also to slow the aircraft down after touchdown. Due to their position on the top surface of the wing, they can only be deflected upwards. This is defined as a negative deflection, similar to the ailerons. The model for each individual spoiler has the structure of Figure 2.3.

### 2.4.6 Flaps and Slats

The flaps and slats together are called the high-lift devices. The flaps form the trailing edge of the wings between the ailerons and the aircraft body. The slats form most of the leading edge of the wing. Together they increase the wing surface area and curvature when extended. This causes more lift while increasing drag. They are used to increase the lift of the aircraft at low speeds, particularly during take-off and landing.

The position of the flaps and slats is known as the high-lift configuration. Configuration 0 is when all the flaps and slats are fully retracted. This is the normal cruising configuration of the aircraft. Configuration 5 is when all the flaps are fully extended. Configurations 1 to 4 are the partial flap extensions that can be selected. The provided Simulink model is only valid for configurations 0 and 4 and does not make provision for any flap position between configuration 0 and configuration 4. The dynamics of the flaps and slats are not modelled. The high-lift configuration is a parameter in the aerodynamic model of the aircraft and will stay constant at the clean configuration for all the simulations used in this project.

### 2.4.7 Engines

The A330-300 has two engines, one underneath each wing. Each engine can be controlled independently. They are also capable of reverse thrust. The engine model that was received from Airbus is a first order approximation consisting of a low pass filter with time constant $\tau = 1{,}5\,\mathrm{s}$ and upper and lower thrust limits. During the course of the project additional engine test data was received, from which another student developed a more accurate non-linear engine model. This model is explained in [4]. This engine model is used in the non-linear simulations contained in this thesis.

The thrust is aligned with the main axis of the aircraft. Thrust therefore only results in a forward force, pitch moment, and yaw moment when differential thrust is used.

## 2.5 Sensors

The Simulink block diagram of the sensors model is shown in Figure 2.4. The inertial reference system (IRS) of the aircraft is located behind the cockpit. Because it is so

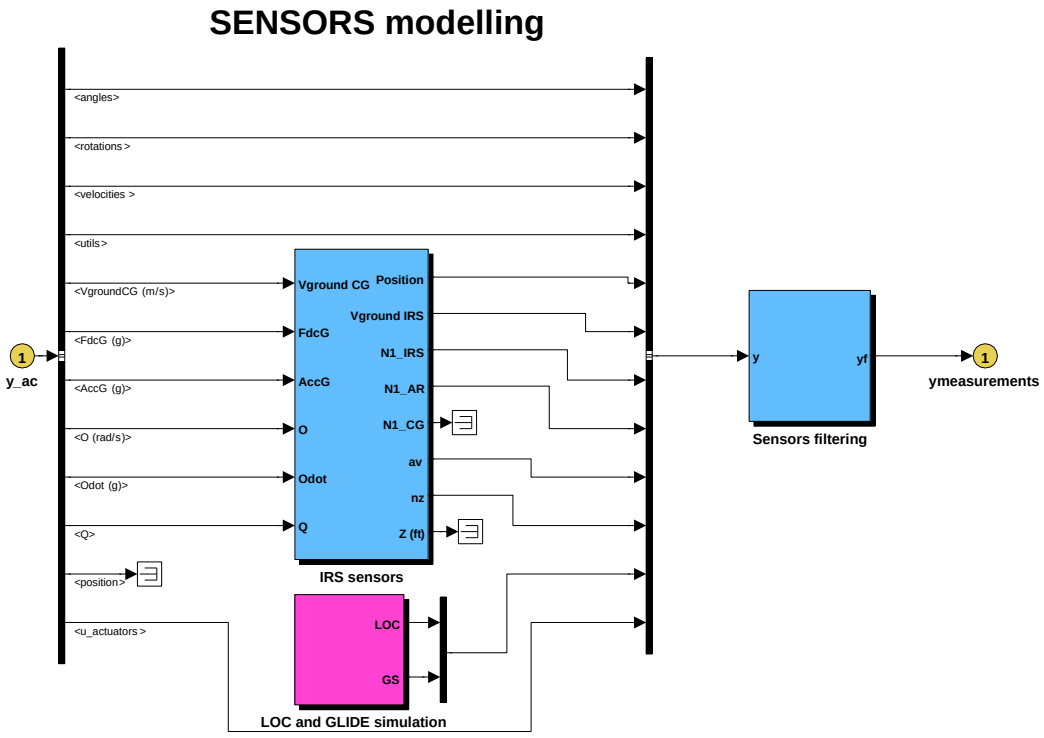


**Figure 2.4** – Contents of the sensor model Simulink block.

far from the CG, the velocity and particularly the accelerations measured at the IRS position are not equal to the velocities and accelerations at the CG. These differences are calculated in the IRS sensors block.

All the signals are filtered by a first order low-pass filter. This smooths the signals and introduces delays that are comparable to the computation delay on the aircraft. The time constants of the filters differ for the various output signals.

The simulation model makes provision for localiser and glide slope information to be included. This is however not implemented in this model.

## 2.6 Wind

A Simulink block that models turbulence was supplied by Airbus. This turbulence block generates wind inputs that correspond to the light, moderate or severe turbulence level as defined in MIL-F-8785C according to the Dryden turbulence model. MIL-HDBK-1797 [2] contains the same turbulence level definitions, but is a more recent document and is therefore used in this project.

When investigating MIL-HDBK-1797 [2] it is seen that turbulence is generated for the

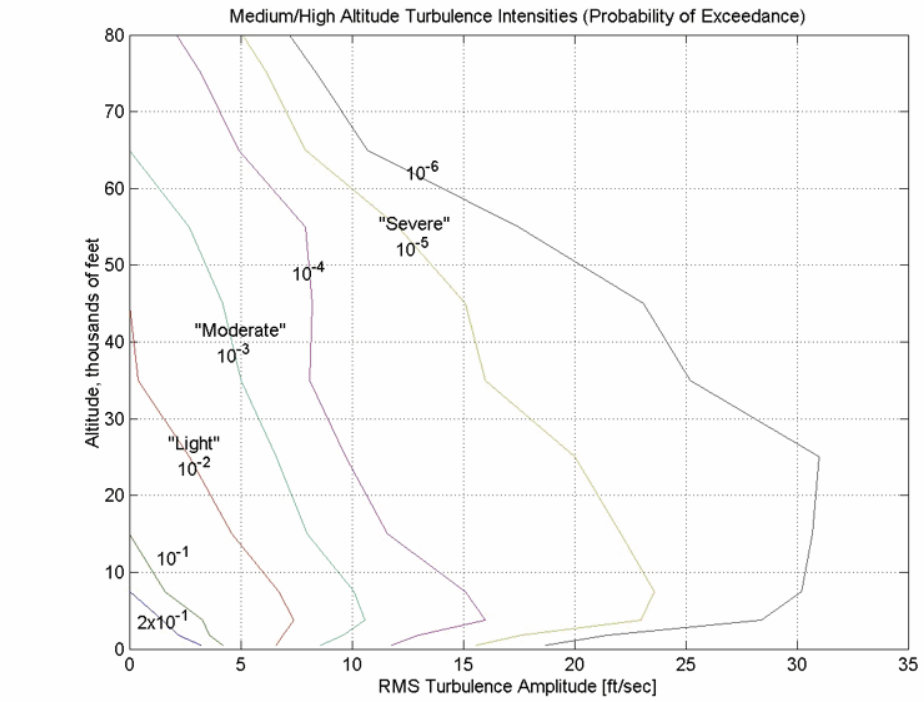


**Figure 2.5** – RMS turbulence intensity as a function of altitude and the probability of that turbulence level being exceeded [2].

simulation by passing band-limited white noise with unity variance through shaping filters. The shaping filters are derived from the spectrum equations, which form part of the Dryden turbulence model. The transfer functions of the shaping filters for axial, normal, lateral, and roll turbulence are given in Equations 2.6.1 to 2.6.4.

$$H_u(s) = \sigma_u \sqrt{\frac{2L_u}{\pi V}} \frac{1}{(1 + \frac{L_u}{V}s)} \tag{2.6.1}$$

$$H_v(s) = \sigma_v \sqrt{\frac{2L_v}{\pi V}} \frac{(1 + \frac{2\sqrt{3}L_v}{V}s)}{(1 + \frac{2L_v}{V}s)^2} \tag{2.6.2}$$

$$H_w(s) = \sigma_w \sqrt{\frac{2L_w}{\pi V}} \frac{(1 + \frac{2\sqrt{3}L_w}{V}s)}{(1 + \frac{2L_w}{V}s)^2} \tag{2.6.3}$$

$$H_p(s) = \sigma_w \sqrt{\frac{0.8}{V}} \frac{(\frac{\pi}{4b})^{1/6}}{(2L_w)^{1/3}(1 + (\frac{4b}{\pi V})s)} \tag{2.6.4}$$

where $\sigma_u, \sigma_v$ and $\sigma_w$ represent the turbulence intensities,

$L_u, L_v$ and $L_w$ represent the turbulence scale lengths,

$b$ and $V$ are the aircraft span and airspeed respectively

and $s$ is the Laplace variable.

The turbulence scale lengths are a characteristic of the frozen turbulence field that forms in the atmosphere, and is a function of altitude. A frozen turbulence field implies that at any specific point in the atmosphere there is a constant air velocity. An object therefore only experiences changes in air velocity due to its own movement through the turbulence field. When using the Dryden model for turbulence with the specifications in MIL-HDBK-1797 these scale lengths are constant for altitude above $2000\,\text{ft}$, and are given by

$$L_u = 2L_v = 2L_w = 1750\,\text{ft} \tag{2.6.5}$$

The turbulence intensities $\sigma_u, \sigma_v$ and $\sigma_w$ are the same in all three directions. The root mean square (RMS) value is a function of altitude and the probability of the turbulence intensity being exceeded. It can be determined from the graph in Figure 2.5.

## 2.7 Control Laws

The control laws, also called the fly-by-wire (FBW) system in this document, are the interface between the pilot or autopilot and the aircraft. It enables the pilot to command aircraft movement such as roll rate or normal load factor, instead of commanding the control surfaces directly. The FBW calculates and commands the appropriate combination of control surface deflections needed to follow the pilot's commands. It also has safety features to prevent the aircraft from entering dangerous flight conditions. The FBW is divided into longitudinal and lateral control. The following two sections explain these control laws in more detail. The kinematics of the control laws are covered in Chapter 6.

### 2.7.1 Longitudinal Control

The longitudinal stick command usually represents a normal load factor command (pulling G's). However, at high angle-of-attack (AoA), the longitudinal stick command is interpreted as an angle-of-attack command instead. There are three protections in the longitudinal control [20]:

**AoA protection** This protects against stall during dynamic manoeuvres or wind gusts. It enables safe and steady flight at high AoA and thus high lift.

**Speed protection** The aircraft is prevented from exceeding its maximum operating velocity by applying a nose-up elevator command. The amount of nose-down that the pilot can command is also reduced at high speed.

**Pitch attitude protection** The pitch attitude of the aircraft is controlled to within certain bounds. This is to keep the aircraft at an attitude at which the previous two protections are effective.

To prevent a steady state elevator deflection, the slow dynamics of the longitudinal command is fed to the horizontal stabilizer. Only the higher frequency commands are fed to the elevator.

### 2.7.2 Lateral Control

The lateral stick commands a roll rate. When the bank angle $\phi \leq 33\,^\circ$, it is maintained when the lateral stick is released. When $\phi > 33\,^\circ$, it returns to $33\,^\circ$ when the stick is released. The bank angle is limited to $\phi = 67\,^\circ$. If the AoA or speed protection is enabled, the bank angle returns to zero when the stick is released, regardless of the commanded bank angle. The maximum bank angle allowed is then also reduced to $\phi = 45\,^\circ$ [20].

The pedals are used to command a side-slip angle.

## 2.8 Pilot Inputs

This block performs the guidance of the aircraft. The simulation can be set up such that the guidance is performed either by manual inputs from the pilot or by the autopilot hold modes.

The inputs that are available to the pilot are longitudinal and lateral side stick, pedals, air brakes, high-lift configuration and thrust. The use of the side stick and pedals commands are explained in §2.7. The other pilot inputs are explained in §2.4.

There are three hold modes included in the Simulink model: flight path angle (FPA) hold, yaw angle hold and side-slip hold. FPA hold mode regulates the flight path angle of the aircraft to a pre-set value by using only the longitudinal stick command as a control signal. Yaw angle hold mode controls the heading by using the lateral stick command. Side-slip hold mode controls the side-slip of the aircraft by using the pedals.

The Pilot Inputs block selects the correct source for the side stick and pedals commands from the manual pilot commands or the hold modes according to which hold modes are activated.

## 2.9 Summary

This chapter described the simulation model of the A330-300 that was received from Airbus. The different sections of the model and how they fit together were explained. This knowledge can now be used to derive a mathematical model of the aircraft in a form that is more suitable to use for control system design. The mathematical model of

the aircraft is derived in Chapter 3 and the mathematical model of the manual control laws is derived in Chapter 6.

# Chapter 3

# A330 Mathematical Model

In this chapter a mathematical model of the A330-300 is derived from the simulation model to obtain a form that is more suitable for analysis and control system design. The dynamics of the aircraft are initially expressed as differential equations derived from Newton's equations of motion. These equations are then linearised and rewritten in state-space form. Finally the dynamics are decoupled into separate models for longitudinal and lateral motion during straight-and-level flight, which can be used for linear control design techniques.

## 3.1 Conventions

The following conventions and assumptions are used when modelling the aircraft:

**Rigid body** Large aircraft, such as the A330-300, are flexible, particularly the wings. Flexibility, however, is not taken into account when modelling the aircraft, because it increases the model's complexity and a rigid body model produces acceptable results. The supplied simulation model does not include flexibility.

**Flat non-rotating earth** The curvature and rotation of the earth plays a role in navigation during intercontinental flights. This project focuses on the positioning of one aircraft relative to another, thus the position of the aircraft relative to the earth is less important. Assuming a flat non-rotating earth is therefore a valid simplification provided that it is used for both aircraft.

### 3.1.1 Axis Definitions

The modelling of the aircraft uses two axis systems: earth axes and body axes. Whilst wind axes is also commonly used in aircraft modelling, this simulation model uses body axes instead.

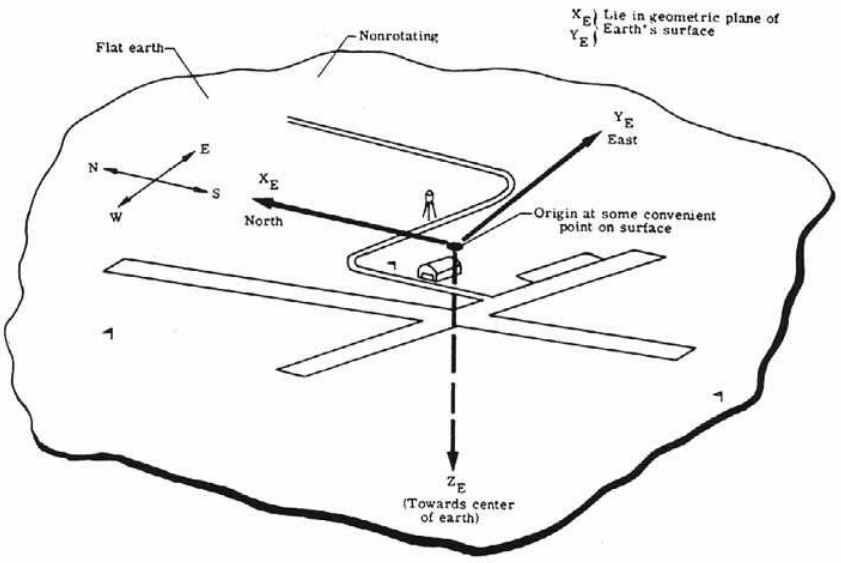


**Figure 3.1** – Earth coordinate system [3].

When using earth axes, the origin lies at any convenient position on the surface of the earth, for example the runway, or beneath the starting position of the aircraft. These axes are aligned so that the first axis ($X_E$) points North, the second axis ($Y_E$) points East, and the third axis ($Z_E$) points downward perpendicular to the other two axes, as shown in Figure 3.1. Gravity is assumed to be in the $Z_E$ direction, which is true for a spherical earth of uniform density. This is a reasonable simplification for the purposes of this project. The three axes form a right-handed axis system known as the NED (North-East-Down) axis system.

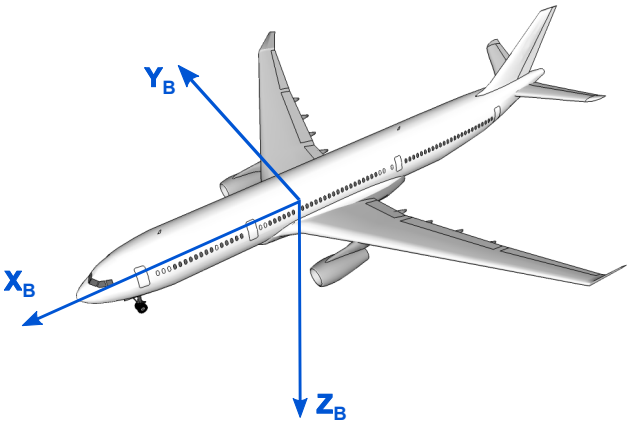


**Figure 3.2** – Aircraft body coordinate system.

The body axis system is shown in Figure 3.2. These axes are fixed to the aircraft with the origin at the aircraft CG. The first axis ($X_B$) is in the plane of symmetry and in line with the aircraft body. The second axis ($Y_B$) is perpendicular to the plane of symmetry and is positive to the right-hand (starboard) side of the aircraft. The third axis ($Z_B$) is also in the plane of symmetry, perpendicular to the other two axes with the positive direction downward to form a right-handed axis system.

Only the aircraft position is coordinated in the earth axes. All the linear and angular velocities are coordinated in body axes.

### 3.1.2 Attitude Definition

The orientation of the body axes relative to the earth axes are represented by a set of three rotations, called the Euler angles. These rotations must be performed in order. The sequence of rotations from the earth axes to the aircraft body axes is 3-2-1: Start with the axes ($X_0$,$Y_0$,$Z_0$) aligned with the earth axes ($X_E$,$Y_E$,$Z_E$). Rotate the axes by the yaw angle $\psi$ around the $Z_0$ axis to get the intermediate axes ($X_1$,$Y_1$,$Z_1$). Rotate these axes by the pitch angle $\theta$ around the $Y_1$ axis to get the second intermediate axes ($X_2$,$Y_2$,$Z_2$). Finally rotate the axes by the roll angle $\phi$ around the $X_2$ axis. These axes

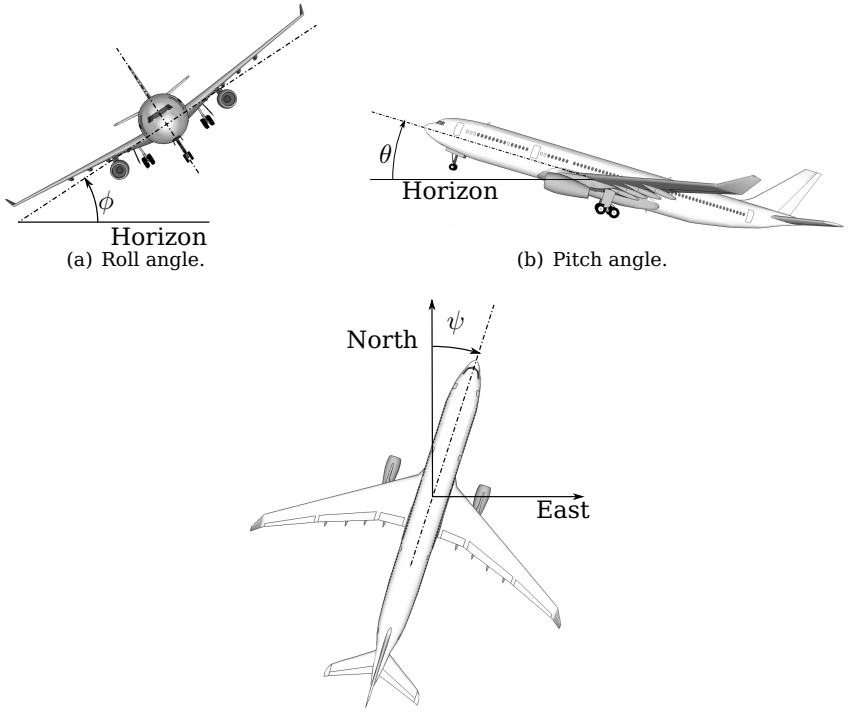


(a) Roll angle.

(b) Pitch angle.

(c) Yaw angle.

**Figure 3.3** – Simplified representation of the three Euler angles.

align with the orientation of the aircraft. A simplified representation of the Euler angles are shown in Figure 3.3.

## 3.2 Dynamic Equations

The different elements needed to build a linear model of the aircraft are explained in this section. The goal is to assemble a state-space model that includes everything that will be controlled. All the building blocks are thus given in a form that resembles the state-space structure. Less manipulation is then needed when the parts of the model are combined into one state-space model.

### 3.2.1 Translational Movement

Newton's second law, when applied to a body of constant mass (m), states that

$$\boldsymbol{F} = m\dot{\boldsymbol{V}}_I \tag{3.2.1}$$

where $\boldsymbol{F}$ is the vector sum of all the external forces applied to the body, and $\boldsymbol{V}_I$ is the velocity of the body referred to an inertial reference frame.

It is desirable to calculate the velocity of the aircraft in components aligned with the aircraft's geometry. The dynamic equations are transformed into a form that includes terms to compensate for the non-inertial reference frame. The relation between the velocity of a body referred to an inertial frame, $I$, and the velocity of the same body referred to a rotating frame, $R$, is

$$\dot{\boldsymbol{V}}_I = \dot{\boldsymbol{V}}_R + \boldsymbol{\omega}_{RI} \times \boldsymbol{V}_R \tag{3.2.2}$$

When Equations 3.2.1 and 3.2.2 are combined, the resulting force equation is

$$\boldsymbol{F} = m(\dot{\boldsymbol{V}}_R + \boldsymbol{\omega}_{RI} \times \boldsymbol{V}_R) \tag{3.2.3}$$

By separating this vector equation into components, the following set of equations for linear translation is obtained:

$$\begin{aligned} m(\dot{U} + QW - RV) &= X_a + X_g + X_c + X_t \\ m(\dot{V} + RU - PW) &= Y_a + Y_g + Y_c + Y_t \\ m(\dot{W} + PV - QU) &= Z_a + Z_g + Z_c + Z_t \end{aligned} \tag{3.2.4}$$

$$\text{where } \boldsymbol{V}_R = \begin{bmatrix} U \\ V \\ W \end{bmatrix}$$

$$\text{and } \boldsymbol{\omega}_{RI} = \begin{bmatrix} P \\ Q \\ R \end{bmatrix}$$

The right-hand side of each equation is the external force that acts on the aircraft along the X, Y and Z axes. The forces are grouped according to their origin: aerodynamics, gravity, control surface deflection or propulsion (thrust). These force groups are denoted by the subscripts $a$, $g$, $c$ and $t$ respectively.

In perturbation form each variable is split into its steady-state (subscript $e$) and perturbation (lower-case) parts, e.g. $Q = Q_e + q$. Each force equation then has the form:

$$\begin{aligned} m(\dot{u} + (Q_e W_e + Q_e w + q W_e + q w) - (R_e V_e + R_e v + r V_e + r v)) \\ = X_{ae} + x_a + X_{g_e} + x_g + X_{ce} + x_c + X_{te} + x_t \end{aligned} \tag{3.2.5}$$

By definition the trim values that are not multiplied with perturbations are balanced and can be removed from both sides of the equation. The products of two or more perturbations are ignored because they are orders of magnitude smaller than the other terms. The remaining terms are rearranged to represent the state-space form more closely by isolating the time derivatives on the left-hand side of the equations.

$$\begin{aligned} \dot{u} &= \frac{1}{m}(x_a + x_g + x_c + x_t) + R_e v - Q_e w - W_e q + V_e r \\ \dot{v} &= \frac{1}{m}(y_a + y_g + y_c + y_t) - R_e u + P_e w + W_e p - U_e r \\ \dot{w} &= \frac{1}{m}(z_a + z_g + z_c + z_t) + Q_e u - P_e v - V_e p + U_e q \end{aligned} \tag{3.2.6}$$

### 3.2.2 Rotational Movement

The rotational movement of a rigid body measured in a rotating axis system is similar in form to Equation 3.2.3.

$$\boldsymbol{M} = \boldsymbol{I}\dot{\boldsymbol{\omega}}_{RI} + \boldsymbol{\omega}_{RI} \times \boldsymbol{I}\boldsymbol{\omega} \tag{3.2.7}$$

where $\boldsymbol{M}$ is the external moments acting on the body, $\boldsymbol{I}$ is the moment of inertia tensor, and $\boldsymbol{\omega}_{RI}$ is the angular velocity of the body relative to an inertial frame.

For a body that is symmetric along the Y-axis, the products of inertia along that axis $I_{xy} = I_{yz} = 0$. The moment of inertia tensor is then:

$$\boldsymbol{I} = \begin{bmatrix} I_x & 0 & I_{xz} \\ 0 & I_y & 0 \\ I_{xz} & 0 & I_z \end{bmatrix} \tag{3.2.8}$$

The angular velocity is split into its components, and then into its steady-state and perturbation terms:

$$\boldsymbol{\omega} = \begin{bmatrix} P \\ Q \\ R \end{bmatrix} = \begin{bmatrix} P_e + p \\ Q_e + q \\ R_e + r \end{bmatrix} \tag{3.2.9}$$

By combining Equations 3.2.7 to 3.2.9 and ignoring second order perturbation terms the component moment equations in perturbation form are

$$\boldsymbol{M} = \boldsymbol{I}\dot{\boldsymbol{\omega}}_{RI} + \boldsymbol{\omega}_{RI} \times \boldsymbol{I}\boldsymbol{\omega}$$

$$\text{with} \quad \boldsymbol{M} = \begin{bmatrix} L_a + l_a + L_g + l_g + L_c + l_c + L_t + l_t \\ M_a + m_a + M_g + m_g + M_c + m_c + M_t + m_t \\ N_a + n_a + N_g + n_g + N_c + n_c + N_t + n_t \end{bmatrix}$$

$$\boldsymbol{I}\dot{\boldsymbol{\omega}}_{RI} = \begin{bmatrix} I_x & 0 & I_{xz} \\ 0 & I_y & 0 \\ I_{xz} & 0 & I_z \end{bmatrix} \begin{bmatrix} \dot{p} \\ \dot{q} \\ \dot{r} \end{bmatrix}$$

$$\boldsymbol{\omega}_{RI} \times \boldsymbol{I}\boldsymbol{\omega} = \begin{bmatrix} I_{xz}\, Q_e & I_{xz}\, P_e - I_y\, R_e + I_z\, R_e & I_z\, Q_e - I_y\, Q_e \\ I_x\, R_e - 2\, I_{xz}\, P_e - I_z\, R_e & 0 & I_x\, P_e - I_z\, P_e + 2\, I_{xz}\, R_e \\ I_y\, Q_e - I_x\, Q_e & I_y\, P_e - I_x\, P_e - I_{xz}\, R_e & -I_{xz}\, Q_e \end{bmatrix} \begin{bmatrix} p \\ q \\ r \end{bmatrix} + \begin{bmatrix} I_{xz}\, P_e\, Q_e - I_y\, Q_e\, R_e + I_z\, Q_e\, R_e \\ I_{xz}\, R_e^2 - I_{xz}\, P_e^2 + I_x\, P_e\, R_e - I_z\, P_e\, R_e \\ I_y\, P_e\, Q_e - I_x\, P_e\, Q_e - I_{xz}\, Q_e\, R_e \end{bmatrix} + O(\delta^2)$$

All the terms that contain the product of two or more perturbations are included in $O(\delta^2)$ and the moments are split into components in a similar way to the forces in Equation 3.2.4.

Since the equation holds true at the chosen trim position where all the perturbation terms and the time derivatives are zero, the steady state terms may be removed from both sides of the equation. The product of any two perturbations is negligible, because it is orders of magnitude smaller than the other terms in the equation. When these simplifications are made, the moment equation can be reduced to:

$$\boldsymbol{M} = \boldsymbol{I}\dot{\boldsymbol{\omega}}_{RI} + \boldsymbol{\omega}_{RI} \times \boldsymbol{I}\boldsymbol{\omega} \tag{3.2.10}$$

$$\text{with} \quad \boldsymbol{M} = \begin{bmatrix} l_a + l_g + l_c + l_t \\ m_a + m_g + m_c + m_t \\ n_a + n_g + n_c + n_t \end{bmatrix}$$

$$\boldsymbol{I}\dot{\boldsymbol{\omega}}_{RI} = \begin{bmatrix} I_x & 0 & I_{xz} \\ 0 & I_y & 0 \\ I_{xz} & 0 & I_z \end{bmatrix} \begin{bmatrix} \dot{p} \\ \dot{q} \\ \dot{r} \end{bmatrix}$$

$$\boldsymbol{\omega}_{RI} \times \boldsymbol{I}\boldsymbol{\omega} = \begin{bmatrix} I_{xz}\,Q_e & I_{xz}\,P_e - I_y\,R_e + I_z\,R_e & I_z\,Q_e - I_y\,Q_e \\ I_x\,R_e - 2\,I_{xz}\,P_e - I_z\,R_e & 0 & I_x\,P_e - I_z\,P_e + 2\,I_{xz}\,R_e \\ I_y\,Q_e - I_x\,Q_e & I_y\,P_e - I_x\,P_e - I_{xz}\,R_e & -I_{xz}\,Q_e \end{bmatrix} \begin{bmatrix} p \\ q \\ r \end{bmatrix}$$

If the trim position is in straight and level flight with $P_e = Q_e = R_e = 0$, the state space form of the moment equations reduces to

$$\begin{bmatrix} \dot{p} \\ \dot{q} \\ \dot{r} \end{bmatrix} = \begin{bmatrix} I_x & 0 & I_{xz} \\ 0 & I_y & 0 \\ I_{xz} & 0 & I_z \end{bmatrix}^{-1} \begin{bmatrix} l_a + l_g + l_c + l_t \\ m_a + m_g + m_c + m_t \\ n_a + n_g + n_c + n_t \end{bmatrix} \tag{3.2.11}$$

## 3.3 Forces and Moments

### 3.3.1 Aerodynamic Forces and Moments

The aerodynamic forces acting on an aircraft are functions of the specific airframe shape, its configuration (e.g. flap position), its control surface deflections, and the linear and angular velocity of the aircraft relative to the surrounding air, represented by the variable groups ($\alpha$,$\beta$, $Mach$) and ($p$, $q$, $r$). The control surface deflections are grouped together as $\boldsymbol{x}_{ctrl}$. The aircraft flaps and landing gear configurations stay constant during the refuelling process, therefore they are considered parameters instead of variables in the function to calculate $\boldsymbol{F}_a$.

$$\boldsymbol{F}_a = f(\alpha, \beta, Mach, p, q, r, \boldsymbol{x}_{ctrl}) \tag{3.3.1}$$

The dynamic equations make use of the deviation of a force or moment from its trim value. This can be determined by integrating the following expression from the trim condition to the current state.

$$\mathrm{d}\boldsymbol{F}_a = \frac{\partial \boldsymbol{F}_a}{\partial \alpha}\mathrm{d}\alpha + \frac{\partial \boldsymbol{F}_a}{\partial \beta}\mathrm{d}\beta + \frac{\partial \boldsymbol{F}_a}{\partial Mach}\mathrm{d}Mach + \frac{\partial \boldsymbol{F}_a}{\partial p}\mathrm{d}p + \frac{\partial \boldsymbol{F}_a}{\partial q}\mathrm{d}q + \frac{\partial \boldsymbol{F}_a}{\partial r}\mathrm{d}r + \frac{\partial \boldsymbol{F}_a}{\partial \boldsymbol{x}_{ctrl}}\mathrm{d}\boldsymbol{x}_{ctrl} \tag{3.3.2}$$

The control surface deflections are grouped together as $\boldsymbol{x}_{ctrl}$. The aircraft flaps and landing gear configurations stay constant during the refuelling process, therefore they are considered parameters instead of variables in the function to calculate $\boldsymbol{F}_a$.

A linear approximation of the deviation of the force from its trim value can be calculated by replacing each partial derivative with its numeric value at the trim position, and approximating the differential of each variable as the perturbation of that variable from its trim value. If only the X-component of the force is considered, then the change in axial force, when ignoring the control surface deflections, is given by

$$\Delta(\boldsymbol{F}_a)_x = \Delta X_a = X_a^{\alpha}\alpha_p + X_a^{\beta}\beta_p + X_a^{Mach}Mach_p + X_a^{p}p_p + X_a^{q}q_p + X_a^{r}r_p \tag{3.3.3}$$

where $X_a^{\alpha}$ is the dimensional value of the partial derivative of axial aerodynamic force with respect to angle-of-attack, calculated at the trim point. The other aerodynamic partial derivatives are defined in a similar manner. The control surface deflections are taken into account in §3.3.2. The change in lateral (Y-direction) and normal (Z-direction) forces are calculated in a similar method as the change in axial force.

The changes in aerodynamic moments are calculated in the same manner, e.g. the change in aerodynamic pitch moment is

$$\Delta M_a = M_a^{\alpha}\alpha_p + M_a^{\beta}\beta_p + M_a^{Mach}Mach_p + M_a^{p}p_p + M_a^{q}q_p + M_a^{r}r_p \tag{3.3.4}$$

In the supplied Simulink model, the aerodynamic forces are calculated by a neural network which has the form of multi variable, piecewise defined functions. The functions were extracted from the simulation model and programmed as symbolic functions using the Matlab Symbolic Toolbox. From there the built-in functions of the Symbolic toolbox was used to determine the partial derivatives of each of these functions and to calculate the numeric values for the partial derivatives at the required trim point.

### 3.3.2 Control Surface Forces and Moments

The change in forces and moments due to the aerodynamic control surface deflections are determined in the same way as described in §3.3.1:

$$\Delta X_c = X_c^{\delta_{ail_{in}}}\delta_{ail_{in}} + X_c^{\delta_{ail_{out}}}\delta_{ail_{out}} + X_c^{\delta_{elv}}\delta_{elv} + X_c^{\delta_{rud}}\delta_{rud} + X_c^{\delta_{HTP}}\delta_{HTP} \tag{3.3.5}$$

$$\Delta M_c = M_c^{\delta_{ail_{in}}}\delta_{ail_{in}} + M_c^{\delta_{ail_{out}}}\delta_{ail_{out}} + M_c^{\delta_{elv}}\delta_{elv} + M_c^{\delta_{rud}}\delta_{rud} + M_c^{\delta_{HTP}}\delta_{HTP} \tag{3.3.6}$$

The control surfaces and their sign conventions are shown in Figure 3.4.

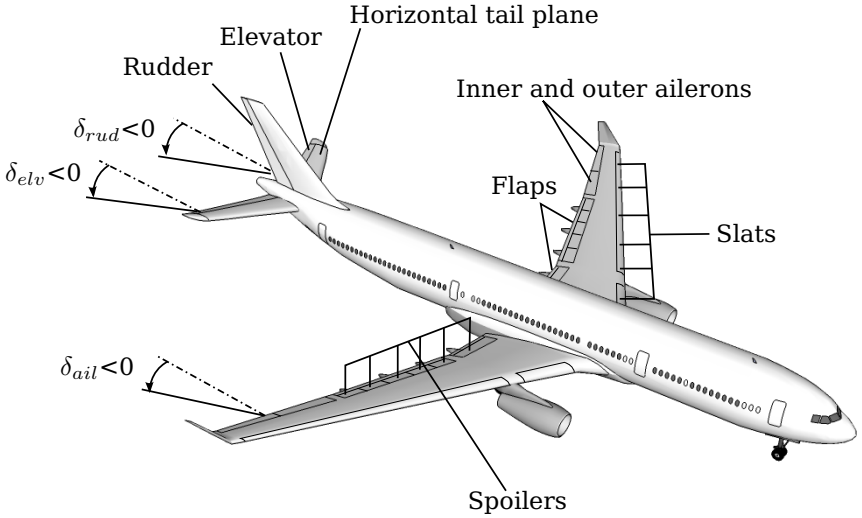


**Figure 3.4** – Aircraft control surfaces showing sign conventions.

### 3.3.3 Gravitational Forces and Moments

Gravity only acts in the positive Z-direction in earth axes. When this is rotated to the aircraft axes by using the Euler 3-2-1 rotation, the result is

$$\mathbf{F}_g = Mass \cdot g \begin{bmatrix} -\sin(\theta) \\ \sin(\phi)\cos(\theta) \\ \cos(\phi)\cos(\theta) \end{bmatrix} \tag{3.3.7}$$

When split into steady-state (e) and perturbation (p) terms, the trigonometric functions become

$$\begin{aligned} \sin(\zeta) &= \sin(\zeta_e)\cos(\zeta_p) + \cos(\zeta_e)\sin(\zeta_p) \\ \cos(\zeta) &= \cos(\zeta_e)\cos(\zeta_p) - \sin(\zeta_e)\sin(\zeta_p) \end{aligned} \tag{3.3.8}$$

In these equations, $\zeta$ can represent any of the Euler angles.

Combine Equations 3.3.7 and 3.3.8 to get

$$\boldsymbol{F_g} = m \cdot g \begin{bmatrix} -\sin(\theta_e)\cos(\theta_p) - \cos(\theta_e)\sin(\theta_p) \\ \big(\sin(\phi_e)\cos(\phi_p) + \cos(\phi_e)\sin(\phi_p)\big)\big(\cos(\theta_e)\cos(\theta_p) - \sin(\theta_e)\sin(\theta_p)\big) \\ \big(\cos(\phi_e)\cos(\phi_p) - \sin(\phi_e)\sin(\phi_p)\big)\big(\cos(\theta_e)\cos(\theta_p) - \sin(\theta_e)\sin(\theta_p)\big) \end{bmatrix} \tag{3.3.9}$$

Applying small angle approximations and grouping constant terms

$$\boldsymbol{F_g} = \boldsymbol{F_{g_e}} + m \cdot g \begin{bmatrix} -\cos(\theta_e)\theta_p \\ \big(\sin(\phi_e) + \cos(\phi_e)\phi_p\big)\big(\cos(\theta_e) - \sin(\theta_e)\theta_p\big) \\ \big(\cos(\phi_e) - \sin(\phi_e)\phi_p\big)\big(\cos(\theta_e) - \sin(\theta_e)\theta_p\big) \end{bmatrix} \tag{3.3.10}$$

and when neglecting the product of two perturbations

$$\boldsymbol{F_g} = \boldsymbol{F_{g_e}} + m \cdot g \begin{bmatrix} 0 & -\cos(\theta_e) \\ \cos(\phi_e)\cos(\theta_e) & -\sin(\phi_e)\sin(\theta_e) \\ -\sin(\phi_e)\cos(\theta_e) & -\cos(\phi_e)\sin(\theta_e) \end{bmatrix} \begin{bmatrix} \phi_p \\ \theta_p \end{bmatrix} \tag{3.3.11}$$

There are no moments due to gravity.

### 3.3.4 Propulsion Forces and Moments

The engine thrust, normalized using the aircraft weight, is given by $\tau_{left}$ and $\tau_{right}$. The resultant force from each engine is in the x-direction only, and is displaced from the body axis origin by $l_{\tau y}$ in the Y-direction, and $l_{\tau z}$ in the Z-direction, as shown in Figure 3.5. This results in the engine thrust causing an axial force, pitch moment and yaw moment, given by

$$\begin{aligned} X_t &= (\tau_{left} + \tau_{right}) \cdot m \cdot g \\ M_t &= (\tau_{left} + \tau_{right}) \cdot m \cdot g \cdot l_{\tau z} \\ N_t &= (\tau_{left} - \tau_{right}) \cdot m \cdot g \cdot l_{\tau y} \end{aligned} \tag{3.3.12}$$

Because the thrust direction is aligned with the aircraft X-axis all the remaining propulsion forces and moments are zero.

$$Y_t = Z_t = L_t = 0 \tag{3.3.13}$$

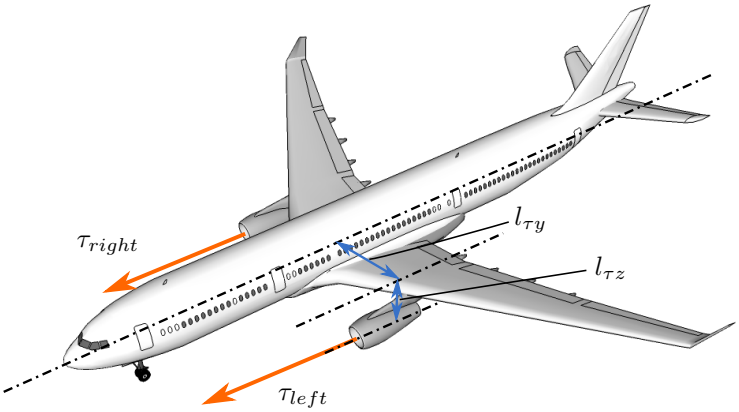


**Figure 3.5** – Engine forces and position.

## 3.4 Receptacle Kinematics

The receptacle is the attachment point where the refuelling boom connects to the receiver aircraft. It is above and slightly behind the cockpit. It is some distance from the aircraft CG, therefore it is not sufficient to model the movement of the CG alone. The movement of the receptacle (R) is related to the movement of the CG of the aircraft body (B) by the following equations:

$$\begin{aligned} \boldsymbol{s_R} &= \boldsymbol{s_B} + \boldsymbol{s_{RB}} \\ \boldsymbol{v_R} &= \boldsymbol{v_B} + \boldsymbol{v_{RB}} \\ &= \boldsymbol{v_B} + \boldsymbol{\omega_B} \times \boldsymbol{s_{RB}} \\ \dot{\boldsymbol{v_R}} &= \dot{\boldsymbol{v_B}} + \dot{\boldsymbol{\omega_B}} \times \boldsymbol{s_{RB}} + \boldsymbol{\omega_B} \times (\boldsymbol{\omega_B} \times \boldsymbol{s_{RB}}) \end{aligned} \tag{3.4.1}$$

The displacement vector $\boldsymbol{s_{RB}}$ is illustrated in Figure 3.6.

As an example, the scalar equations for lateral and normal receptacle velocity in terms of the CG velocity and angular rates are

$$\begin{aligned} v_R &= v_B + l_z p + l_x r \\ w_R &= w_B - l_x q \end{aligned}$$

Because the distance between the CG and the receptacle does not introduce new dynamics, but only kinematics, the receptacle states can be extracted from a state-space model using CG states through a change in the output matrix.

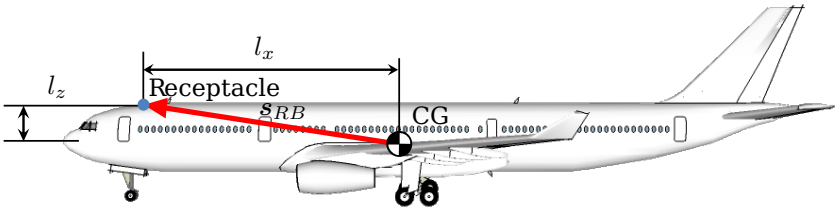


**Figure 3.6** – Position of the receptacle relative to the aircraft CG.

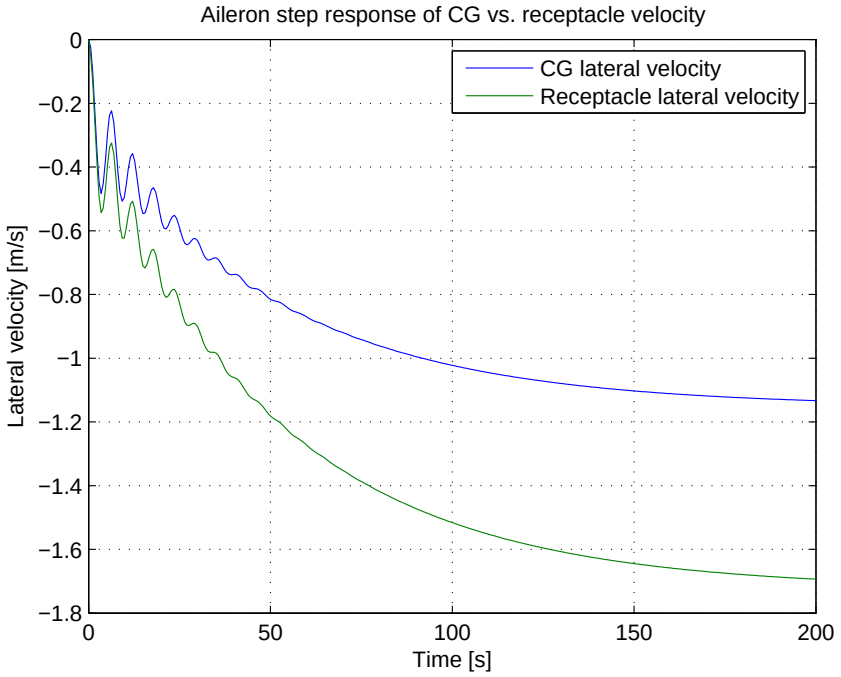


**Figure 3.7** – Lateral velocity response to an aileron step input.

Figure 3.7 shows the lateral velocity response to a step input to the aileron for both the CG and receptacle velocity. The difference between the CG and receptacle velocities that is visible is due to the roll and yaw rates.

## 3.5 State-Space Aircraft Models

State-space models are easily derived from the linearised dynamic equations and can be transformed to other types of models is necessary. In this section the state-space aircraft models for straight-and-level flight and for a constant banked turn are given. Each model is verified against the non-linear model at the trim condition for which is was derived. The model for straight-and-level flight is decoupled into two models containing the longitudinal and lateral dynamics respectively. It is also shown why the

same decoupling cannot be applied as successfully for a model which is derived for a constant banked turn.

### 3.5.1 Coupled Model for Straight-and-Level Flight

The linear dynamics of the A330-300 are modelled with a 9th-order state-space model. The model is only valid at the trim point for which it is calculated. The model in Equation 3.5.1 was calculated for the trim point given in Table 3.1.

$$\begin{aligned} \dot{\boldsymbol{x}} &= \mathbf{A}\boldsymbol{x} + \mathbf{B}\boldsymbol{u} \\ \boldsymbol{y} &= \mathbf{C}\boldsymbol{x} + \mathbf{D}\boldsymbol{u} \end{aligned} \tag{3.5.1}$$

with

$$\mathbf{A} = \begin{bmatrix} 0.0019 & 12.4 & -9.64 & -9.8 & -0.0005 & 0 & -0.0002 & 0 & 0 \\ -0.0005 & -0.525 & 0.99 & -0.002 & 0 & 0 & 0 & -0 & 0 \\ 0.0002 & -0.794 & -0.468 & 0 & 0 & 0 & 0 & 0 & 0 \\ 0 & 0 & 1 & 0 & 0 & 0 & -0 & -0 & 0 \\ 0 & -0 & 0 & 0 & -0.0987 & -0.0488 & 0.992 & -0.0519 & 0 \\ -0 & 0 & -0 & 0 & 4.51 & -1.53 & 0.251 & 0 & 0 \\ 0 & 0 & -0 & 0 & -0.729 & -0.125 & -0.215 & 0 & 0 \\ 0 & 0 & 0 & 0 & 0 & 1 & 0.0379 & 0 & 0 \\ 0 & 0 & 0 & 0 & 0 & 0 & 1 & 0 & 0 \end{bmatrix}$$

$$\mathbf{B} = \begin{bmatrix} 0.0039 & 9.81 & 9.81 & 0 & 0 & 0 \\ -0.0004 & 0 & 0 & 0 & 0 & 0 \\ -0.0208 & 0.108 & 0.108 & 0 & 0 & 0 \\ 0 & 0 & 0 & 0 & 0 & 0 \\ 0 & 0 & 0 & 0 & 0 & -0.0004 \\ 0 & 0.0456 & -0.0456 & -0.02 & -0.0095 & 0.0033 \\ 0 & 0.545 & -0.545 & -0.0007 & 0.0002 & -0.0125 \\ 0 & 0 & 0 & 0 & 0 & 0 \\ 0 & 0 & 0 & 0 & 0 & 0 \end{bmatrix}$$

$$\mathbf{C} = \begin{bmatrix} \mathbf{I} \end{bmatrix}$$

$$\mathbf{D} = \begin{bmatrix} \mathbf{0} \end{bmatrix}$$

$$\text{with } \boldsymbol{x} = \begin{bmatrix} Mach \\ \alpha \\ q \\ \theta \\ \beta \\ p \\ r \\ \phi \\ \psi \end{bmatrix} \qquad \boldsymbol{u} = \begin{bmatrix} \delta_{elv} \\ \tau_{left} \\ \tau_{right} \\ \delta_{ail_{in}} \\ \delta_{ail_{out}} \\ \delta_{rud} \end{bmatrix} \qquad \text{and} \qquad \boldsymbol{y} = \boldsymbol{x}$$

**Table 3.1** – Trim point definition for straight-and-level flight.

| Parameter | Value |
|---|---|
| $\alpha$, $\theta$ | $2{,}9558\,^\circ$ |
| $\beta$ | $0\,^\circ$ |
| Mach | $0{,}5962$ |
| p, q, r | $0\,^\circ/\mathrm{s}$ |
| $\phi$, $\psi$ | $0\,^\circ$ |
| CG Position | $30\%$ of MAC |
| Altitude | $20\,000\,\mathrm{ft}$ |

The aircraft poles for the trim point defined in Table 3.1 are shown in Table 3.2. As is fairly typical for this type of aircraft, the dutch roll mode is extremely under damped. The phugoid mode is unstable near this trim condition.

**Table 3.2** – Pole positions for straight-and-level flight.

| Poles | | | |
|---|---|---|---|
| Position | Freq | Damping | Mode |
| $0.0000$ | $0.0000$ | $-1.0000$ | Yaw angle integrator |
| $-0.0194$ | $0.0194$ | $1.0000$ | Spiral Mode |
| $0.0004 \pm 0.0689i$ | $0.0689$ | $-0.0059$ | Phugoid Mode |
| $-0.4956 \pm 0.8876i$ | $1.0166$ | $0.4875$ | Short Period Mode |
| $-0.0813 \pm 1.0784i$ | $1.0814$ | $0.0752$ | Dutch Roll Mode |
| $-1.6574$ | $1.6574$ | $1.0000$ | Roll Subsidence Mode |

### 3.5.2 Verification of the Coupled Model for Straight-and-Level Flight

Figures 3.9 to 3.10 show the response of the linear and non-linear models due to a $1\,^\circ$ deflection step relative to the trim position of the ailerons, elevator and rudder respectively. In each case, the control surface deflection is held for 10 seconds. The other control surfaces are held at their trim position.

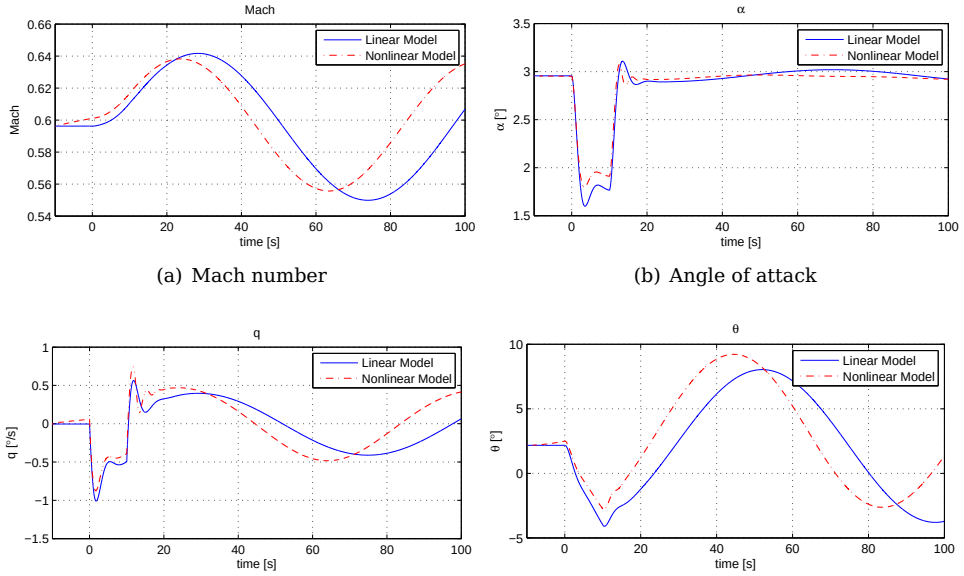


(a) Mach number (b) Angle of attack

(c) Pitch rate (d) Pitch angle

**Figure 3.8** – Linear versus non-linear response due to an elevator input during straight-and-level flight.

When looking at the elevator response in Figure 3.8 there is a noticeable difference between the linear and non-linear dynamics: the frequency of the phugoid mode is not the same for both models causing the linear and non-linear responses to drift away from each other with time. The transient responses correspond well. This linear model is therefore still suitable to use for the controller design as long as the phugoid mode is well damped.

In the aileron response in Figure 3.9 there is a very good correspondence between the linear and non-linear dynamics. Both the transient and the slower dynamics are represented well by the linear model in comparison with the non-linear model in both frequency and damping.

The rudder response of the linear model in Figure 3.10 is very similar to the non-linear response in both the frequency and damping. Overall the similarity between the linear and non-linear responses to the ailerons, elevator and rudder shows that this linear model is a suitable base for control design. It must be kept in mind that the model is only valid for the trim point where it was derived. The larger the difference between the current flight condition and the trim point, the less reliable the linear model is as a representation of the aircraft dynamics.

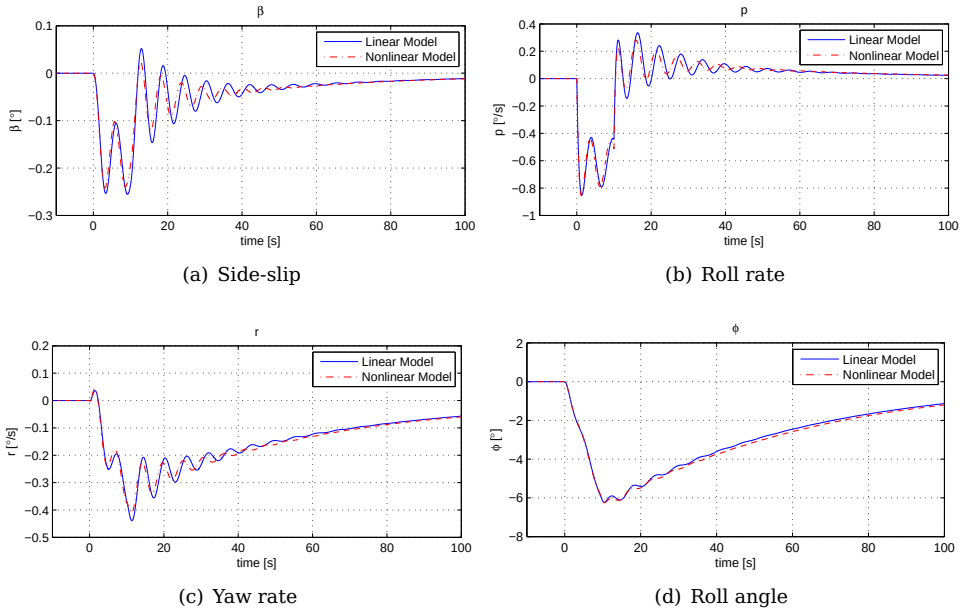


(a) Side-slip (b) Roll rate

(c) Yaw rate (d) Roll angle

**Figure 3.9** – Linear versus non-linear response due to an aileron input during straight-and-level flight.

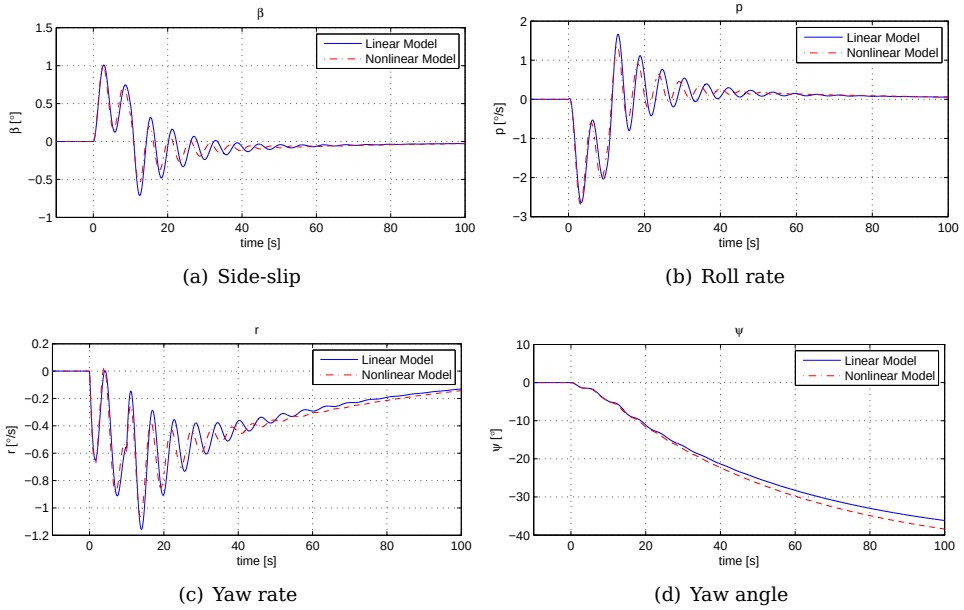


(a) Side-slip (b) Roll rate

(c) Yaw rate (d) Yaw angle

**Figure 3.10** – Linear versus non-linear response due to a rudder input during straight-and-level flight.

### 3.5.3 Decoupled Model for Straight-and-Level Flight

In straight and level flight, the model can be decoupled into longitudinal and lateral dynamics. This simplifies the control design, since the plant that needs to be controlled can be separated into two lower-order sections, instead of one higher-order model.

Longitudinal motion of the aircraft includes all the motion that occurs in the X-Z-plane. This plane is illustrated in Figure 3.11. The longitudinal modes are the phugoid mode and the short period mode. The longitudinal states are:

- Axial velocity ($u$ or $\mathrm{Mach}$)
- Angle of attack ($\alpha$)
- Pitch rate ($q$)
- Pitch angle ($\theta$)

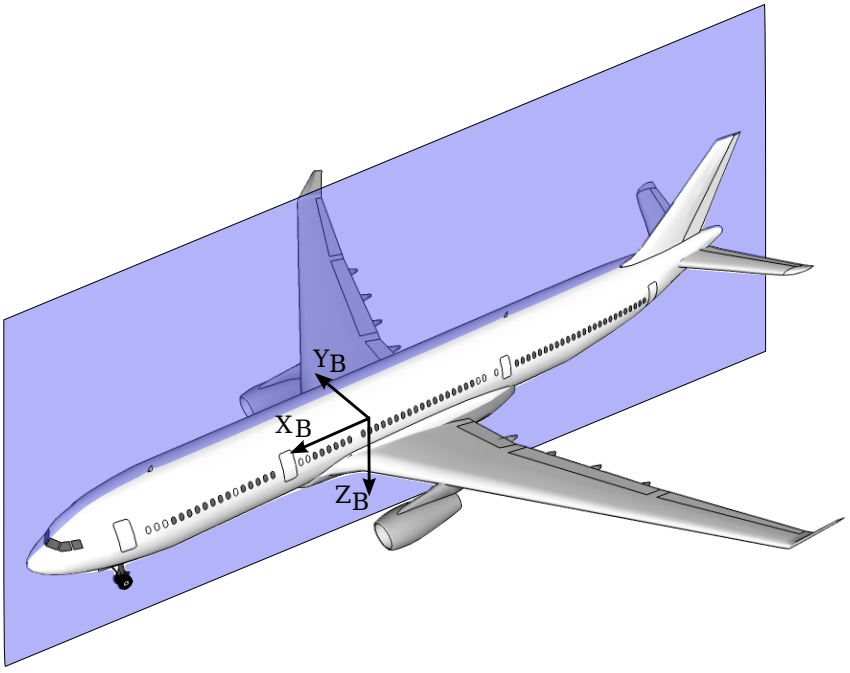


**Figure 3.11** – The X-Z-plane in which longitudinal motion takes place.

Lateral motion is the translational movement in the Y-direction and rotation about the X- and Z-axes. Lateral modes include the Dutch roll mode, the spiral mode, and the roll subsidence mode. The lateral states are

- Angle of side-slip ($\beta$)
- Roll rate ($p$)

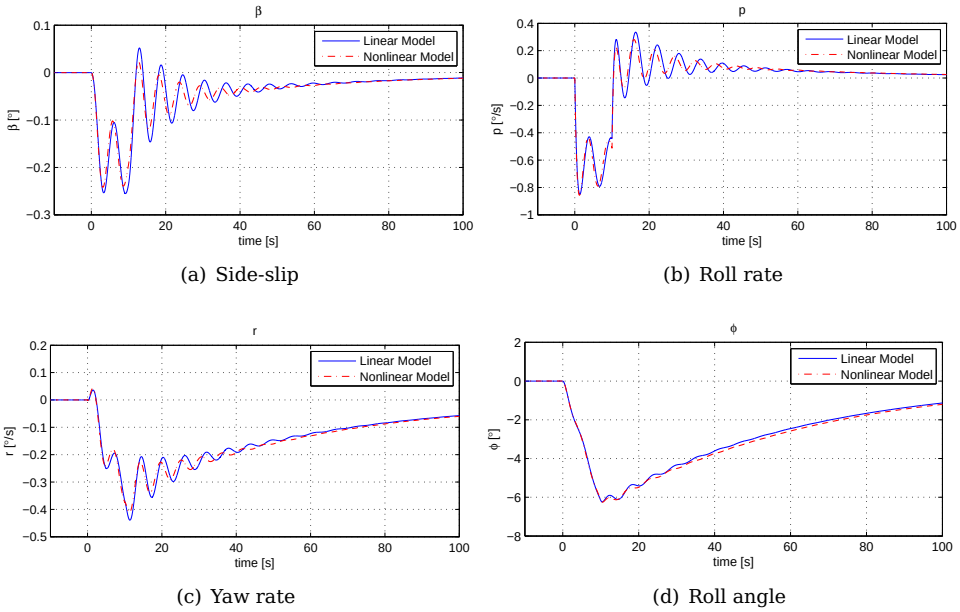


(a) Side-slip (b) Roll rate

(c) Yaw rate (d) Roll angle

**Figure 3.12** – Decoupled linear versus non-linear response due to an aileron input.

- Yaw rate ($r$)
- Bank or roll angle ($\phi$)
- Heading angle ($\psi$)

The heading angle may be omitted because the aircraft dynamics are independent of the aircraft heading. In this model it is included in order to be used for feedback control.

### 3.5.4 Verification of the Decoupled Model for Straight-and-Level Flight

Figure 3.12 shows the response of the decoupled linear and non-linear models due to a $1^\circ$ deflection step relative to the trim position of the ailerons. The responses to the elevator and rudder can be seen in Figures A.1 and A.2 in Appendix A. The correspondence between the linear and non-linear response is similar to that with the coupled model. This means that the control system design process can be simpler because the reduced order decoupled models can be used for the design.

### 3.5.5 Coupled Model for a Constant Banked Turn

For a different trim point, a new model is calculated. See Equation 3.5.2 for a model trimmed at a constant bank angle as defined in Table 3.3. The state, control and output

vectors are the same as defined in Equation 3.5.1.

$$\begin{aligned} \dot{\boldsymbol{x}} &= \mathbf{A}\boldsymbol{x} + \mathbf{B}\boldsymbol{u} \\ \boldsymbol{y} &= \mathbf{C}\boldsymbol{x} + \mathbf{D}\boldsymbol{u} \end{aligned} \tag{3.5.2}$$

with

$$\mathbf{A} = \begin{bmatrix} 0 & 14.8 & -16.7 & -9.78 & 3.48 & 0 & 1.53 & 0 & 0 \\ -0 & -0.547 & 0.99 & -0.0036 & 0.0015 & -0.0078 & 0 & 0.0173 & 0 \\ 0.0006 & -0.551 & -0.488 & 0 & 0 & -0.018 & -0 & 0 & 0 \\ 0 & 0 & 0.937 & 0 & 0 & 0 & 0.349 & 0.0189 & 0 \\ -0.0001 & -0.0015 & 0 & -0.0014 & -0.095 & -0.0822 & 0.99 & -0.0465 & 0 \\ 0 & 0 & 0.0183 & 0 & 5.05 & -1.6 & 0.315 & 0 & 0 \\ 0 & 0 & 0.0006 & 0 & -0.632 & -0.157 & -0.173 & 0 & 0 \\ 0 & 0 & -0.0272 & -0.019 & 0 & 1 & 0.0732 & 0 & 0 \\ 0 & 0 & -0.35 & -0.0015 & 0 & 0 & 0.94 & 0 & 0 \end{bmatrix}$$

$$\mathbf{B} = \begin{bmatrix} 0.0072 & 9.81 & 9.81 & 0 & 0 & 0 \\ -0.0004 & 0 & 0 & 0 & 0 & 0 \\ -0.0221 & 0.108 & 0.108 & 0 & 0 & 0 \\ 0 & 0 & 0 & 0 & 0 & 0 \\ 0 & 0 & 0 & 0 & 0 & -0.0004 \\ 0 & 0.0456 & -0.0456 & -0.0208 & -0.01 & 0.0033 \\ 0 & 0.545 & -0.545 & -0.0006 & 0.0001 & -0.0116 \\ 0 & 0 & 0 & 0 & 0 & 0 \\ 0 & 0 & 0 & 0 & 0 & 0 \end{bmatrix}$$

$$\mathbf{C} = \begin{bmatrix} \mathbf{I} \end{bmatrix}$$

$$\mathbf{D} = \begin{bmatrix} \mathbf{0} \end{bmatrix}$$

$$\text{with } \boldsymbol{x} = \begin{bmatrix} Mach \\ \alpha \\ q \\ \theta \\ \beta \\ p \\ r \\ \phi \\ \psi \end{bmatrix} \qquad \boldsymbol{u} = \begin{bmatrix} \delta_{elv} \\ \tau_{left} \\ \tau_{right} \\ \delta_{ail_{in}} \\ \delta_{ail_{out}} \\ \delta_{rud} \end{bmatrix} \quad \text{and} \quad \boldsymbol{y} = \boldsymbol{x}$$

The aircraft poles for the trim point defined in Table 3.3 are shown in Table 3.4.

**Table 3.3** – Trim point definition for a banked turn.

| Parameter | Value |
|---|---|
| $\alpha$ | $4{,}8785\,^\circ$ |
| $\beta$ | $0{,}4454\,^\circ$ |
| Mach | $0{,}6521$ |
| p | $0{,}0842\,^\circ/\mathrm{s}$ |
| q | $0{,}3772\,^\circ/\mathrm{s}$ |
| r | $-1{,}0123\,^\circ/\mathrm{s}$ |
| $\phi$ | $-20{,}41\,^\circ$ |
| $\theta$ | $4{,}4636\,^\circ$ |
| CG Position | $30\%$ of MAC |
| Altitude | $20\,000\,\mathrm{ft}$ |

**Table 3.4** – Pole positions during a constant banked turn.

| | Poles | | |
|---|---|---|---|
| Position | Freq | Damping | Mode |
| $0.0000$ | $0.0000$ | $-1.0000$ | Yaw angle integrator |
| $-0.0112$ | $0.0112$ | $1.0000$ | Spiral Mode |
| $0.0001 \pm 0.0915i$ | $0.0915$ | $-0.0012$ | Phugoid Mode |
| $-0.5153 \pm 0.7447i$ | $0.9056$ | $0.5690$ | Short Period Mode |
| $-0.0827 \pm 1.1078i$ | $1.1109$ | $0.0744$ | Dutch Roll Mode |
| $-1.6927$ | $1.6927$ | $1.0000$ | Roll Subsidence Mode |

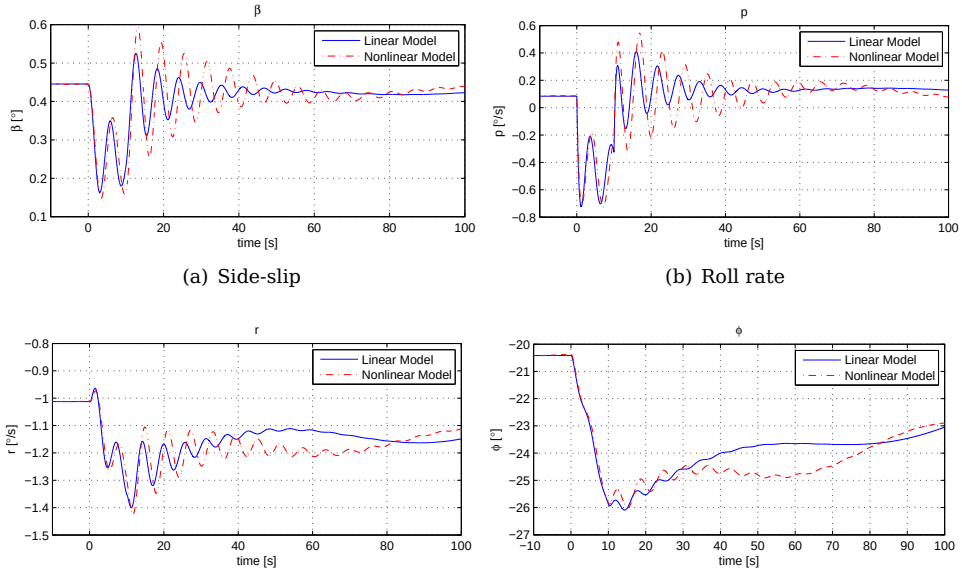


(a) Side-slip (b) Roll rate

(c) Yaw rate (d) Roll angle

**Figure 3.13** – Linear versus non-linear response due to an aileron input during a constant banked turn.

### 3.5.6 Verification of the Coupled Model for a Constant Banked Turn

Figure 3.13 shows the response of the linear and non-linear models due to a $1^\circ$ deflection step relative to the trim position of the ailerons during a constant banked turn. The other control surfaces are held at their trim position. The transient response corresponds well, but the amplitude of the dominant resonant mode is too small in the linear model. In the yaw rate and roll angle responses the slow phugoid mode can be seen as well. This is because the lateral and longitudinal dynamics become coupled when the aircraft is not flying straight-and-level. The elevator and rudder responses show a similar trend and can be seen in Figures A.3 and A.4 in Appendix A.

### 3.5.7 Decoupled Model for a Constant Banked Turn

When the aircraft is in a constant banked turn, some of the aircraft dynamics will be lost if the linear model is decoupled, due to the coupling of the non-zero steady-state angular rates. This can be seen in the bold coupling terms of the coupled matrix in Equation 3.5.7:

$$\mathbf{A} = \begin{bmatrix} 0 & 14.8 & -16.7 & -9.78 & \mathbf{3.48} & \mathbf{0} & \mathbf{1.53} & \mathbf{0} & \mathbf{0} \\ -0 & -0.547 & 0.99 & -0.0036 & \mathbf{0.0015} & \mathbf{-0.0078} & \mathbf{0} & \mathbf{0.0173} & \mathbf{0} \\ 0.0006 & -0.551 & -0.488 & 0 & \mathbf{0} & \mathbf{-0.018} & \mathbf{-0} & \mathbf{0} & \mathbf{0} \\ 0 & 0 & 0.937 & 0 & \mathbf{0} & \mathbf{0} & \mathbf{0.349} & \mathbf{0.0189} & \mathbf{0} \\ \mathbf{-0.0001} & \mathbf{-0.0015} & \mathbf{0} & \mathbf{-0.0014} & -0.095 & -0.0822 & 0.99 & -0.0465 & 0 \\ \mathbf{0} & \mathbf{0} & \mathbf{0.0183} & \mathbf{0} & 5.05 & -1.6 & 0.315 & 0 & 0 \\ \mathbf{0} & \mathbf{0} & \mathbf{0.0006} & \mathbf{0} & -0.632 & -0.157 & -0.173 & 0 & 0 \\ \mathbf{0} & \mathbf{0} & \mathbf{-0.0272} & \mathbf{-0.019} & 0 & 1 & 0.0732 & 0 & 0 \\ \mathbf{0} & \mathbf{0} & \mathbf{-0.35} & \mathbf{-0.0015} & 0 & 0 & 0.94 & 0 & 0 \end{bmatrix} \tag{3.5.3}$$

For this reason the model which is derived for a constant banked turn is not decoupled.

## 3.6 Engine Model

In the Simulink model that was received from Airbus, each aircraft engine, including its controller, is modelled as a low bandwidth low pass filter as shown in Figure 3.14.

During the project, data for the engine thrust response was received. An example of the trust response is shown in Figure 3.15. The following main characteristics can be seen in practical engine thrust test data:

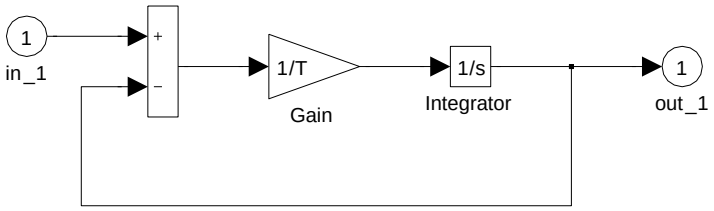


**Figure 3.14** – Original simplified engine model

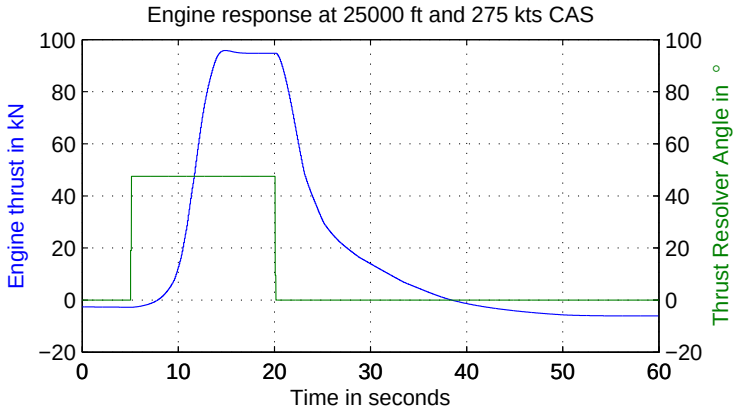


**Figure 3.15** – Engine response data.

- There is a noticeable lag before the thrust output starts responding to a commanded step in thrust.
- When a large increase in thrust is commanded, the output thrust quickly reaches a maximum slew-rate.
- When the thrust is decreased, it is also limited by a maximum rate, but the maximum rate of thrust decrease is much slower than the maximum rate of thrust increase. This is because the engine is not actively braked, therefore the the rotor decelerates slower than it accelerates.

In [4] the practical engine data was used to derive a non-linear engine model. This model was used for the simulations in this project. Refer to Appendix B for the block diagram of the non-linear engine model.

For the control design, the linear engine model was used to perform the initial design, after which the designs were adapted to work with the non-linear model in simulation.

## 3.7 Summary

In this chapter the linear aircraft dynamic models that are used for the control system design were developed. The dynamics of these models were compared with the non-linear aircraft simulation models and the transient dynamics correspond sufficiently for use in the control system design in Chapter 4.

# Chapter 4

# Direct Actuator Control Design

During this project two different approaches to the refuelling control task were followed. One of the aims of this project is to compare the performance of these two approaches.

The first approach is to control the receiver aircraft by using the aerodynamic actuators directly. The refuelling controller thus replaces the manual control laws and the hold mode controllers.

The second approach is to control the receiver aircraft using the same inputs that are available to the pilot. The refuelling controller thus replaces only the hold mode controllers while the inner loop control is still performed by the manual control laws.

This chapter discusses the design of the controllers that use the actuators directly, also referred to as the Direct Actuator Controllers (DAC).

## 4.1 Design Strategy

The first DAC was designed using state-space methods. During this stage of the project only the first-order engine model was available. The aircraft model was split into the longitudinal and lateral dynamics. MIMO pole placement was performed separately for the longitudinal and the lateral control. These controllers controlled the position of the receiver's CG relative to the mid-position of the tanker's boom. The position of the receptacle relative to the CG was added to the boom mid-position, thereby calculating the required receiver CG position. For this calculation a constant orientation was assumed for the receiver aircraft.

The first controller was improved by discarding the assumption of a constant trim orientation for the receiver. Instead, the position error or the receptacle was used to command a differential CG position, e.g. if the receptacle was one unit to the left of the

boom mid position, the CG is commanded to move one unit to the right. This improved the steady-state accuracy of the receptacle position, but introduced unmodelled kinematics for which the controller was not specifically designed.

The final improvement to the first controller was to include the receptacle kinematics in the model and repeating the control design. The result was two MIMO controllers, one each for longitudinal and lateral control, that control the position of the receiver's receptacle.

At that stage of the project engine data was received from which a co-student derived a non-linear engine model which was more representative of the A330-300 engines than the linear model which was used up to this point. When the receptacle controller was tested using the non-linear engine model the resulting system was unstable. Therefore a new controller that works with the non-linear engine model was needed.

The longitudinal dynamic model of the receiver was further separated into axial and normal dynamic models. For each of these models a SISO controller was designed: axial position was controlled using only thrust, and normal position was controlled using only the elevator. The lateral dynamics of the aircraft were not changed by the non-linear engine model because differential thrust is never used. The lateral position controller was therefore kept the same.

## 4.2 Longitudinal MIMO CG Control

### 4.2.1 Velocity Control

The first controller that was developed controls the longitudinal motion of the aircraft CG. It is based on a linear state-space model consisting of the normal and axial (X- and Z-directions) dynamics, combined with the first-order model of the engine dynamics, as described in Chapter 3. The states included in this model are

- Axial velocity ($u$)
- Angle of attack ($\alpha$)
- Pitch rate ($q$)
- Pitch angle ($\theta$)
- Thrust ($\tau$)

All these states are perturbations from the steady state values.

The state-space aircraft model was augmented with the integrals of axial velocity and normal velocity errors. This is to achieve zero steady-state errors for axial and normal velocity when full-state feedback is performed.

- Axial velocity error integral ($\int err_u$)
- Normal velocity error integral ($\int err_w$)

After experimenting with successive loop closure (SLC) and linear-quadratic regulator (LQR) controllers, it was found that pole placement using full state feedback gives satisfactory results. The closed loop pole positions were chosen iteratively, using the following requirements:

- The real pole of the engine dynamics is not moved to reduce the excitation of unmodelled non-linear dynamics.
- The short period mode poles are not moved to reduce the required control effort [21].
- The rest of the poles are placed on the real axis in the left half plane to ensure a stable response without overshoot. In general the non-linear response has less damping than the linear response.

The open-loop and closed-loop poles for axial and normal velocity control are shown in Table 4.1 and Figure 4.1.

**Table 4.1** – Pole placement for longitudinal control

| (a) | | | (b) | | |
|---|---|---|---|---|---|
| Open Loop Poles | | | Closed Loop Poles | | |
| Eigenvalue | $\zeta$ | $\omega_n$ | Eigenvalue | $\zeta$ | $\omega_n$ |
| $0$ | $1$ | $0$ | $-2$ | $1$ | $2$ |
| $0$ | $1$ | $0$ | $-2$ | $1$ | $2$ |
| $0.0004 \pm 0.0689i$ | $-0.006$ | $0.0689$ | $-1.25$ | $1$ | $1.25$ |
| | | | $-1.25$ | $1$ | $1.25$ |
| $-0.4$ | $1$ | $0.4$ | $-0.4$ | $1$ | $0.4$ |
| $-0.496 \pm 0.888i$ | $0.487$ | $1.02$ | $-0.496 \pm 0.888i$ | $0.487$ | $1.02$ |

### 4.2.2 Position Control

The longitudinal control was completed by commanding a differential axial velocity that is proportional to the axial position error, and commanding a differential normal velocity that is proportional to the normal position error. The resulting structure is shown in Figure 4.2.

In non-linear simulations it was assumed that the receiver aircraft will always settle to one trim condition since the tanker flies at a constant velocity and altitude. A change in the position of the receptacle then results in the same change in the position of the

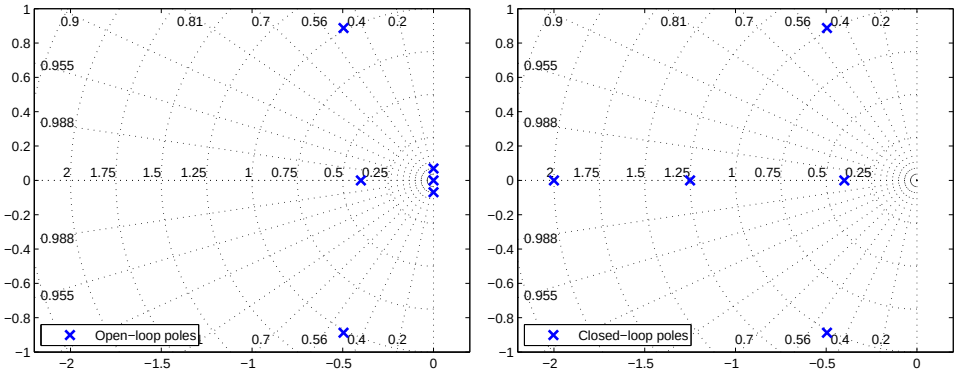


(a) Open-loop poles (b) Closed-loop poles

**Figure 4.1** – Pole positions for longitudinal control of the CG.

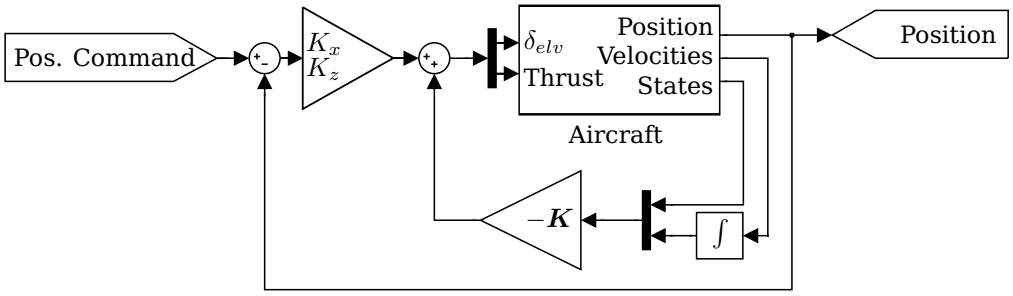


**Figure 4.2** – Structure of CG MIMO controller.

CG in the steady state. Therefore, the position error in the simulation is measured at the receptacle, even though the model on which the controller is based does not model the relative motion between the aircraft CG and receptacle.

The step response in axial and normal position command are shown in Figure 4.3 and Figure 4.4. The responses of the linear and non-linear models are shown. In both cases the command is followed with a zero steady state error. This shows that the integral control succeeds in eliminating any steady state error. The axial step command is within 5% of the reference after 16s and has 10% overshoot. The response time in the axial direction is limited severely by the response time of the engines. In order to minimise the control effort needed in axial control, it is essential that the normal and lateral controllers cause a minimal disturbance in the axial direction. The normal controller is capable of following a 10m step in normal position within 10s with less than $3\%$ overshoot. A more aggressive controller could be designed, but in Figure 4.4 it can be seen that this controller already causes a significant disturbance in axial position, which is only resolved after 30s.

This controller was improved by repeating the pole placement on the aircraft model that includes the receptacle kinematics. This formed the basis of the next controller. Preliminary simulation results for different turbulence conditions are shown in Appendix C.

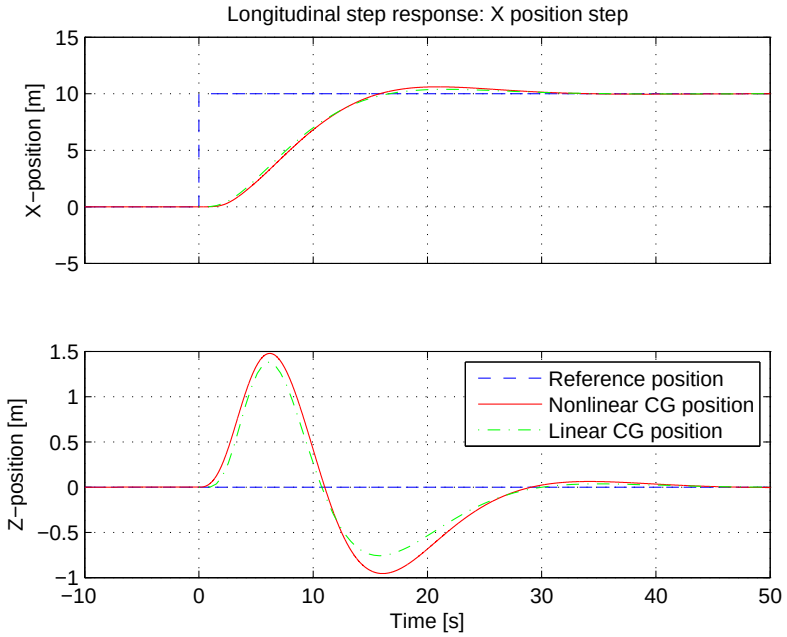


**Figure 4.3** – Response to a 10m axial position step.

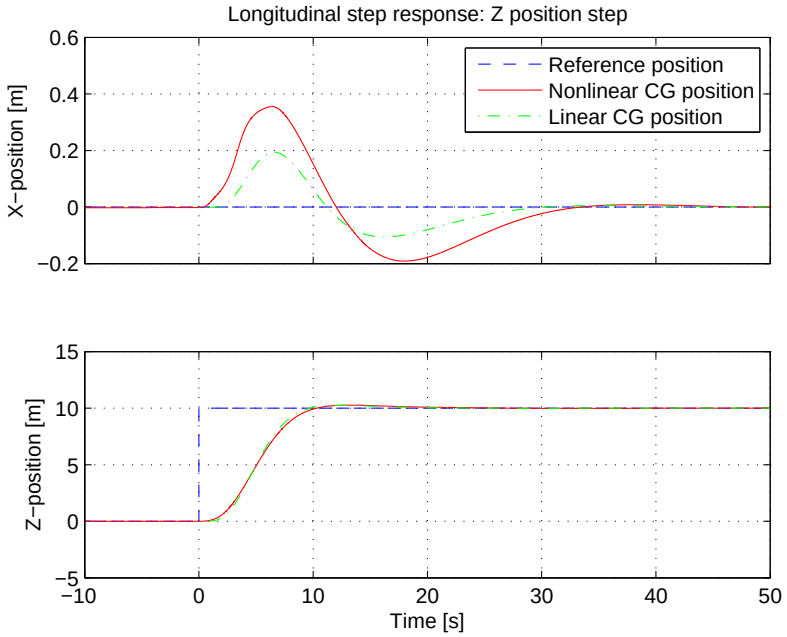


**Figure 4.4** – Response to a 10m normal position step.

After the more accurate engine model became available the longitudinal controller using the linear engine model was not developed further.

## 4.3 Longitudinal SISO Receptacle Control

The fuel receptacle is in front of and above the aircraft CG, therefore any angular velocity of the aircraft will result in a difference in the linear velocity of the CG and the receptacle. A change in aircraft attitude will result in a change of the receptacle position relative to the CG when measured in earth axes. A controller based on an aircraft model that includes the receptacle kinematics will thus have an advantage over a controller based on a model of only the CG movement since it eliminates the need to assume a constant trim orientation.

The controller that was described in the previous section was not able to produce a stable response with the non-linear engine model. The longitudinal control was therefore separated into normal control and axial control, and a SISO controller was designed for each direction.

### 4.3.1 Normal Control

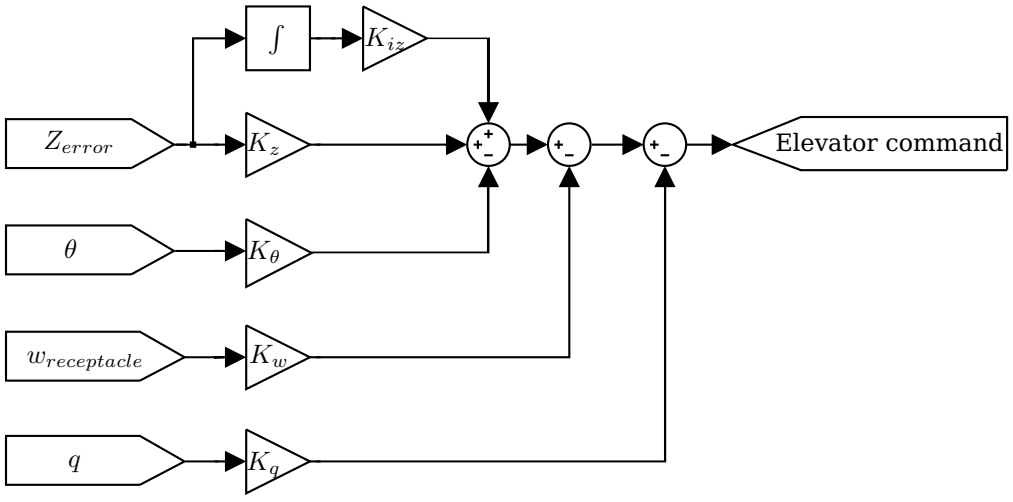


**Figure 4.5** – Structure of the normal controller.

A controller with the structure shown in Figure 4.5 was designed to control the normal velocity of the receptacle. Initially a successive loop closure design process was followed. It had the restriction that the resulting system after each loop closure must be stable and that there must be time-scale separation between the loops. Due to these

restrictions, the performance of the controller was compromised: the position error was much larger than the error of the CG controller described in §4.2.

In order to improve the performance of the receptacle velocity controller, the feedback gains were based on the CG controller's gains. The elements of the full-state feedback gain matrix $\mathbf{K}_{Long}$ corresponding to the angle of attack, pitch rate, and pitch angle feedback to elevator, were transformed to feedback gains corresponding to the receptacle states, by using the state transformation matrix $\mathbf{T}$:

$$\begin{bmatrix} K_{w_{rec}} & K_q & K_\theta \end{bmatrix} = \begin{bmatrix} K_{Long}(\delta_e, \alpha) & K_{Long}(\delta_e, q) & K_{Long}(\delta_e, \theta) \end{bmatrix} \mathbf{T}^{-1} \tag{4.3.1}$$

where $\mathbf{T}$ is defined by $\begin{bmatrix} w_{rec} \\ q \\ \theta \end{bmatrix} = \mathbf{T} \begin{bmatrix} \alpha \\ q \\ \theta \end{bmatrix}$ resulting in

$$\begin{bmatrix} K_{w_{rec}} & K_q & K_\theta \end{bmatrix} \begin{bmatrix} w_{rec} \\ q \\ \theta \end{bmatrix} = \begin{bmatrix} K_{Long}(\delta_e, \alpha) & K_{Long}(\delta_e, q) & K_{Long}(\delta_e, \theta) \end{bmatrix} \begin{bmatrix} \alpha \\ q \\ \theta \end{bmatrix}$$

The resulting feedback control system had similar characteristics to the normal control section of the MIMO controller on which it was based.

Position control were achieved with a PI controller feeding the normal velocity command from the normal position error. The gains were iterated to get a fast stable response of the non-linear system with minimal overshoot.

Figure 4.6 shows the response to a $10\,\mathrm{m}$ normal position step. The receptacle position overshoots by $22\%$ and is within $10\%$ of its final position after $12\,\mathrm{s}$. The steady-state error is zero. The axial and normal dynamics of the aircraft is coupled. During this manoeuvre the error in axial position is always less than $0.65\,\mathrm{m}$. This shows that the controller is capable of controlling the normal position without causing a large disturbance of the axial position.

### 4.3.2 Axial Control

Thrust is directly proportional to axial acceleration through mass, therefore having thrust control is similar to having acceleration control. The thrust response of the aircraft is very non-linear (see §3.6). It was therefore decided to implement and iterate a simple PI-controller for axial velocity control, with only the gains $K_i$ and $K_p$, instead of doing a non-linear-control design. Position control is then achieved by translating the positional error into a differential velocity command by multiplying it with the gain $K_x$.

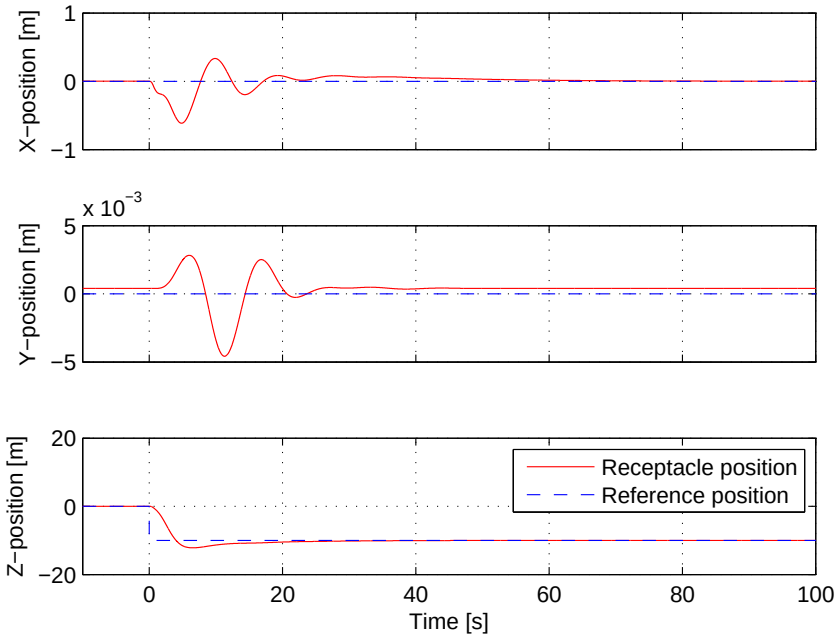


**Figure 4.6** – Non-linear response to a $10\,\mathrm{m}$ normal position step.

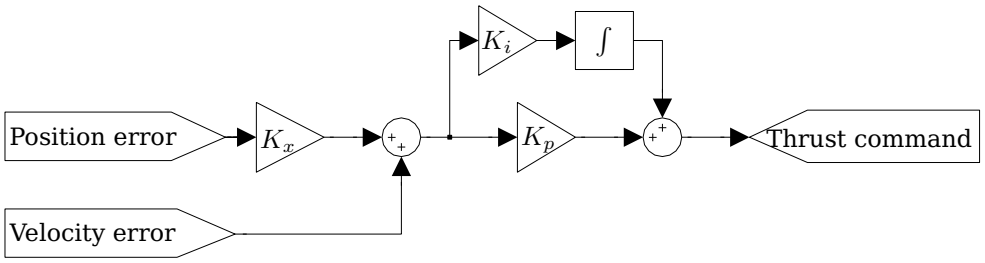


**Figure 4.7** – Structure of the axial controller.

The structure of the controller is shown in Figure 4.7. Figure 4.8 shows the response to a $10\,\mathrm{m}$ step in axial position. This controller is able to follow a $10\,\mathrm{m}$ step in axial position within $12\,\mathrm{s}$ with overshoot of less than $20\,\%$. After the overshoot, it takes another $30\,\mathrm{s}$ for the position to stay within $5\,\%$ of the commanded position, however the steady-state error is zero as a result of integral control. This controller has a minimal disturbance on the other axes.

Many of the engines' natural characteristics can be seen in this step response. There is a noticeable delay before the engines start responding, but once they do, the position error improves fairly quickly. The slow decay of the error is exaggerated by the asymmetrical response of the engines.

When the position step in the opposite direction, shown in Figure 4.9, is compared to the previous step response, the effects of the asymmetrical engine response can be seen. The response delay is more than in the positive step and also the overshoot is less

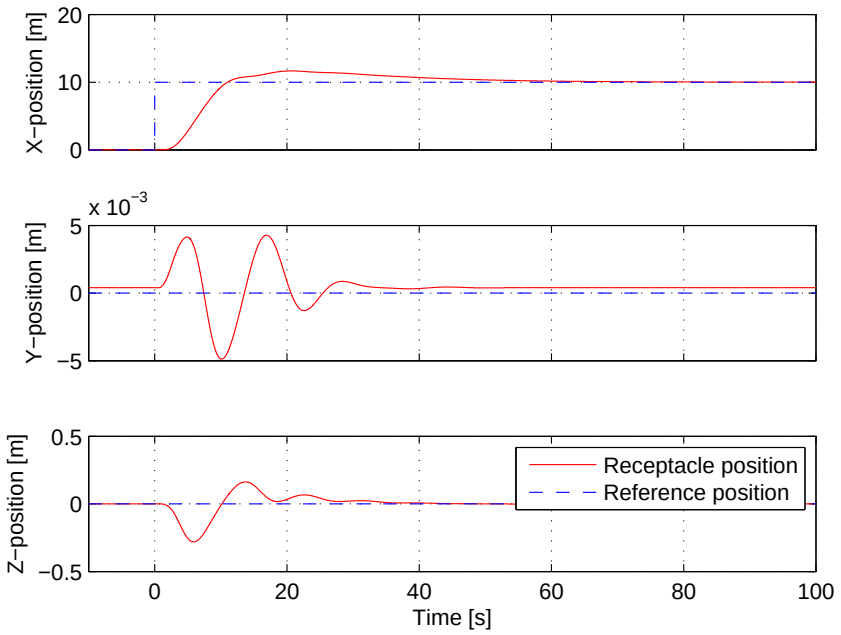


**Figure 4.8** – Non-linear response to a $10\,\mathrm{m}$ axial position step.

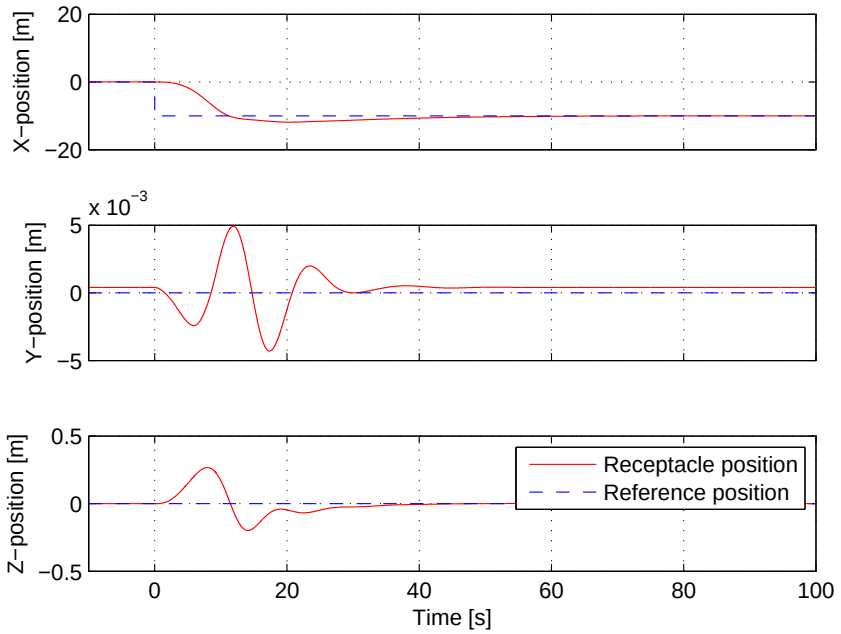


**Figure 4.9** – Non-linear response to a negative axial position step.

and decays quicker, due to the faster engine response in that direction.

## 4.4 Lateral Control

Lateral control of the receptacle is performed by a controller using a SLC structure. The feedback gains are multiplied with the feedback signals instead of with the error signals, which is the more familiar SLC structure. It is possible to transform these SLC forms between each other. They are equivalent in terms of degrees-of-freedom and what control is possible using this structure. The gains are chosen in this position for the following reasons:

1. The control input is independent of the order in which the loops are closed.
2. The same output can be fed back multiple times. This has the same result as feeding that output back only once with the gain equal to the sum of the multiple feedback gains.
3. The effect of a change in each gain on the closed loop system can be visualised with a root locus because of the previous two characteristics.

The controller's structure is shown in Figure 4.10

In the first section of this controller the yaw rate is fed to the rudder in order to damp the Dutch roll mode. The feedback signal is first passed through a high-pass filter. This isolates the transients of the yaw rate to damp the Dutch roll mode without the rudder counteracting a constant banked turn [22].

Figure 4.11 shows the response to a $10\,\mathrm{m}$ step in lateral position. It reaches a position within $10\%$ of the reference position in less than $6\,\mathrm{s}$. The step causes a $1\,\mathrm{m}$ disturbance in the normal position of the receptacle. This is because the aircraft banks in order to follow the lateral position step. As the aircraft banks its lift becomes misaligned with gravity, and subsequently the aircraft loses altitude. The influence on the axial position is less than $0.15\,\mathrm{m}$ for the given lateral step.

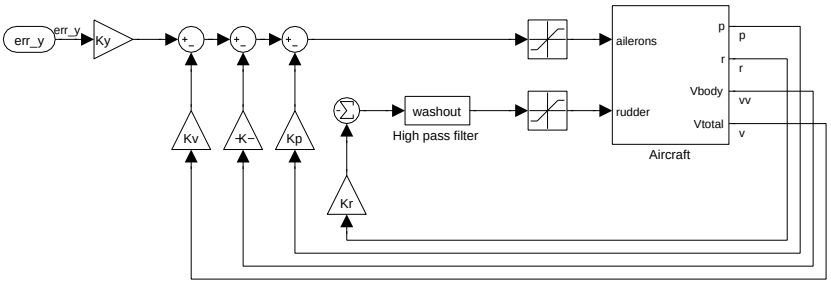


**Figure 4.10** – Structure of the lateral controller.

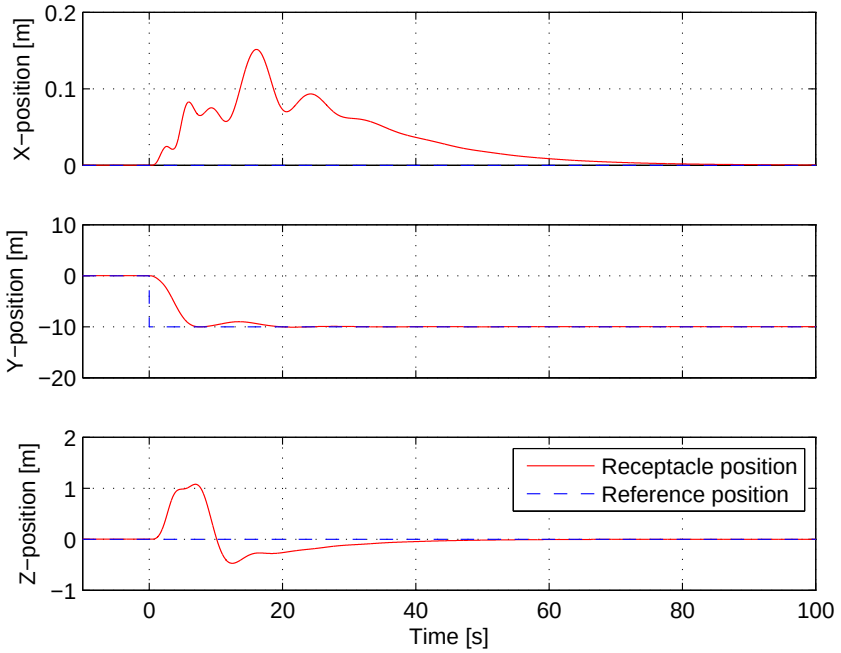


**Figure 4.11** – Non-linear response to a $10\,\mathrm{m}$ lateral position step.

## 4.5 Summary

In this chapter the design of the set of controllers that directly command the aerodynamic actuators is explained. The dynamics of the aircraft with this set of control systems is analysed in the form of pole positions and the response to various position step commands are evaluated. In Chapter 5 the performance of this set of controllers is tested in non-linear simulations of various refuelling scenarios.

# Chapter 5

# Direct Actuator Control Simulations

The purpose of the controllers that were developed in the previous chapter is to keep the receptacle in the correct position for fuel transfer to take place. The best way that is available to evaluate the performance of the controllers is to have the controllers perform the task in simulation. The controllers are evaluated using the non-linear Simulink simulation in a still air, light turbulence and moderate turbulence.

In the non-linear simulation, the only external disturbance that influences either aircraft is the wind. In the absence of wind there is nothing that will make the aircraft deviate from their correct relative position. The step responses in §4.3 already show that the receiver aircraft is able to follow position commands with zero steady-state error in a calm atmosphere. Those results are therefore not repeated in this chapter.

The controllers are tested in light and moderate turbulence. The results are shown and discussed in §5.3 and §5.4 respectively. The techniques and parameters that are used to simulate and evaluate the performance of the controllers are discussed in the next sections.

## 5.1 Simulation Procedure

In order to perform a refuelling simulation, data from both the tanker and receiver aircraft is needed. The simulation model which was received from Airbus does not contain a model of the aerodynamic interaction of the two aircraft on each other. Because the focus of this project is on the control systems necessary for refuelling, it was decided not to include the aerodynamic interaction between the two aircraft and solve the kinematic problem first. The inclusion of the aerodynamics interactions is left as future work.

## 5.2 Statistical Analysis

In this project the turbulence requirements have probabilistic attributes: In the Dryden model for turbulence, the turbulence level is defined by probability: At any time, at any point in the atmosphere, Light turbulence has a 1% chance of being exceeded, and Moderate turbulence has a 0.1% chance of being exceeded.

This dependence of the turbulence on statistics means that both the reference, which is the tanker position, and the dominant disturbance, which is the wind, is well defined using statistical parameters.

The following parameters are used to evaluate the controller performance:

1. **Mean error** is the average error in position.
2. $3\boldsymbol{\sigma}$ is the distance from the mean which contains $99.7\%$ of all measurements. This means that there is only a $0.3\%$ chance that any measurement is outside the $\pm 3\sigma$ bounds.

## 5.3 Straight-and-Level Flight in Light Turbulence

Figures 5.1 to 5.3 show the position of the receptacle relative to the contact and disconnect envelope of the refuelling boom in light turbulence conditions. The lateral and normal controllers perform well in keeping the receptacle within the disconnect envelope, and mostly within the contact envelope as well. It is clear that the axial controller needs improvement in order for the receptacle to stay within the required envelope. If the receptacle leaves the disconnect envelope during AAR the receiver aircraft must immediately brake and move away from the tanker and the refuelling is stopped. This means that the entire connection procedure must be restarted if the more fuel needs to be transferred. The breakaway manoeuvre is not implemented in these simulations.

**Table 5.1** – Statistical parameters: Light turbulence

| | |
|---|---|
| In disconnect env. | 100% |
| In contact env. | 37% |
| $3\sigma_x = 99.7\%$ bound | $\pm 2{,}53\,\mathrm{m}$ |
| $3\sigma_y = 99.7\%$ bound | $\pm 0{,}688\,\mathrm{m}$ |
| $3\sigma_z = 99.7\%$ bound | $\pm 0{,}752\,\mathrm{m}$ |
| Mean error$_x$ | $0{,}0138\,\mathrm{m}$ |
| Mean error$_y$ | $0{,}0131\,\mathrm{m}$ |
| Mean error$_z$ | $-0{,}001\,54\,\mathrm{m}$ |

When inspecting the shape of the disconnect envelope in Figures 5.1 to 5.3, it can be seen that the most restrictive measurement is the boom length. In the contact envelope

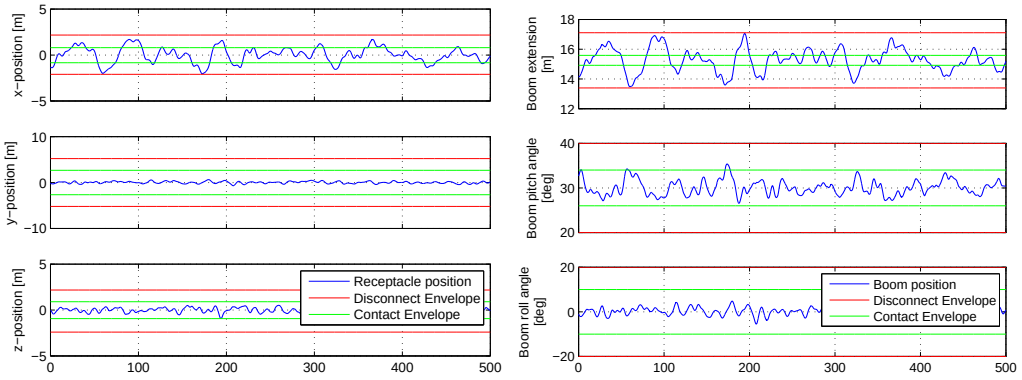


(a) Position errors in XYZ axes. (b) Position errors in boom measurements.

**Figure 5.1** – Straight-and-level flight in light turbulence.

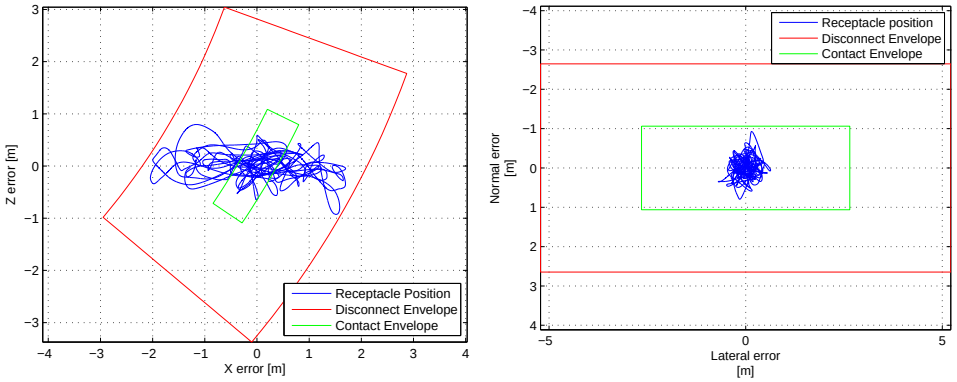


(a) Side view showing axial and normal error. (b) Rear view showing lateral and normal error.

**Figure 5.2** – Straight-and-level flight in light turbulence.

this boom length restriction is even more severe. The pitch angle is less restrictive, and the roll angle has the most leeway.

In the tracking performance of the receiver, the response in the axial direction has the largest error, with a standard deviation of $0{,}843\,\mathrm{m}$ as can be seen in Table 5.1. Unfortunately this has the largest influence in the boom length, which is also the most restrictive specification. Clearly, this is the section of the control which will fail the specifications first as the turbulence increases. It only just stays within the disconnect envelope in light turbulence conditions, and is within the contact envelope only $37\%$ of the time. The normal and lateral control performs much better, with a standard deviation of $0{,}251\,\mathrm{m}$ and $0{,}229\,\mathrm{m}$ respectively.

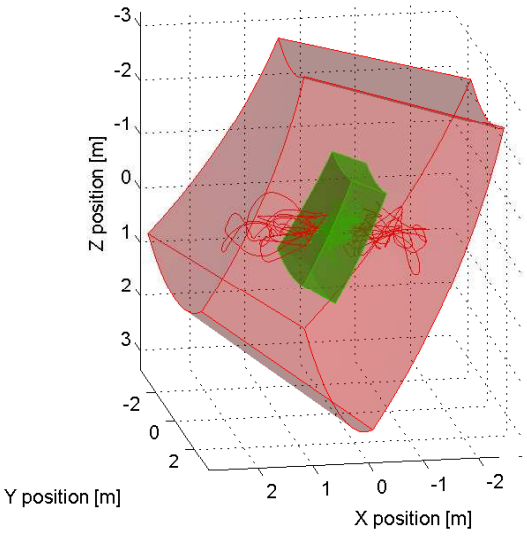


**Figure 5.3** – Straight-and-level flight in light turbulence; 3D movement of the receiver relative to the tanker. The contact envelope is shown in green, and the disconnect envelope in red.

## 5.4 Straight-and-Level Flight in Moderate Turbulence

Figures 5.4 to 5.6 show the tanker tracking performance in moderate turbulence conditions. Here the axial controller is not able to keep the receptacle inside the disconnect envelope. The lateral and normal controllers, however, still succeed in keeping the receptacle within the disconnect envelope in those directions, but not inside the contact envelope.

When the turbulence increases from light to moderate levels, the RMS amplitude of the wind almost doubles. If there is a linear relationship between turbulence intensity and position error, it is expected that the position error will also double. But when

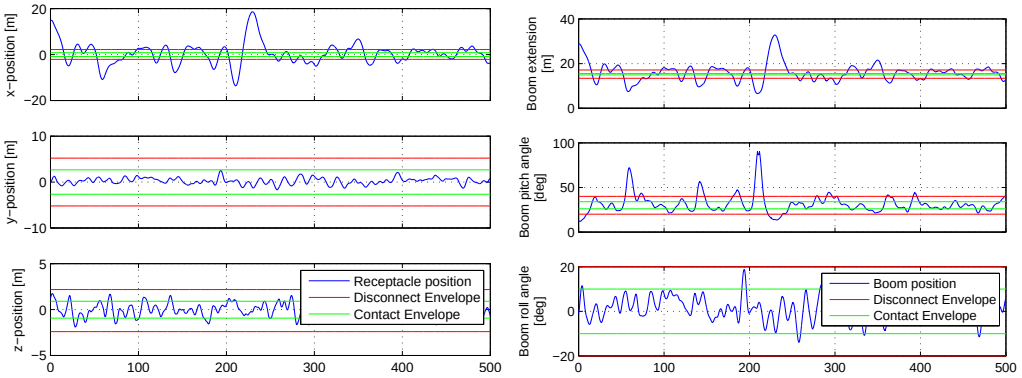


(a) Position errors in XYZ axes.

(b) Position errors in boom measurements.

**Figure 5.4** – Straight-and-level flight in moderate turbulence.

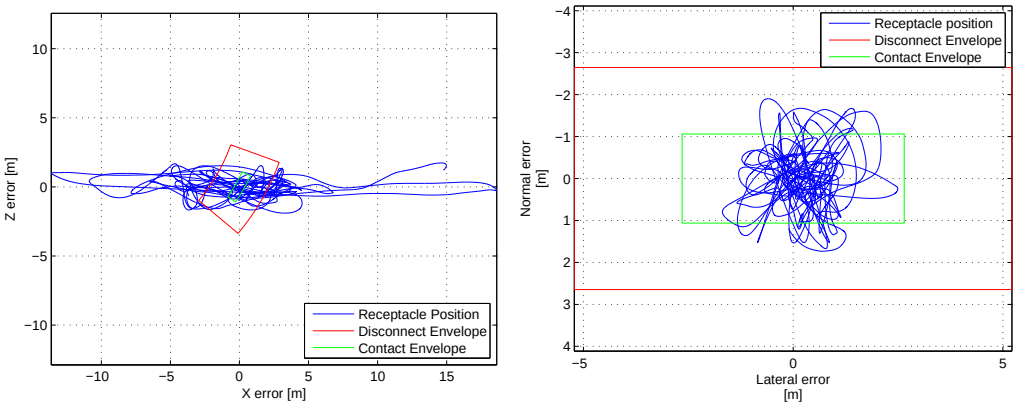


(a) Side view showing axial and normal error. (b) Rear view showing lateral and normal error.

**Figure 5.5** – Straight-and-level flight in moderate turbulence.

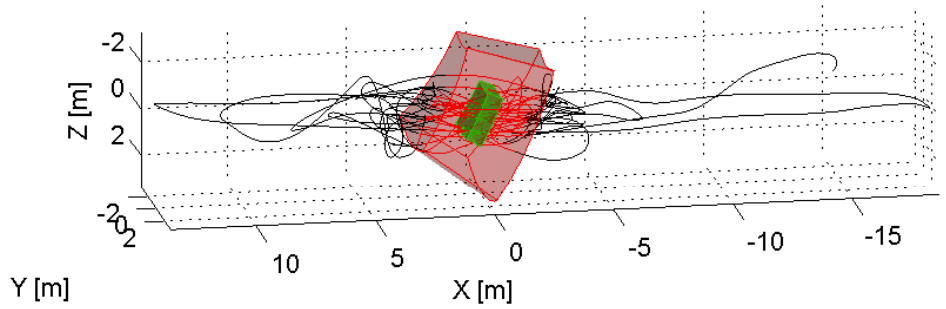


**Figure 5.6** – Straight-and-level flight in moderate turbulence; 3D movement of the receiver relative to the tanker. The contact envelope is shown in green, and the disconnect envelope in red.

comparing Tables 5.1 and 5.2 it is seen that this is not the case: the errors increase with a factor of more than two in the normal and lateral directions and is more than five times larger in the axial direction. This shows that the relation between position error and turbulence is not linear and that the axial dynamics contain the most non-linearities. It is caused in part by the thrust response and by drag.

**Table 5.2** – Statistical parameters: Moderate turbulence

| | |
|---|---|
| In disconnect env. | 39,3% |
| In contact env. | 5,56% |
| $3\sigma_x = 99.7\%$ bound | $\pm 14{,}4\,\mathrm{m}$ |
| $3\sigma_y = 99.7\%$ bound | $\pm 2{,}05\,\mathrm{m}$ |
| $3\sigma_z = 99.7\%$ bound | $\pm 2{,}12\,\mathrm{m}$ |
| Mean error$_x$ | $0{,}454\,\mathrm{m}$ |
| Mean error$_y$ | $0{,}236\,\mathrm{m}$ |
| Mean error$_z$ | $-0{,}000\,906\,\mathrm{m}$ |

## 5.5 Summary

In this chapter the performance of the direct actuator controllers is evaluated in non-linear simulations. In light turbulence the receptacle stays within the disconnect envelope but with a very small margin. In moderate turbulence the control system fails because the axial controller is not able to keep the receptacle within the required envelope. The axial response may be improved by using different control methods. Non-linear control methods may be able to utilise the engines better. Also using other actuators such as the elevator and spoilers along with the engines can give better results. Adjusting the engine controllers to result in a faster engine response will also improve the axial control results that can be achieved. These suggestions are left as future work.

The modelling, design and simulation of the controllers that incorporate the existing manual control laws are considered in the next three chapters. The performance of these controllers will then be compared with the DAC controllers presented in this chapter.

# Chapter 6

# Manual Control Laws Mathematical Model

The fly-by-wire system (FBW) is the electronic interface between the pilot and the aircraft. The control inputs from the pilot are converted by the FBW system into commands for the actuators. The use of FBW enables the design of the airframe to be aerodynamically less stable, because the control system is able to stabilize the airframe without intervention from the pilot.

There are many safety features built into the FBW control system of the A330-300 [20], for example:

1. The maximum deflection angle and slew rate of all actuators are not exceeded.
2. The load factor is limited to a value that can be safely sustained by the airframe.
3. The attitude, altitude and speed is kept within the safe flight envelope of the airframe.
4. The frequencies of the actuator commands are filtered in order to avoid pilot induced oscillation and structural modes of the airframe.

Because the FBW is already carefully designed with these safety features, it is beneficial to design a refuelling controller that works through the FBW system. Such a control system has no direct control over the control surfaces of the aircraft, but only has access to the same inputs as the pilot, such as longitudinal and lateral stick commands, and pedal inputs. The manual control laws (MCL) are the sections of the FBW system which determine how the side-stick and pedal inputs from the pilot control the aircraft.

Since the dynamics of the aircraft are altered by the manual control laws, it is necessary to derive a new dynamic model of the aircraft and MCL combination to use in designing

the refuelling control system. One way to achieve this is to do a low-order system identification of the transfer functions between selected inputs and outputs and then use this simple model as a base for the control design. This is the method used by an intern at Airbus [23]. The purpose of this investigation is to compare different control strategies therefore it was decided not to repeat his work but to rather use another method.

The Simulink model received from Airbus includes the manual control laws. The block diagram was analysed and linearised about the selected trim point in order to get a linear model which is appropriate for using in the control design. The model of the manual control laws is combined with the aircraft model derived in Chapter 3 to build a model of the aircraft with its control laws. This is the plant on which the second set of controllers is based.

## 6.1 Overview

The manual control laws are divided into three controllers (see Figure 6.1):

**DP LAW** uses the ailerons and spoilers of the aircraft to control roll and side-slip.

**DR LAW** works in parallel to DP LAW to control roll and side-slip. This controller only uses the rudder.

**DQ LAW** uses the elevator and horizontal stabilizer to control load factor in the Z-direction.

These controllers need information about the aircraft's dynamic state, for instance velocity and attitude, to operate. Some of these inputs cannot be accurately measured with on-board sensors. It is thus necessary to estimate these inputs using the variables that can be measured.

In the next three sections the state-space equivalents of the manual control laws and estimators of the aircraft are derived.

## 6.2 Normal Control

The overall structure of the Normal Control Laws can be seen in the bottom half of Figure 6.1. The first part of this controller is the longitudinal feed-forward. The normal load factor command $N_{zc}$ is directly proportional to the longitudinal stick position $\lambda_{long}$:

$$\frac{N_{zc}}{\lambda_{long}} = -\frac{1}{16} \tag{6.2.1}$$

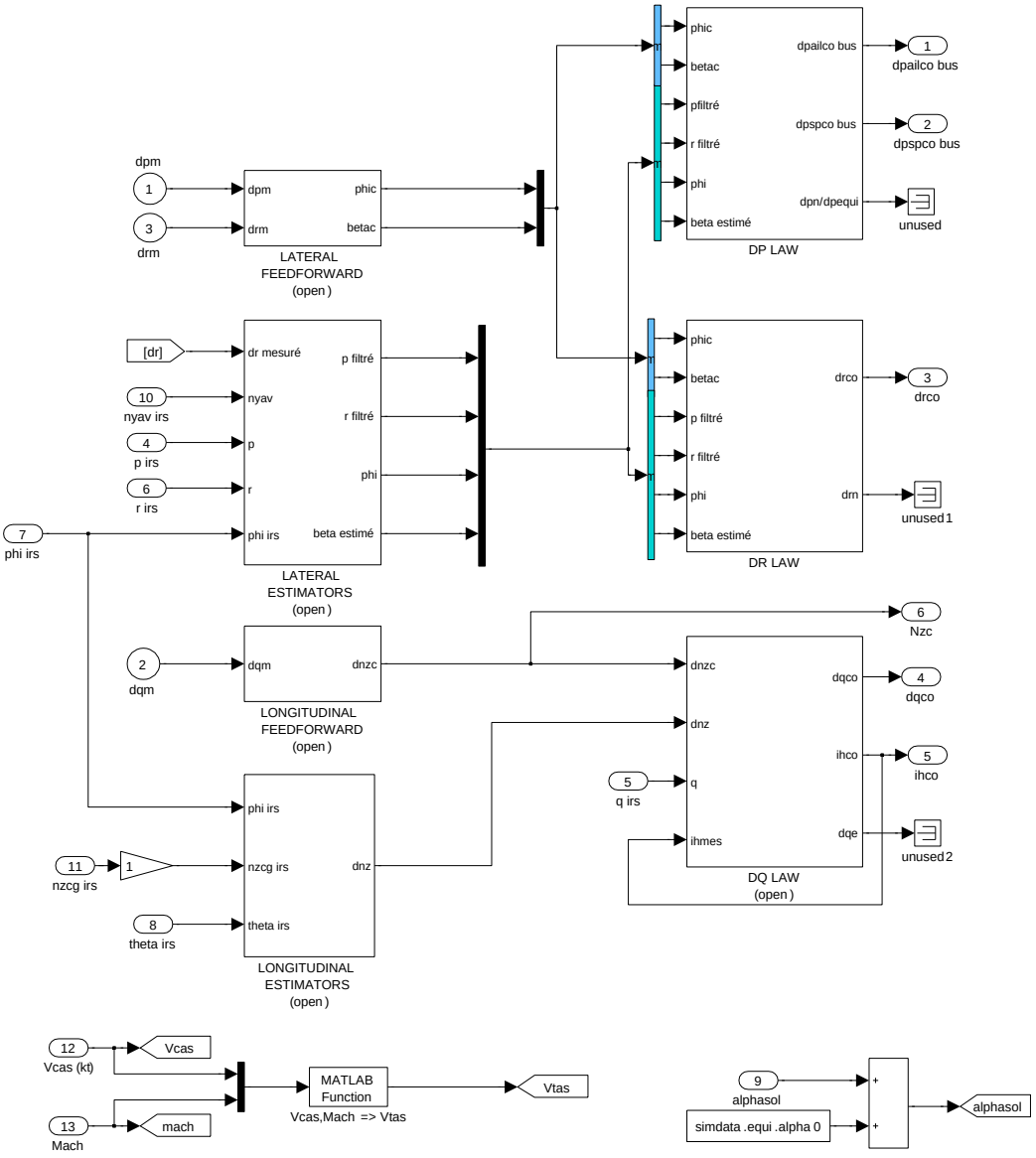


**Figure 6.1** – Block diagram showing the structure of the fly-by-wire model.

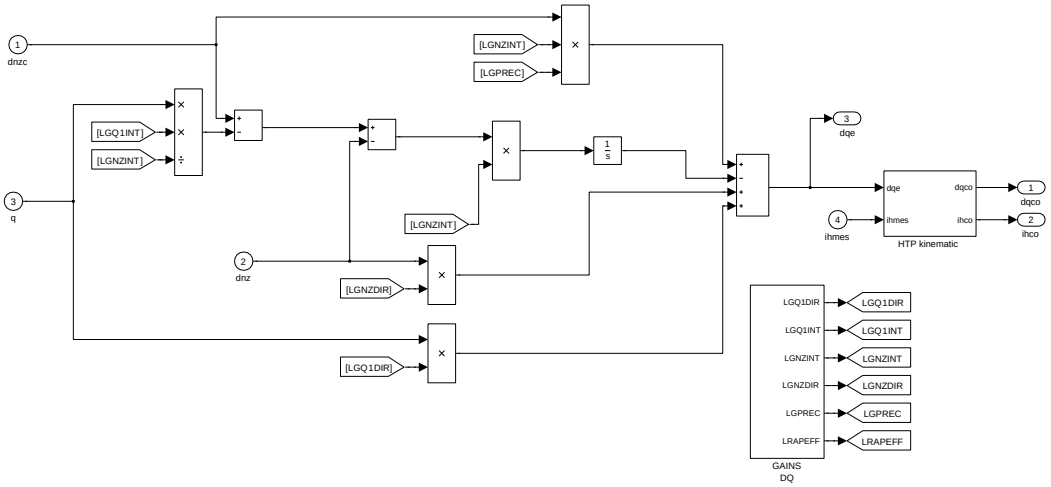


**Figure 6.2** – Block diagram of FBW normal control.

The DQ Law calculates the equivalent elevator command which is needed to follow the normal load factor command. The contents of the DQ LAW block are shown in Figure 6.2, from which the following equations can be derived:

$$\begin{aligned} \dot{x} &= k_{I_{N_z}} N_{zc} - k_{I_{N_z}} N_z - k_{I_q} q \\ \delta_{qe} &= k_{Nzc} N_{zc} + k_{N_z} N_z + k_q q - x \end{aligned} \tag{6.2.2}$$

The equations can be represented in state-space form as:

$$\begin{aligned} \begin{bmatrix} \dot{x} \end{bmatrix} &= \begin{bmatrix} 0 \end{bmatrix} \begin{bmatrix} x \end{bmatrix} + \begin{bmatrix} k_{I_{N_z}} & -k_{I_{N_z}} & -k_{I_q} \end{bmatrix} \begin{bmatrix} N_{zc} \\ N_z \\ q \end{bmatrix} \\ \begin{bmatrix} \delta_{qe} \end{bmatrix} &= \begin{bmatrix} -1 \end{bmatrix} \begin{bmatrix} x \end{bmatrix} + \begin{bmatrix} k_{Nzc} & k_{N_z} & k_q \end{bmatrix} \begin{bmatrix} N_{zc} \\ N_z \\ q \end{bmatrix} \end{aligned} \tag{6.2.3}$$

This equivalent $\delta_{qe}$ deflection is divided between the elevator and the horizontal tail-plane (HTP), shown in Figure 6.3. Only the low frequency commands go to the HTP while the high frequency commands are handled by the elevator. The elevator command is also filtered using a second order Chebychev filter, with coefficients $d_{1,2,3}$, in order to reduce pilot-induced oscillations (PIO). The separation in the command signal is represented by the following equations in the Laplace domain:

$$\frac{\delta_{ih_c}}{\delta_{qe}} = \frac{k_{ih}}{13.3s + 1} \tag{6.2.4}$$

$$\begin{aligned} \frac{\delta_{q_c}}{\delta_{qe}} &= \frac{1}{d_1 s^2 + d_2 s + d_3} - \frac{1}{k_{ih}} \frac{\delta_{ih}}{\delta_{qe}} \\ &= \frac{1}{d_1 s^2 + d_2 s + d_3} - \frac{1}{13.3s + 1} \end{aligned} \tag{6.2.5}$$

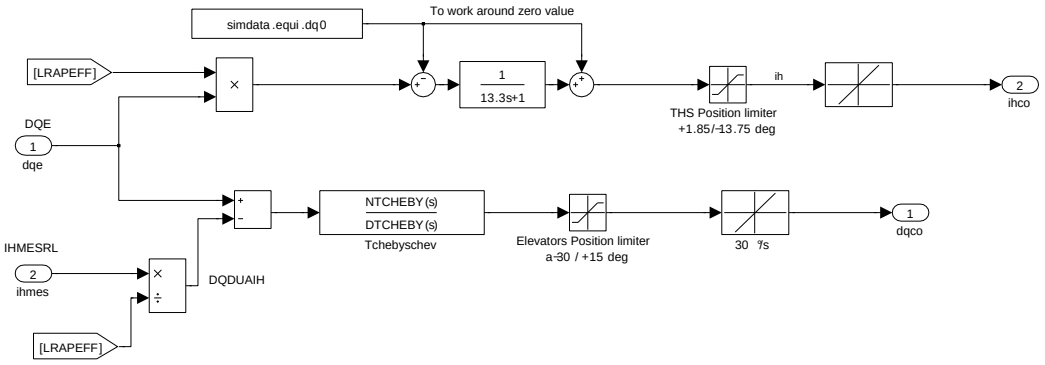


**Figure 6.3** – Block diagram of FBW normal control: elevator and horizontal tailplane kinematics.

The assumption is made that the HTP follows its commanded angle precisely. This is possible because the HTP dynamics, with time constant $\tau = 0{,}1\,\mathrm{s}$, are much faster than its commanded dynamics, with $\tau = 13{,}3\,\mathrm{s}$.

When converted to state-space form, Equations 6.2.4 and 6.2.5 become

$$\begin{aligned}\begin{bmatrix}\dot{x}\end{bmatrix} &= \begin{bmatrix}0 & 1 & 0\\ -\frac{d_3}{d_1} & -\frac{d_2}{d_1} & -\frac{1}{d_1 c_1}\\ 0 & 0 & -\frac{1}{13.3}\end{bmatrix}\begin{bmatrix}x\end{bmatrix} + \begin{bmatrix}0\\ \frac{1}{d_1}\\ \frac{c_1}{13.3}\end{bmatrix}\begin{bmatrix}\delta_{qe}\end{bmatrix}\\ \begin{bmatrix}\delta_{ih_c}\\ \delta_{q_c}\end{bmatrix} &= \begin{bmatrix}0 & 0 & 1\\ 1 & 0 & 0\end{bmatrix}\begin{bmatrix}x\end{bmatrix} + \begin{bmatrix}0\\ 0\end{bmatrix}\begin{bmatrix}\delta_{qe}\end{bmatrix}\end{aligned} \tag{6.2.6}$$

These state-space models are combined using the methods shown in Appendix D.

## 6.3 Lateral Control

The relation between the lateral stick input and the commanded bank angle is shown in Figure 6.4. For smaller bank angles the lateral stick input is interpreted as a roll rate command in such a way that the aircraft holds its bank angle when the stick is released. If the aircraft exceeds the maximum constant bank angle it will return to the maximum constant bank angle as soon as the stick is released. A lookup table is used to accommodate the non-linearities so that the stick input becomes more sensitive the more it deviates from the position zero. If the discontinuities, in this case the dead band and limits, are ignored and the lookup table is approximated by a constant gain, the mathematical relation between lateral stick input $\lambda_{lat}$ and bank angle command $\phi_c$

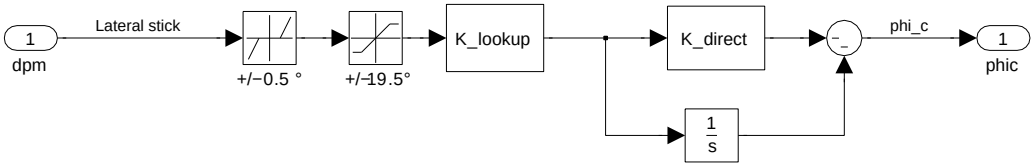


**Figure 6.4** – Block diagram showing the relation between lateral stick input and bank angle command.

is

$$\begin{aligned}\frac{\phi_c}{\lambda_{lat}} &= -K_{lookup}\left(K_{direct}+\frac{1}{s}\right)\\ &= -K_{lookup}\left(\frac{sK_{direct}+1}{s}\right)\end{aligned} \tag{6.3.1}$$

The pilot pedal input is equivalent to the commanded angle of side-slip:

$$\beta_c = \lambda_{pedal} \tag{6.3.2}$$

The DP LAW section of the FBW combines the command and feedback signals into a raw aileron command. This command is then filtered and distributed as command signals to all the individual aileron and spoiler control surfaces. Near the chosen trim point, only the inner set of ailerons is used for roll control. The signal distribution is thus modelled as a constant gain that feeds only to the inner ailerons. This is represented with the following equations:

$$\delta_{p_{raw}} = -K_{p_{\phi c}}\phi_c + K_{p_{\beta c}}\frac{1}{s+1}\beta_c + K_{p_p}p + K_{p_r}r + K_{p_\phi}\phi + K_{p_\beta}\beta \tag{6.3.3}$$

$$\delta_{p_{inner}} = K_{ail}\frac{1}{d_1 s^2 + d_2 s + d_3}\delta_{p_{raw}} \tag{6.3.4}$$

$$\delta_{p_{outer}} = 0 \tag{6.3.5}$$

$$\delta_{spoilers} = 0 \tag{6.3.6}$$

where $d_1$, $d_2$ and $d_3$ are the same Chebychev filter denominator coefficients as in the Normal control section of the FBW.

The side-slip control section of the FBW has a similar structure as the roll control.

$$\begin{aligned}\delta_{r_{raw}} &= -K_{r_{\phi c}}\frac{1}{0.3s+1}\phi_c + K_{r_p}p + K_{r_r}r + K_{r_\phi}\phi + K_{r_\beta}\beta\\ \delta_{r_c} &= K_{rud}\left(\beta_c + K_{comp}\frac{1}{d_1 s^2 + d_2 s + d_3}\delta_{r_{raw}}\right)\end{aligned} \tag{6.3.7}$$

## 6.4 Model Assembly

The different sections of the model are combined with the aircraft model derived in Chapter 3 by applying the methods described in Appendix D in order to get a model of the aircraft with the manual control laws enabled.

The longitudinal and lateral dynamics of the aircraft including the manual control laws can be represented with a 7th order and a 15th order state-space model respectively. The longitudinal model is given by:

$$\begin{aligned} \dot{\boldsymbol{x}} &= \mathbf{A}\boldsymbol{x} + \mathbf{B}\boldsymbol{u} \\ \boldsymbol{y} &= \mathbf{C}\boldsymbol{x} + \mathbf{D}\boldsymbol{u} \end{aligned} \tag{6.4.1}$$

with

$$\mathbf{A} = \begin{bmatrix} 0 & 0 & 0 & 0 & 0 & 0 & 0 \\ -0.0005 & -0.525 & 0.99 & -0.002 & -0.0004 & 0 & 0 \\ 0.0002 & -0.794 & -0.468 & 0 & -0.0208 & 0 & 0 \\ 0 & 0 & 1 & 0 & 0 & 0 & 0 \\ 0 & 0 & 0 & 0 & 0 & 1 & 0 \\ 1.57 & 1600 & 2000 & 0 & -44.8 & -6.9 & -43.5 \\ -0.0335 & -34.1 & -0.681 & 0 & 0.0272 & 0 & 0 \end{bmatrix}$$

$$\mathbf{B} = \begin{bmatrix} 0 \\ 0 \\ 0 \\ 0 \\ 0 \\ 6.61 \\ -0.211 \end{bmatrix}$$

$$\text{with } \boldsymbol{x} = \begin{bmatrix} Mach \\ alpha \\ q \\ theta \\ dqco \\ fbwx2 \\ fbwx4 \end{bmatrix} \qquad \boldsymbol{u} = \begin{bmatrix} dqm \end{bmatrix} \quad \text{and} \quad \boldsymbol{y} = \boldsymbol{x}$$

The lateral model is included in Appendix E.

Figure 6.5 shows the aileron command response due to a lateral stick input. The similarity between the linear and non-linear responses shows that the linear mathematical model is a suitable representation of the non-linear Simulink model. The elevator and rudder linear responses also correspond well with the non-linear response and is shown in Appendix E.

## 6.5 Summary

In this chapter the manual control laws were analysed and a mathematical model was derived. This model was combined with the aircraft model derived in Chapter 3. In

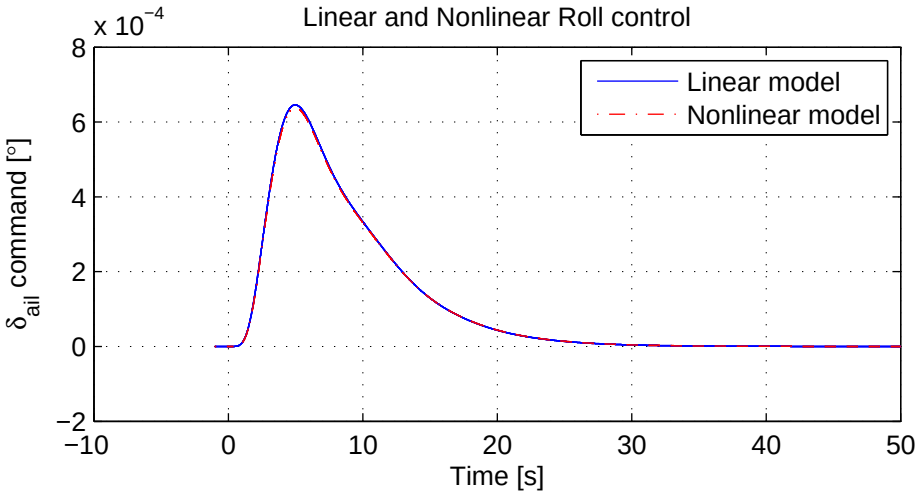


**Figure 6.5** – Comparison of linear and non-linear MCL model roll control aileron command.

the next chapter the design of the set of controllers, also referred to as the side-stick controllers, that makes use of the manual control laws is discussed.

# Chapter 7

# Side-Stick Control Design

The aim of this thesis is to design two sets of controllers that are capable of keeping the receptacle in the correct position for fuel transfer to take place. The first set of control systems commands the actuator deflections directly. The second set of controllers, called the side-stick controllers (SSC), uses the same stick and pedals inputs as are available to the pilot. In this chapter the design of the set of controllers that uses the manual control laws as an inner loop controller is explained. These controllers are based on the mathematical models of the manual control laws developed in Chapter 6 combined with the aircraft model developed in Chapter 3

## 7.1 Controller Design

The second set of controllers uses the model of the aircraft with its manual control laws as foundation for the control design. This model was developed in Chapter 6

The refuelling control is separated into normal, lateral and axial control. This is dictated by the decoupled structure of the manual control laws.

### 7.1.1 Normal Control

For the Normal control, only the longitudinal side-stick input to the MCL is used.

Pole placement with full-state-feedback is used for normal velocity control of the receptacle. The feedback states are:

1. Angle-of-attack perturbation ($\alpha$)
2. Pitch rate perturbation ($q$)
3. Pitch angle perturbation ($\theta$)

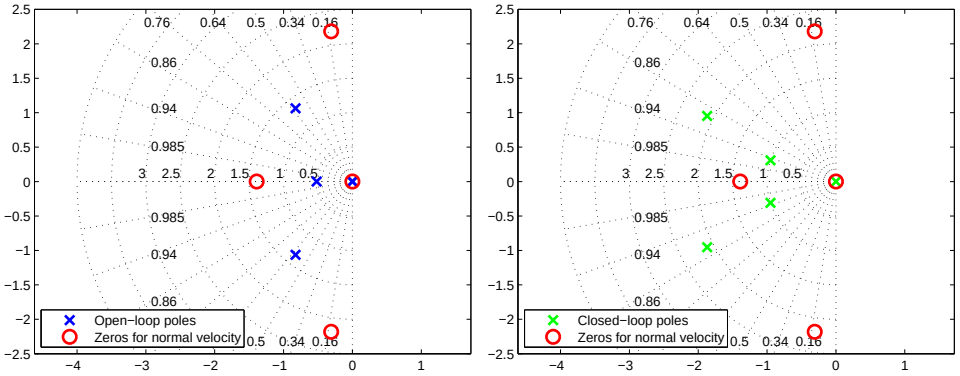


(a) Open-loop poles (b) Closed-loop poles

**Figure 7.1** – Normal control pole placement.

4. Elevator angle ($\delta_{elv}$)
5. Elevator angular rate ($\dot{\delta}_{elv}$)
6. Integral of normal load factor error (as used by the fly-by-wire internally, not measured) ($\int N_{z_{err}}$)

Refer to §6.4 for the state-space model used in the feedback design.

In this simulation the internal fly-by-wire state for the integral of the normal load factor error is not directly accessible. For this reason an approximation of the integral is obtained by duplicating the section of the FBW control system that calculates that integral. This was used instead of a conventional estimator for the following reasons:

- The state estimation part of the greater refuelling project is handled by another student, it is therefore not necessary to develop an estimator for these states if a suitable alternative is available.
- There are negligible uncertainties and non-linearities in that part of the plant.
- Because it is a value that is calculated by an on-board computer, it can be made available for use by all the flight control systems if it is needed.

The open-loop and closed-loop pole and zero positions for normal velocity are shown in Figure 7.1 and Table 7.1. Only the slower dynamics are shown in the figure. The faster poles are not moved, and the slower poles are placed to have sufficient damping, but their bandwidth does not exceed the bandwidth of the complex zero pair that is due to the distance between the aircraft CG and the receptacle. The bandwidth limitation is necessary to avoid adverse movement of the CG while only the receptacle is controlled. See [24] for an analysis of the effect of that pair of zeros on the dynamics of the receiver aircraft.

**Table 7.1** – Pole placement for normal control.

| (a) | | | (b) | | |
|---|---|---|---|---|---|
| Open Loop Poles | | | Closed Loop Poles | | |
| Eigenvalue | $\zeta$ | $\omega_n$ | Eigenvalue | $\zeta$ | $\omega_n$ |
| $0.00193$ | $-1$ | $0.00193$ | $-0.951 \pm 0.309$ | $0.951$ | $1$ |
| $-0.466$ | $1$ | $0.466$ | | | |
| $-0.811 \pm 1.08i$ | $0.599$ | $1.35$ | $-1.87 \pm 0.953$ | $0.891$ | $2.10$ |
| $-2.90 \pm 0.544i$ | $0.470$ | $6.17$ | $-2.90 \pm 0.544i$ | $0.470$ | $6.17$ |

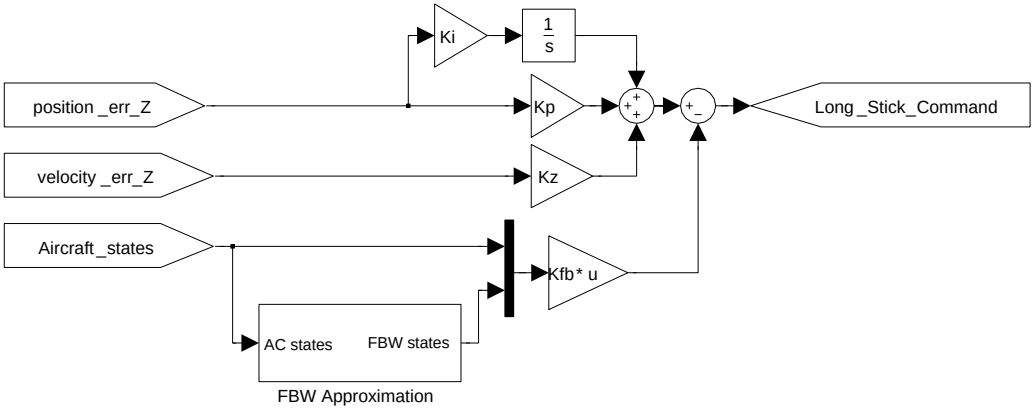


**Figure 7.2** – Structure of the Normal controller.

A position control loop with an integrator is closed around the normal velocity control to complete the normal control architecture. The structure of the completed Normal controller is shown in Figure 7.2.

The response to a $10\,\mathrm{m}$ step in normal position is shown in Figure 7.3. The normal position of the receptacle settles to the commanded position within $10\,\mathrm{s}$. The transient disturbance in the axial position is less than $1{,}3\,\mathrm{m}$, and there is no steady state position error in any direction.

### 7.1.2 Lateral Control

For the Lateral control, the lateral side stick and pedal inputs to the fly-by-wire are used. Pole placement with full-state-feedback is used for lateral velocity control of the receptacle. The feedback states are:

1. Angle of side-slip ($\beta$)
2. Roll rate ($p$)
3. Yaw rate ($r$)

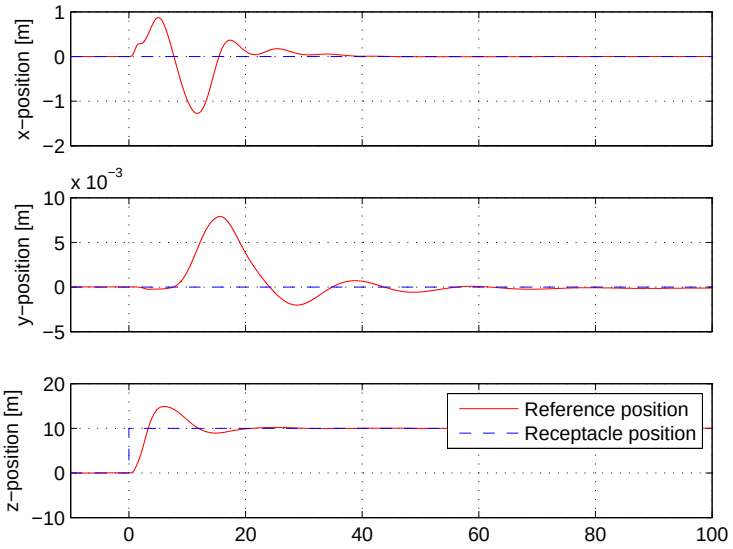


**Figure 7.3** – Response to a Normal position step.

4. Roll angle ($\phi$)
5. Heading angle ($\psi$)
6. Filtered bank angle command
7. Filtered side-slip angle command
8. Filtered roll rate
9. Filtered yaw rate
10. Filtered side-slip angle
11. Integral of lateral stick command

Refer to Chapters 3 and 6 for the state-space models used in the feedback design.

As with the normal control, an approximation for the FBW states is used.

The open-loop and closed-loop pole and zero positions for lateral receptacle velocity are shown in Figure 7.4 and Table 7.2. Only the slower dynamics are shown in the figure. The faster poles are not moved and the slower poles are placed to have increased damping.

A position control loop with an integrator is closed around the lateral velocity control to complete the lateral control architecture. The structure of the controller is shown in Figure 7.5.

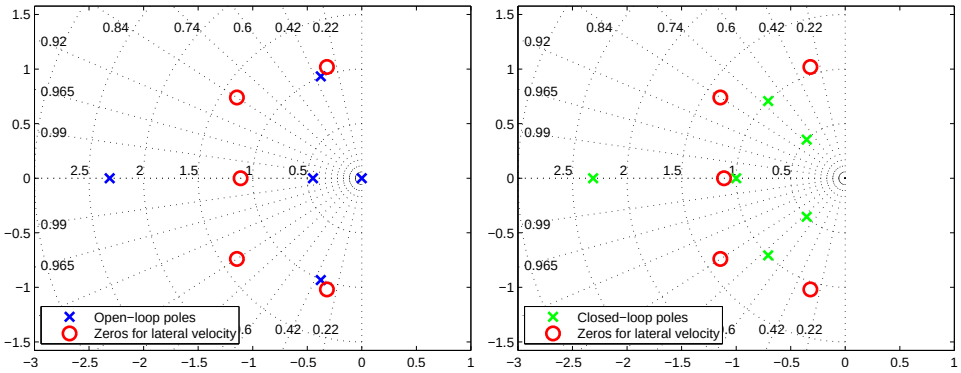


(a) Open-loop poles (b) Closed-loop poles

**Figure 7.4** – Lateral control pole placement.

**Table 7.2** – Pole placement for lateral control.

| (a) | | | (b) | | |
|---|---|---|---|---|---|
| Open Loop Poles | | | Closed Loop Poles | | |
| Eigenvalue | $\zeta$ | $\omega_n$ | Eigenvalue | $\zeta$ | $\omega_n$ |
| $0$ | $1$ | $0$ | $-0.353 \pm 0.354$ | $0.707$ | $0.500$ |
| $0$ | $1$ | $0$ | | | |
| $-0.448$ | $1$ | $0.448$ | $-0.707 \pm 0.707$ | $0.707$ | $1.00$ |
| $-0.376 \pm 0.933i$ | $0.374$ | $1.01$ | $-1.00$ | $1$ | $1.00$ |
| $-2.31$ | $1$ | $2.31$ | $-2.31$ | $1$ | $2.31$ |
| $-3.33$ | $1$ | $3.33$ | $-3.33$ | $1$ | $3.33$ |
| $-2.88 \pm 5.42i$ | $0.469$ | $6.14$ | $-2.88 \pm 5.42i$ | $0.469$ | $6.14$ |
| $-3.18 \pm 5.51i$ | $0.500$ | $6.36$ | $-3.18 \pm 5.51i$ | $0.500$ | $6.36$ |

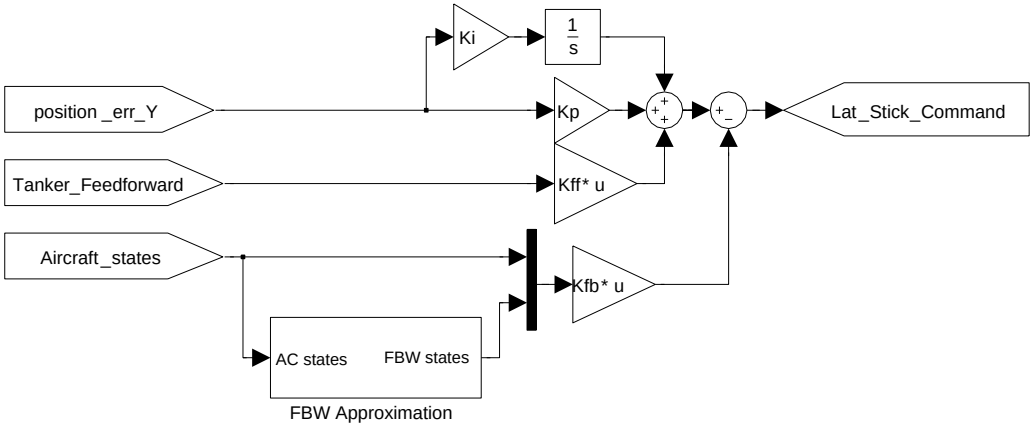


**Figure 7.5** – Structure of the lateral controller.

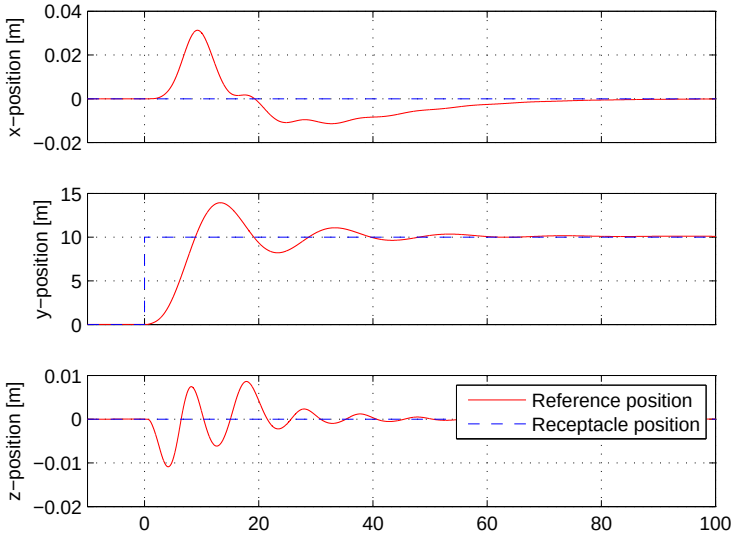


**Figure 7.6** – Response to a lateral step command.

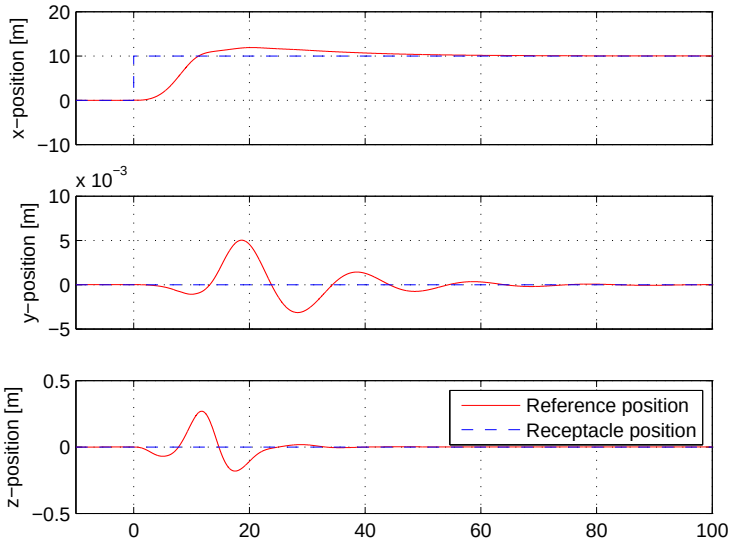


**Figure 7.7** – Response to an axial step command.

### 7.1.3 Axial Control

The axial controller that was designed with the previous set of controllers was duplicated to use with the set of FBW controllers as well as the direct actuator controllers. The response to a 10m step in axial position when used with this set of controllers is shown in Figure 7.7. Refer to §4.3.2 for the design of this controller.

## 7.2 Summary

This chapter explains the structure of the control system which makes use of the pilot inputs. This controller is based on the aircraft model derived in Chapter 3 combined with the FBW model derived in Chapter 6. The response to position step commands are shown and discussed. The performance of these controllers in refuelling conditions are shown in the next chapter.

# Chapter 8

# Side-Stick Control Simulations

The purpose of the controllers that were developed in the previous chapter is to keep the receiver aircraft in the correct position and orientation for fuel transfer to take place. The best way to evaluate the performance of the controllers is to have the controllers perform the task in simulation. The controllers are evaluated using the non-linear Simulink simulation in a calm atmosphere, light turbulence and moderate turbulence.

In the non-linear simulation, the only external disturbance that influences any of the aircraft is the wind. In the absence of wind there is nothing that will make the aircraft deviate from their correct relative position. The step responses in §7.1 already show that the receiver aircraft is able to follow position commands with zero steady-state error in a calm atmosphere. Those results are therefore not repeated in this chapter.

The controllers are tested in light and moderate turbulence. The techniques and parameters that are used to simulate and evaluate the performance of the controllers are the same as was used for the DAC and are discussed in §5.1 and §5.2.

## 8.1 Straight-and-Level Flight in Light Turbulence

The tracking error during refuelling in light turbulence is shown in Figures 8.1 to 8.3.

The control in the normal and lateral directions perform well by keeping the receptacle within the contact envelope for those axes. The axial control performs considerably worse, keeping only within the disconnect envelope. This is because the bandwidth of the engines, which are the only actuators used for axial control, is much slower than the elevator and ailerons, used for normal and lateral control.

In the tracking performance of the receiver, the response in the axial direction has the largest error, with a standard deviation of $0{,}909\,\mathrm{m}$ as can be seen in Table 8.1.

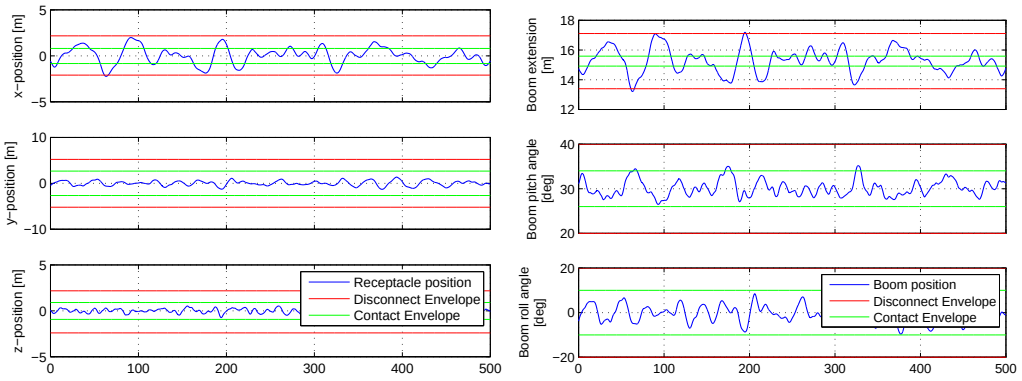


(a) Position errors in XYZ axes. (b) Position errors in boom measurements.

**Figure 8.1** – Straight-and-level flight in light turbulence.

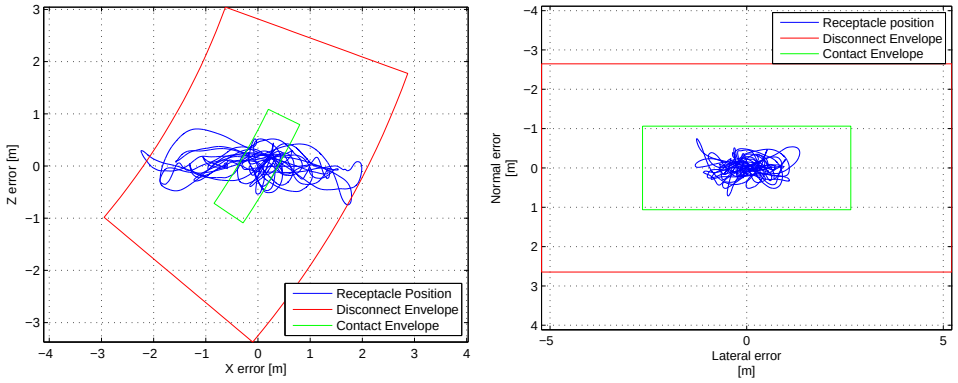


(a) Side view showing axial and normal error. (b) Rear view showing lateral and normal error.

**Figure 8.2** – Straight-and-level flight in light turbulence.

**Table 8.1** – Statistical parameters: Light turbulence.

| | |
|---|---|
| In disconnect env. | 98,7% |
| In contact env. | 37,7% |
| $3\sigma_x = 99.7\%$ bound | $\pm 2{,}73\,\mathrm{m}$ |
| $3\sigma_y = 99.7\%$ bound | $\pm 1{,}6\,\mathrm{m}$ |
| $3\sigma_z = 99.7\%$ bound | $\pm 0{,}702\,\mathrm{m}$ |
| Mean error$_x$ | $0{,}0121\,\mathrm{m}$ |
| Mean error$_y$ | $0{,}007\,59\,\mathrm{m}$ |
| Mean error$_z$ | $-0{,}003\,33\,\mathrm{m}$ |

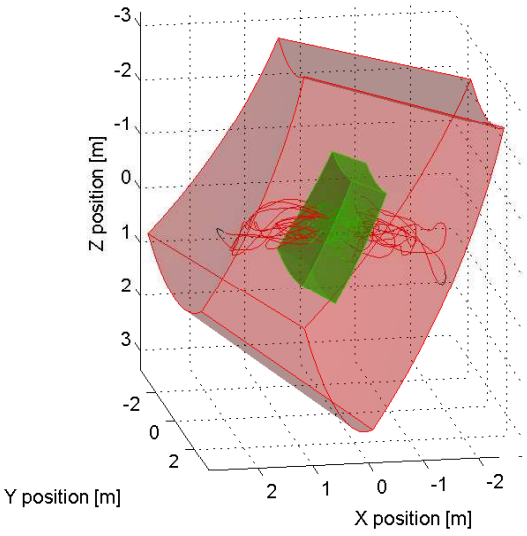


**Figure 8.3** – Straight-and-level flight in light turbulence; 3D movement of the receiver relative to the tanker. The contact envelope is shown in green, and the disconnect envelope in red.

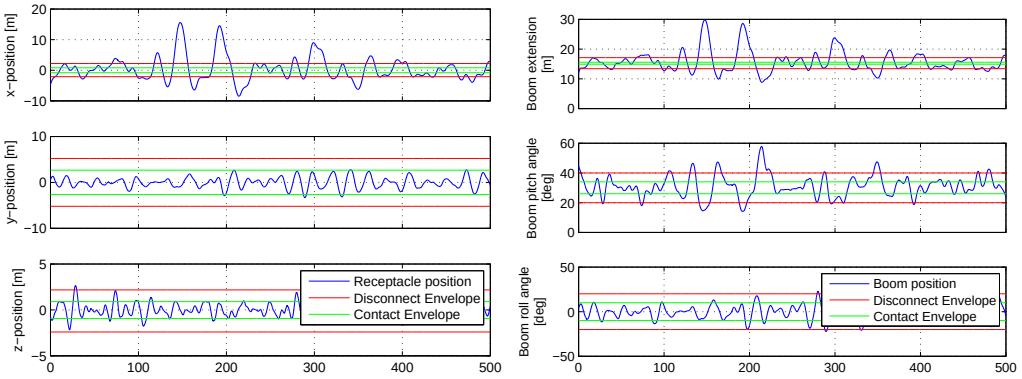


(a) Position errors in XYZ axes.

(b) Position errors in boom measurements.

**Figure 8.4** – Straight-and-level flight in moderate turbulence.

Unfortunately the axial error has the largest influence in the boom length, which is also the most restrictive specification. Clearly, this is the section of the control which will fail the specifications first as the turbulence increases. It only just stays within the disconnect envelope in light turbulence conditions, and is within the contact envelope only $37,7\%$ of the time. The normal and lateral control performs much better, with a standard deviation of $0{,}234\,\mathrm{m}$ and $0{,}535\,\mathrm{m}$ respectively.

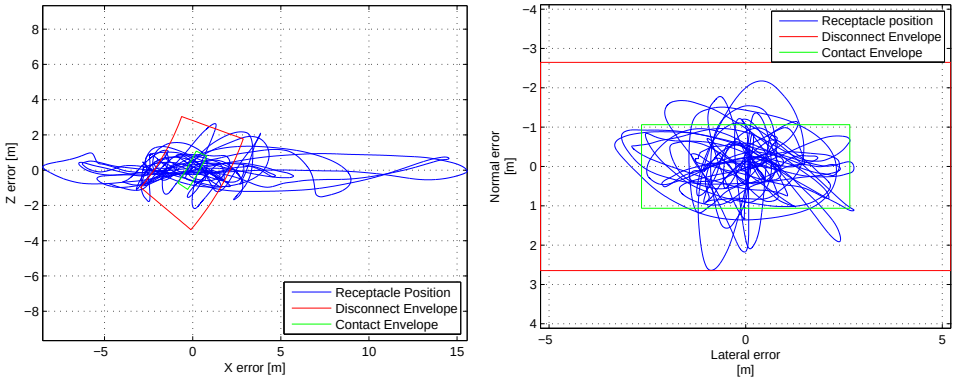


(a) Side view showing axial and normal error. (b) Rear view showing lateral and normal error.

**Figure 8.5** – Straight-and-level flight in moderate turbulence.

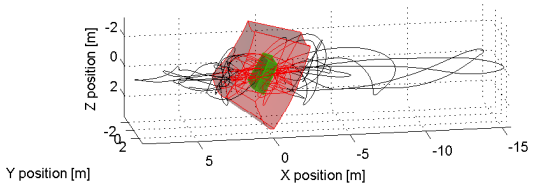


**Figure 8.6** – Straight-and-level flight in moderate turbulence; 3D movement of the receiver relative to the tanker. The contact envelope is shown in green, and the disconnect envelope in red.

**Table 8.2** – Statistical parameters: Moderate turbulence.

| | |
|---|---|
| In disconnect env. | 49,8% |
| In contact env. | 4,9% |
| $3\sigma_x = 99.7\%$ bound | $\pm 12\,\mathrm{m}$ |
| $3\sigma_y = 99.7\%$ bound | $\pm 3{,}58\,\mathrm{m}$ |
| $3\sigma_z = 99.7\%$ bound | $\pm 2{,}21\,\mathrm{m}$ |
| Mean error$_x$ | $0{,}346\,\mathrm{m}$ |
| Mean error$_y$ | $-0{,}0252\,\mathrm{m}$ |
| Mean error$_z$ | $0{,}002\,37\,\mathrm{m}$ |

## 8.2 Straight-and-Level Flight in Moderate Turbulence

Figures 8.4 to 8.6 show the tracking performance in moderate turbulence. Here it is clear that the axial control is not up to the task. Again it is only the axial control that does not perform well: Figure 8.5(b) shows the lateral and normal error of the same simulation and here it can be seen that the receptacle stays well within the disconnect envelope in those directions. The receptacle leaves the disconnect envelope only once in this simulation.

## 8.3 Summary

In this chapter the performance of the side-stick controllers is evaluated in non-linear simulations. The performance is very similar to the performance of the DAC discussed in Chapter 5. In light turbulence the receptacle stays within the disconnect envelope but with a very small margin. In moderate turbulence the control system again fails because the axial controller is not able to keep the receptacle within the required envelope. The performance of the DAC and side-stick controllers are compared in mode detail in the next chapter.

# Chapter 9

# Comparison of Controllers

In this chapter the simulation results for the DAC and side-stick controllers are compared against each other. This is to emphasise the strong and weak points that each controller may have. Each controller was tested in still air, light turbulence and moderate turbulence. In each case, the same tanker data was used in the simulations for both controllers. This simulation procedure was explained in §2.1. Any difference in the position errors is therefore only due to the difference in the control systems, which is suitable for a direct comparison of the two methods.

## 9.1 Straight and Level Flight in Still Air

**Table 9.1** – Calm atmosphere performance measures.

(a) Direct actuator control.

| | |
|---|---|
| In disconnect env. | $100\%$ |
| In contact env. | $100\%$ |
| Mean error$_x$ | $3{,}23 \times 10^{-11}\,\mathrm{m}$ |
| Mean error$_y$ | $0{,}000\,399\,\mathrm{m}$ |
| Mean error$_z$ | $-1{,}19 \times 10^{-12}\,\mathrm{m}$ |

(b) Pilot input control.

| | |
|---|---|
| In disconnect env. | $100\%$ |
| In contact env. | $100\%$ |
| Mean error$_x$ | $-5{,}46 \times 10^{-11}\,\mathrm{m}$ |
| Mean error$_y$ | $4{,}05 \times 10^{-06}\,\mathrm{m}$ |
| Mean error$_z$ | $-6{,}09 \times 10^{-13}\,\mathrm{m}$ |

It was shown in §4.3 and §7.1 that both the direct actuator controller (DAC) and the side-stick controller (SSC) have zero steady-state position error in all three directions. The non-linear simulation results shown in Table 9.1 confirms that the steady state errors are negligible in straight and level flight. The lateral error for the DAC is larger than the other errors because it is the only controller that does not make use of an integrator to eliminate the steady-state error. In spite of this, the error is still only $0{,}4\,\mathrm{mm}$. This is less than 0.01% of the size of the disconnect envelope in that direction.

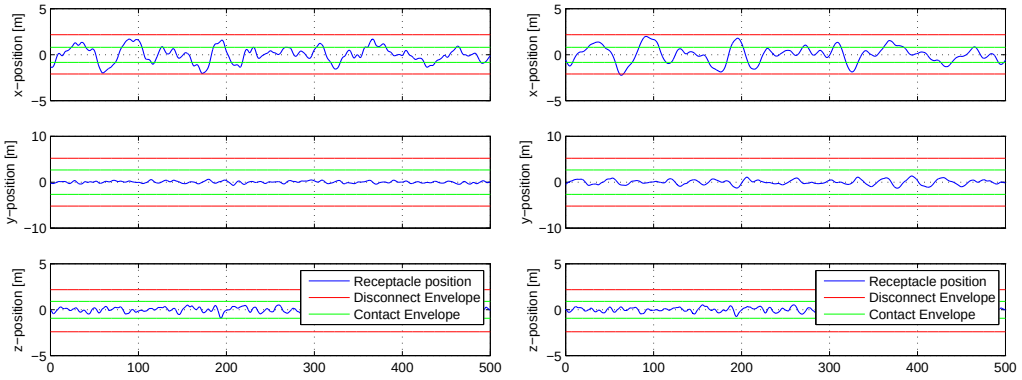


(a) Direct actuator control. (b) Pilot command control.

**Figure 9.1** – Straight-and-level flight in light turbulence: Cartesian position errors.

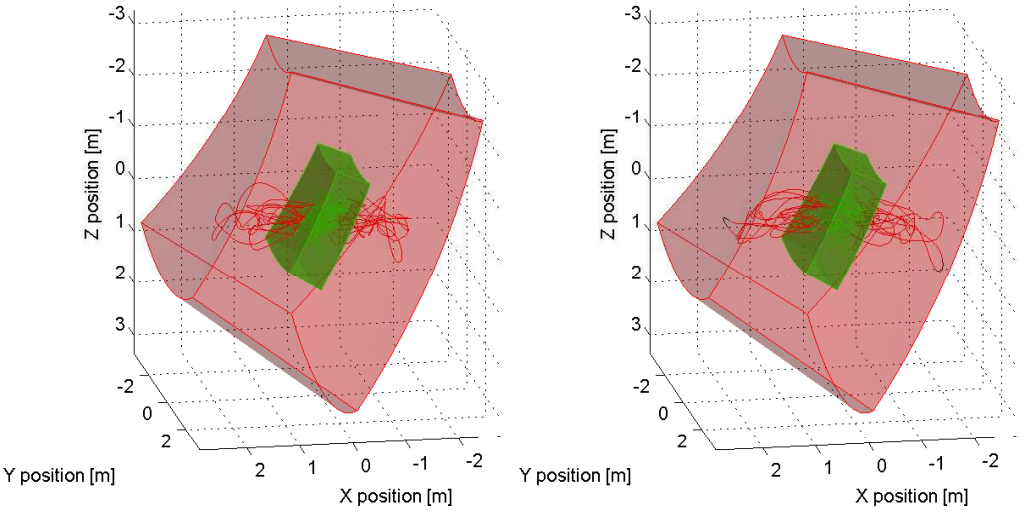


(a) Direct actuator control. (b) Pilot command control.

**Figure 9.2** – Straight-and-level flight in light turbulence: 3D representation of relative position.

## 9.2 Straight and Level Flight in Light Turbulence

Figures 9.1 to 9.4 show the simulation results for refuelling during light turbulence conditions. On the left hand side of each figure is the DAC results while the SSC results are on the right hand side.

Figure 9.1 shows the three Cartesian components of the position error measured in body axes. Because the edges of the contact and disconnect envelopes are defined in terms of boom parameters, the green and red limits are only an approximation of where the envelope limits are in that direction. The two simulations were run with

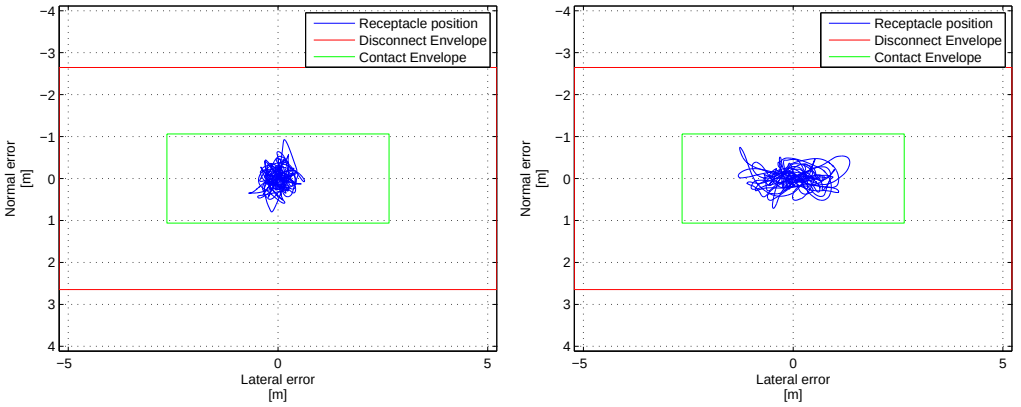


(a) Direct actuator control. (b) Pilot command control.

**Figure 9.3** – Straight-and-level flight in light turbulence: rear view showing lateral and normal errors.

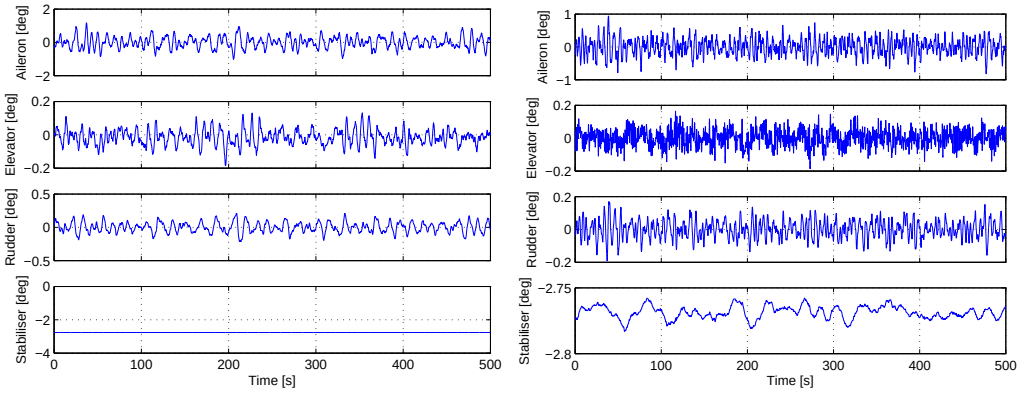


(a) Direct actuator control. (b) Pilot command control.

**Figure 9.4** – Straight-and-level flight in light turbulence: actuator usage.

exactly the same tanker track and turbulence inputs. This is why the general shape of the responses look so similar. This can be seen the clearest in the axial responses which also makes use of the same controller architecture.

### 9.2.1 Axial Control

The actuator deflections of the DAC has a higher bandwidth than SSC. This is because the DAC has a stricter lateral controller than the SSC. In Table 9.2 it is shown that the $3\sigma$ bound for the DAC and SSC for lateral control is $0{,}688\,\mathrm{m}$ and $1{,}6\,\mathrm{m}$ respectively. The DAC error is 57% less than the SSC error. Recall that in Figure 4.11, which is repeated in Figure 9.5, it was shown that position control in the lateral direction causes a disturbance in the axial direction. When Figures 4.11 and 7.6, repeated in Figure 9.5 for convenience, are compared, it can be seen that the lateral controller of the DAC

**Table 9.2** – Light turbulence performance measures.

| (a) Direct actuator control. | | (b) Pilot input control. | |
|---|---|---|---|
| In disconnect env. | 100% | In disconnect env. | 98,7% |
| In contact env. | 37% | In contact env. | 37,7% |
| $3\sigma_x = 99.7\%$ bound | $\pm 2{,}53\,\mathrm{m}$ | $3\sigma_x = 99.7\%$ bound | $\pm 2{,}73\,\mathrm{m}$ |
| $3\sigma_y = 99.7\%$ bound | $\pm 0{,}688\,\mathrm{m}$ | $3\sigma_y = 99.7\%$ bound | $\pm 1{,}6\,\mathrm{m}$ |
| $3\sigma_z = 99.7\%$ bound | $\pm 0{,}752\,\mathrm{m}$ | $3\sigma_z = 99.7\%$ bound | $\pm 0{,}702\,\mathrm{m}$ |
| Mean error$_x$ | $0{,}0138\,\mathrm{m}$ | Mean error$_x$ | $0{,}0121\,\mathrm{m}$ |
| Mean error$_y$ | $0{,}0131\,\mathrm{m}$ | Mean error$_y$ | $0{,}007\,59\,\mathrm{m}$ |
| Mean error$_z$ | $-0{,}001\,54\,\mathrm{m}$ | Mean error$_z$ | $-0{,}003\,33\,\mathrm{m}$ |

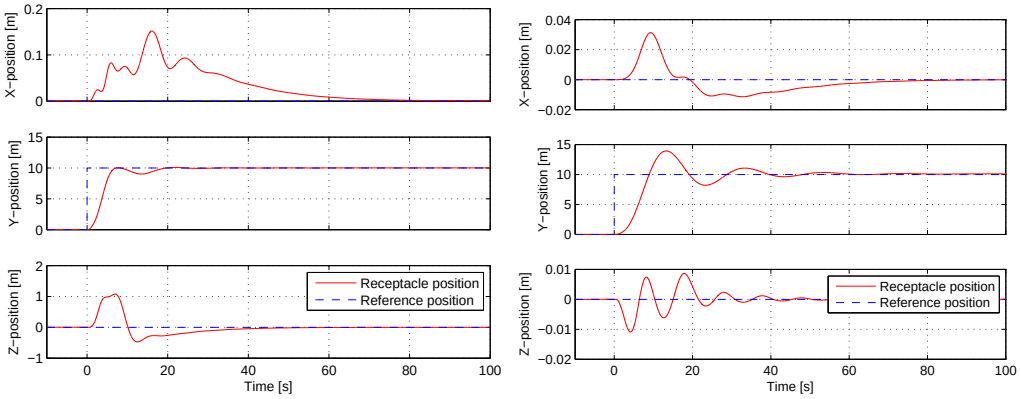


(a) Direct actuator control. (b) Pilot command control.

**Figure 9.5** – Lateral position step response.

causes more disturbance in the axial direction than its counterpart in the SSC. This is why the DAC axial position in Figure 9.1 has an additional higher frequency disturbance when compared with the SSC. Despite this, there is only a 7,9% difference between the $3\sigma$ bounds for the axial directions, showing that the dominant cause of the axial error is still the tanker and receiver aircraft's responses to the turbulence instead of the disturbance caused by the controllers in the other directions.

### 9.2.2 Lateral Control

The DAC lateral error is 57% less than the SSC lateral error. When evaluating this without considering the axial and normal controllers, the DAC is clearly the better performing lateral controller in light turbulence conditions. When evaluating the lateral controllers in context together with the axial and normal controllers, then the smaller errors of the DAC does not necessarily make it more suitable for the refuelling task.

In Figure 9.3 it is visible that both the DAC and SSC lateral controllers are able to keep the receptacle well within the contact envelope in that direction. The lateral position control has an influence on the normal and axial position as seen in Figure 9.5. There

is no advantage to keeping the lateral position to within 20% of the available envelope if that causes enough disturbance in the other directions to cause the receptacle to exit the envelope in those directions. A balance between the controllers is needed.

When the DAC and SSC results in Figure 9.3 are compared visually, it is seen that the position distribution of the SSC resembles the shape of the contact envelope while the position distribution of the DAC does not. This indicates that the SSC has a better balance between the normal and lateral controllers. The advantage of this balance becomes more visible in moderate turbulence and is discussed in §9.3.

### 9.2.3 Normal Control

The normal controllers of the DAC and SSC have a similar performance with $3\sigma$ bounds of $0{,}752\,\mathrm{m}$ and $0{,}702\,\mathrm{m}$ respectively. The most notable difference between them can be seen in Figure 9.4: the DAC does not make use of the HTP. The elevator therefore has to compensate for any steady-state disturbance or change in flight trim position, causing it to have a non-zero mean deflection. With the SSC the low frequency elevator command are handled by the HTP while only the higher frequency control actuations are performed by the elevator. This combination is aerodynamically more efficient than using the elevator alone and may make it easier to adapt the controller to different attitudes and velocities.

### 9.2.4 General Remarks

In both the DAC and SSC the controller that performs the worst is the axial controller. This makes is difficult to compare the two controller sets because their axial position controllers are identical. From Figures 9.2 and 9.3 it can be argued that if the axial controller performance is improved sufficiently, the receptacle can stay within the disconnect envelope and mostly inside the contact envelope during light turbulence, for both control methods.

From Figure 9.4 it can be seen that the aerodynamic actuator deflections are very small compared to their dynamic ranges shown in [20]. This suggests that there is room for substantial improvement in the position control performance.

## 9.3 Straight and Level Flight in Moderate Turbulence

Figures 9.6 to 9.9 show the DAC and SSC simulation results in moderate turbulence levels. From Figure 2.5 it is clear that the amplitude of moderate turbulence is about two times larger than light turbulence. A similar increase in position error can therefore be expected.

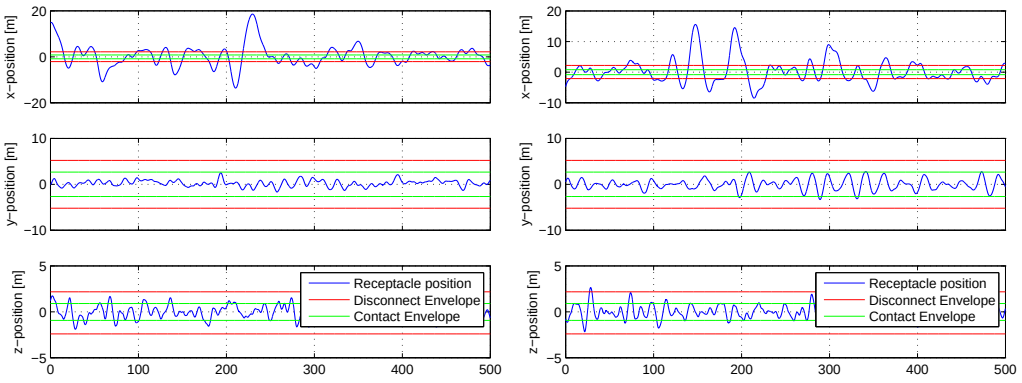


(a) Direct actuator control. (b) Pilot command control.

**Figure 9.6** – Straight-and-level flight in moderate turbulence: Cartesian position errors.

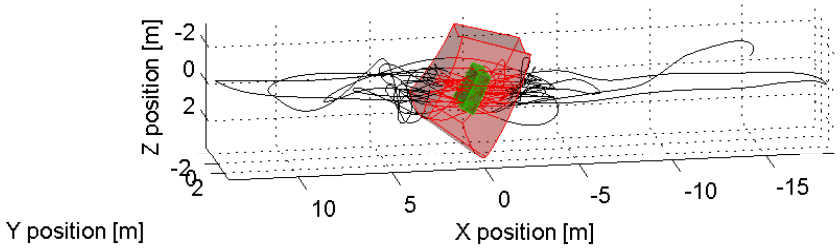


(a) Direct actuator control.

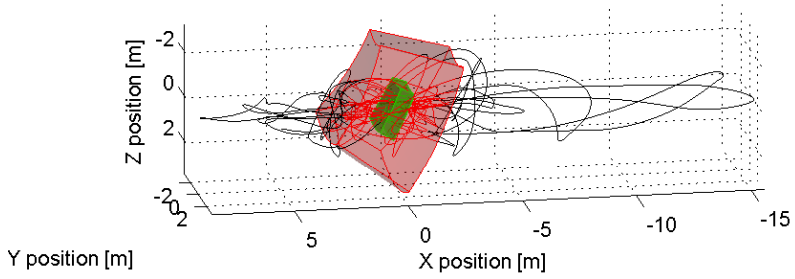


(b) Pilot command control.

**Figure 9.7** – Straight-and-level flight in moderate turbulence: 3D representation of relative position.

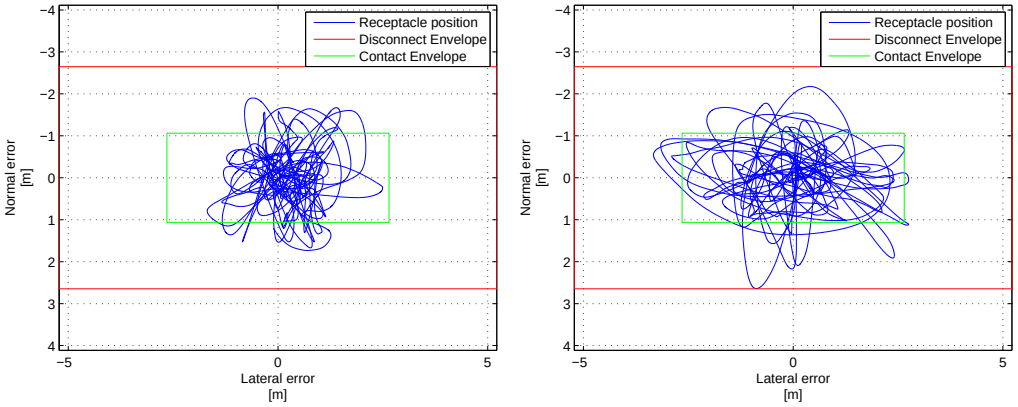


(a) Direct actuator control. (b) Pilot command control.

**Figure 9.8** – Straight-and-level flight in moderate turbulence: rear view showing normal and lateral error.

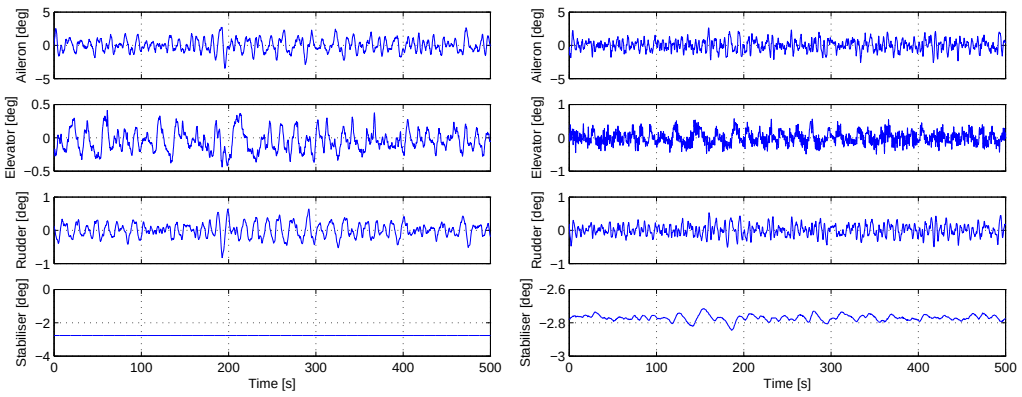


(a) Direct actuator control. (b) Pilot command control.

**Figure 9.9** – Straight-and-level flight in moderate turbulence: actuator usage.

**Table 9.3** – Moderate turbulence performance measures.

(a) Direct actuator control.

| | |
|---|---|
| In disconnect env. | 39,3% |
| In contact env. | 5,56% |
| $3\sigma_x = 99.7\%$ bound | $\pm 14{,}4\,\mathrm{m}$ |
| $3\sigma_y = 99.7\%$ bound | $\pm 2{,}05\,\mathrm{m}$ |
| $3\sigma_z = 99.7\%$ bound | $\pm 2{,}12\,\mathrm{m}$ |
| Mean error$_x$ | $0{,}454\,\mathrm{m}$ |
| Mean error$_y$ | $0{,}236\,\mathrm{m}$ |
| Mean error$_z$ | $-0{,}000\,906\,\mathrm{m}$ |

(b) Pilot input control.

| | |
|---|---|
| In disconnect env. | 49,8% |
| In contact env. | 4,9% |
| $3\sigma_x = 99.7\%$ bound | $\pm 12\,\mathrm{m}$ |
| $3\sigma_y = 99.7\%$ bound | $\pm 3{,}58\,\mathrm{m}$ |
| $3\sigma_z = 99.7\%$ bound | $\pm 2{,}21\,\mathrm{m}$ |
| Mean error$_x$ | $0{,}346\,\mathrm{m}$ |
| Mean error$_y$ | $-0{,}0252\,\mathrm{m}$ |
| Mean error$_z$ | $0{,}002\,37\,\mathrm{m}$ |

In moderate turbulence the axial control fails to keep the receptacle within the disconnect envelope by a large margin. When comparing the plots in Figure 9.7 it is interesting to note that the axial position control of the SSC performs better than the DAC with $3\sigma$ of $12\,\mathrm{m}$ and $14{,}4\,\mathrm{m}$ respectively (see Table 9.3), even though they have identical axial controllers. This shows how the balance between the controllers can affect the overall performance: the axial performance of the SSC is better than the DAC because its controllers, more specifically the lateral control, are more relaxed. Even so the SSC lateral controller is very capable in keeping the receptacle well within the disconnect envelope in that direction, which is what the original design requirements are.

In Figure 9.9 it can be seen that even in moderate turbulence the actuators are not used near their limits by either set of controllers.

## 9.4 Summary

In this chapter the DAC and SSC were evaluated against each other. It was found that the DAC produces smaller errors in the lateral and normal directions, but that the strictness of those controllers cause the axial control to perform worse than in die SSC. This is very pronounced in the moderate turbulence results.

The SSC has a better balance between the aggression of the controllers, allowing the axial control to perform better than in the DAC without causing the receptacle to leave the disconnect envelope in the other directions in moderate turbulence conditions.

In both the DAC and SSC the axial controller is unable to keep the receptacle within the disconnect envelope in moderate turbulence, and only marginally within the disconnect envelope in light turbulence. Both the controllers will be able to keep the receptacle within the disconnect envelope during light turbulence if a better performing axial controller is used.

# Chapter 10

# Conclusions and Recommendations

## 10.1 Summary of Work

In this project several sets of controllers were developed to control the position of the receiver aircraft during air-to-air refuelling. They were all designed to work near one trim condition which is near the centre of the required flight envelope for refuelling.

The first set of controllers, the DAC, use the aerodynamic actuators directly. The first iteration of the DAC controls the CG position of the receiver relative to the tanker boom mid position. This often resulted in steady state errors in the receptacle position due to an orientation that was different than the orientation for which the controller was developed. This was improved by measuring the position error between the boom mid position and the receptacle position and then commanding a change in CG position that will rectify that receptacle error. Due to the large distance between the CG and receptacle, the dynamics of the receptacle differs from the CG dynamics. Therefore the controller that controls the receptacle using the CG dynamics is at a disadvantage. This controller was therefore redesigned using a model of the receptacle dynamics instead of the CG dynamics.

All the controllers mentioned above were MIMO pole placement controllers that used the first order engine model. When the non-linear engine model was tested with these controllers, they were unable to ensure a stable response. The longitudinal MIMO controller of the DAC was therefore split into a SISO normal controller and a SISO axial controller which works with the non-linear engine model. This set of controllers was able to keep the receptacle within the disconnect envelope during light turbulence. In moderate turbulence the axial controller was unable to reliably keep the receptacle within the disconnect envelope, while the lateral and normal controllers still succeeded in keeping the receptacle within the disconnect envelope.

The second set of controllers, the SCC, uses the side stick and pedal inputs to control

the receptacle position of the receiver aircraft. The manual control laws of the aircraft acts as an inner loop controller. The controller was separated into normal, lateral and axial controllers. Both the normal and lateral controllers were designed using pole placement. The axial controller for the SCC was the same controller as was designed for the DAC, because the manual control laws do not influence the engine thrust.

Both these controllers were tested in simulations of different refuelling scenarios. Refuelling was simulated in still air, light turbulence and moderate turbulence. Initial tests were also performed for refuelling in a constant banked turn, but the results are not in a form that is suitable for inclusion in this document. It can be provided by the author on request.

## 10.2 Conclusions

The performance of the controllers are very similar in the normal and lateral directions. Both controllers are able to keep the receptacle within the contact envelope during light turbulence, and within the disconnect envelope during moderate turbulence. The lateral position control performance of the DAC is slightly better than the SSC, but the SSC still keeps the receptacle within the required envelope. This investigation succeeds in showing that both control strategies are equally suitable for the normal and lateral control at the chosen trim condition. It is however not known how valid this conclusion is at other flight conditions. Further investigation will be very useful.

Using only the engine thrust to perform the axial control is not sufficient. Therefore before automated refuelling can be performed, a different type of axial control must be developed. Examples of different axial controllers and other suggestions are given in the next section.

## 10.3 Recommendations for Future Work

There is very little difference between the performances of the two control strategies for the trim point used in this thesis. It is therefore recommended to use the pilot inputs to perform the task, because the safety features of the FBW system are not bypassed. It is however not known whether this holds true for the entire flight envelope, therefore further investigation is needed to determine the effects of different trim points.

The axial position control which is developed in §4.3.2 is only just able to perform the refuelling task in light turbulence and fails to meet the position requirements in moderate turbulence. Using only the thrust to control axial position is therefore not sufficient. Several improvements to the axial control can be suggested:

1. The normal and lateral controllers can be made less aggressive in order to decrease their effect on the axial position. Doing this may increase the margin by which the receptacle stays within position in light turbulence, but will not improve the axial positions control enough to stay within the disconnect envelope in moderate turbulence.

2. The normal and axial controllers can be combined in to a single longitudinal controller. This enables drag as well as thrust to be used for axial control. Drag is changed by changing the angle-of-attack of the aircraft.

3. Additional actuators such as the spoilers can be used. Spoilers increase the drag and decrease the lift of the aircraft by changing the aerodynamic shape of the wing.

The usage of the ailerons can perhaps be adopted so that the left and right ailerons can be actuated in the same direction as well as in opposite directions in the same way as flaperons. This will increase the number of actuators available for longitudinal control, resulting in greater flexibility of the controller. The ailerons are already used in this way during landing when the flaps are extended. It is included as an interesting concept for refuelling control.

The two sets of controllers that are described in this thesis use only a fraction of the actuator deflections that are possible for the aerodynamic control surfaces. Controller designs that use more actuation power will be able to get better results in the normal and lateral directions.

The wake of the tanker and the bow wave of the receiver each has an influence on the other aircraft. Including information of these effects will improve the reliability of the results because the simulation then represent the reality more closely.

# Appendix A

# Linear Model Responses

## A.1 Decoupled Model for Straight-and-Level Flight

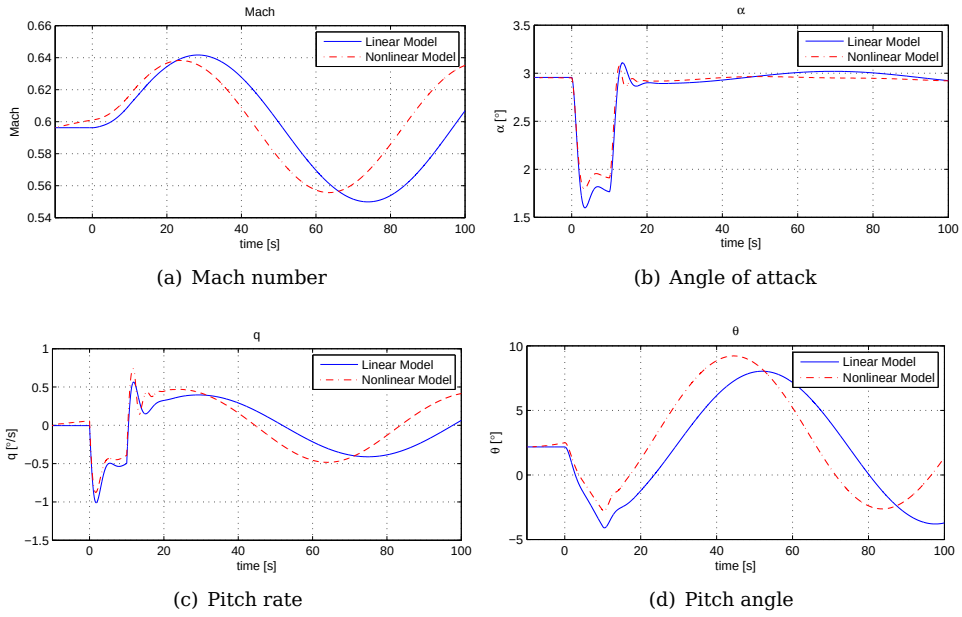


(a) Mach number (b) Angle of attack

(c) Pitch rate (d) Pitch angle

**Figure A.1** – Decoupled linear versus non-linear response due to an elevator input.

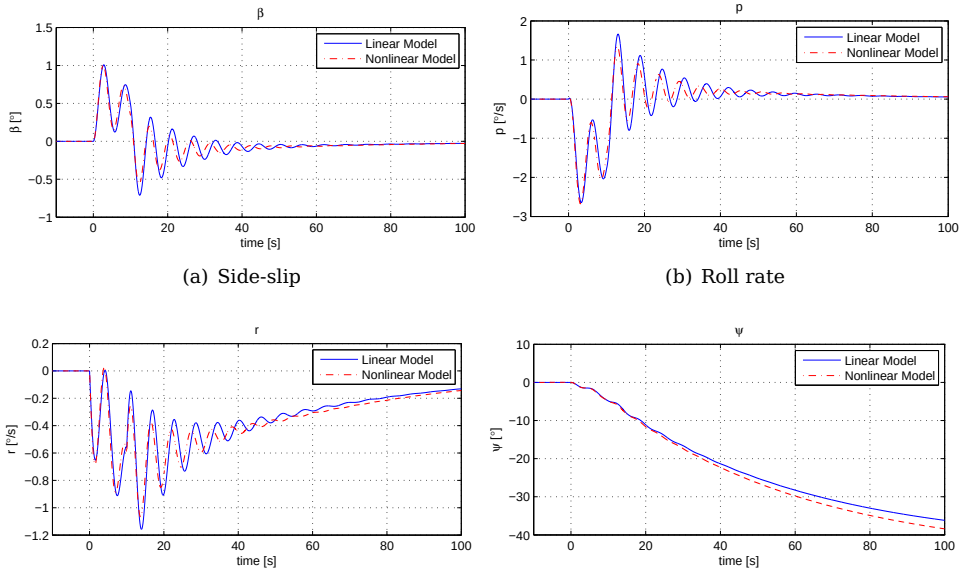


(a) Side-slip (b) Roll rate

(c) Yaw rate (d) Yaw angle

**Figure A.2** – Decoupled linear versus non-linear response due to a rudder input.

## A.2 Coupled Model for a Constant Banked Turn

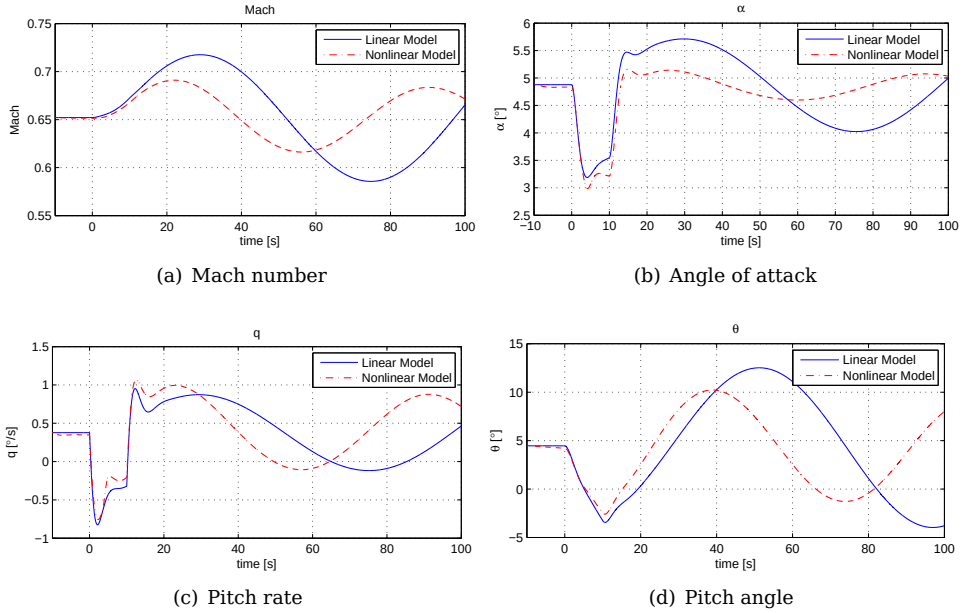


(a) Mach number

(b) Angle of attack

(c) Pitch rate

(d) Pitch angle

**Figure A.3** – Linear versus non-linear response due to an elevator input during a constant banked turn.

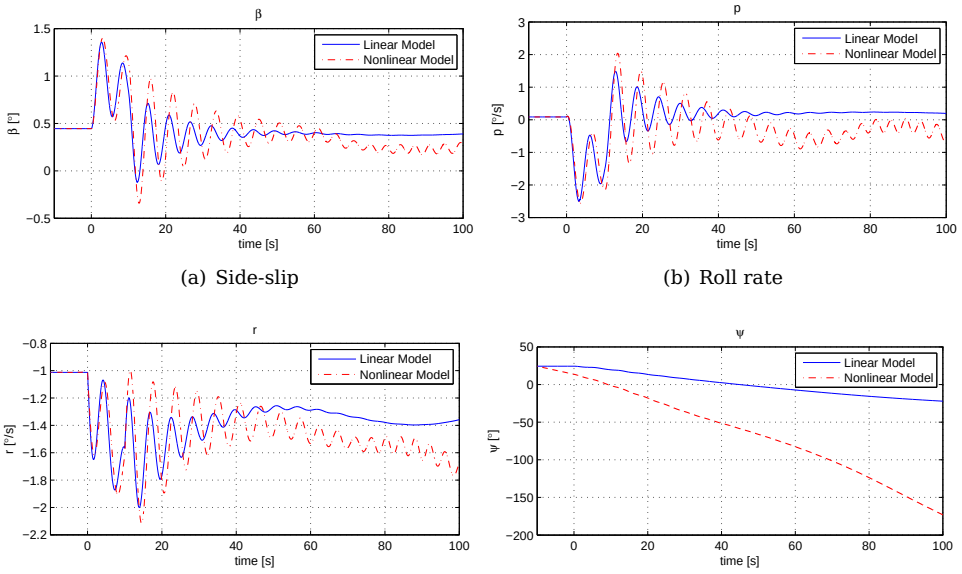


(a) Side-slip (b) Roll rate

(c) Yaw rate (d) Yaw angle

**Figure A.4** – Linear versus non-linear response due to a rudder input during a constant banked turn.

# Appendix B

# Non-linear Engine Model

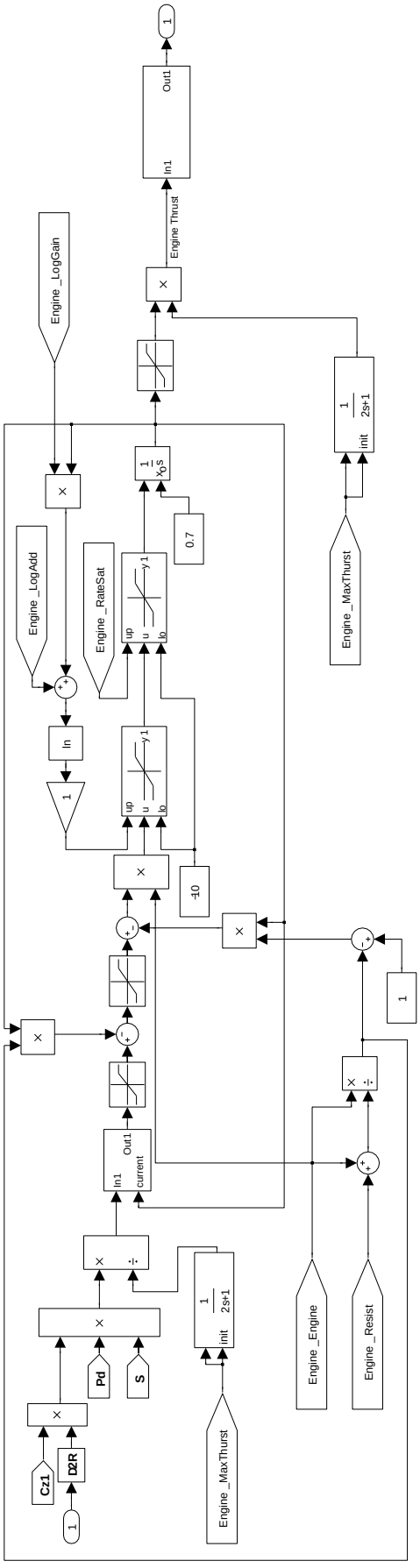


**Figure B.1** – Block diagram of the non-linear engine model developed by [4].

# Appendix C

# CG Control Simulation Results

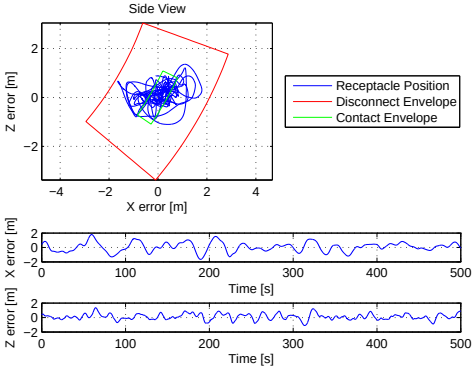


**Figure C.1** – CG Control non-linear longitudinal response in light turbulence

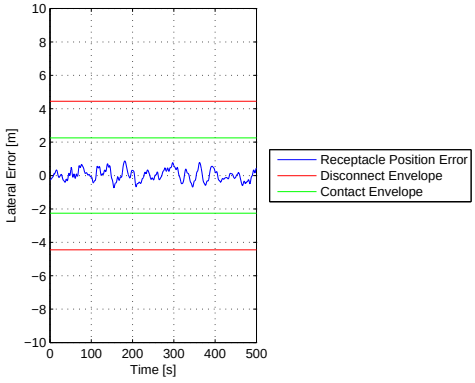


**Figure C.2** – CG Control non-linear lateral response in light turbulence

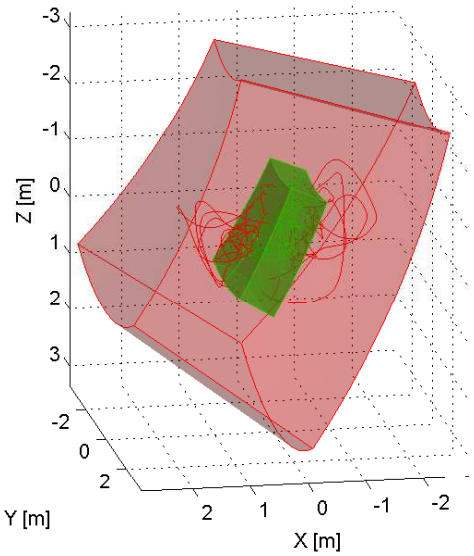


**Figure C.3** – CG Control non-linear response in light turbulence

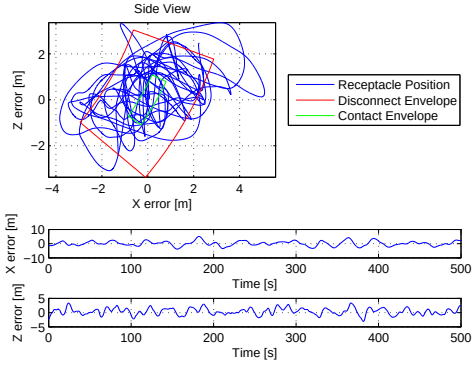


**Figure C.4** – CG Control non-linear longitudinal response in medium turbulence

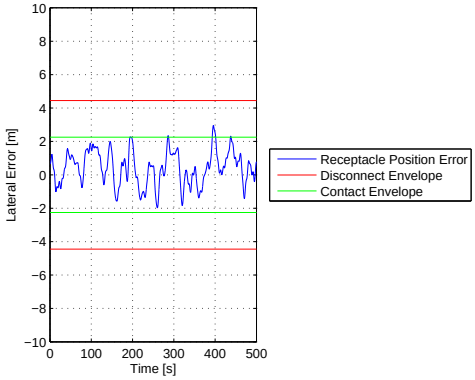


**Figure C.5** – CG Control non-linear lateral response in medium turbulence

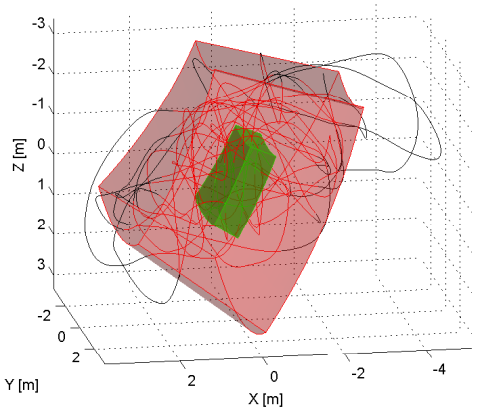


**Figure C.6** – CG Control non-linear response in medium turbulence

# Appendix D

# State-Space Model Manipulations

## D.1 Combination

The combining of two models can be represented by Figure D.1. By carefully choosing the signal sets $u_1$, $u_2$, $y_1$, $y_2$ and $w$, this diagram can represent series connection ($u_2 = y_1 = []$) or parallel connection ($w = []$), or any combination of the two, as long as no feedback is performed. Feedback is considered separately in §D.2. The input signals which form part of $u_1$ and $u_2$ do not need to be unique.

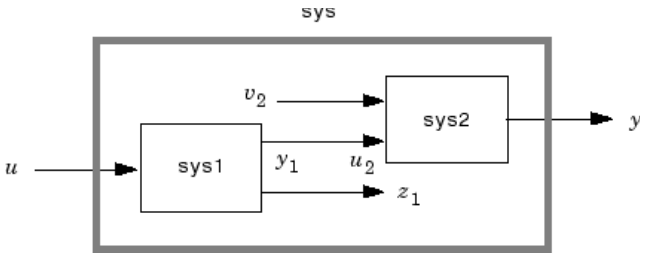


(a)

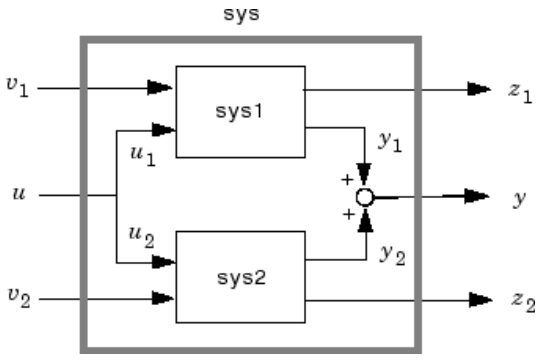


(b)

**Figure D.1** – General representation of the combination of two models without feedback.

The first system is represented in state-space form by the matrices $[\mathbf{A}, \mathbf{B}, \mathbf{C}, \mathbf{D}]$ and the state vector $\boldsymbol{x}_1$, and the second system by $[\mathbf{K}, \mathbf{L}, \mathbf{M}, \mathbf{N}]$ and $\boldsymbol{x}_2$.

$$\begin{aligned} \dot{\boldsymbol{x}}_1 &= \mathbf{A}\boldsymbol{x}_1 + \mathbf{B}\boldsymbol{u}_1 \\ \begin{bmatrix} \boldsymbol{y}_1 \\ \boldsymbol{w} \end{bmatrix} &= \mathbf{C}\boldsymbol{x}_1 + \mathbf{D}\boldsymbol{u}_1 \end{aligned} \tag{D.1.1}$$

Split the matrices $\mathbf{C}$ and $\mathbf{D}$ so that

$$\boldsymbol{y}_1 = \mathbf{C}_1\boldsymbol{x}_1 + \mathbf{D}_1\boldsymbol{u}_1 \text{ and} \tag{D.1.2}$$

$$\boldsymbol{w} = \mathbf{C}_2\boldsymbol{x}_1 + \mathbf{D}_2\boldsymbol{u}_1 \tag{D.1.3}$$

Do the same with the second system.

$$\begin{aligned} \dot{\boldsymbol{x}}_2 &= \mathbf{K}\boldsymbol{x}_2 + \mathbf{L}\begin{bmatrix} \boldsymbol{w} \\ \boldsymbol{u}_2 \end{bmatrix} \\ &= \mathbf{K}\boldsymbol{x}_2 + \mathbf{L}_1\boldsymbol{w} + \mathbf{l}_2\boldsymbol{u}_2 \end{aligned} \tag{D.1.4}$$

$$\begin{aligned} \boldsymbol{y}_2 &= \mathbf{M}\boldsymbol{x}_2 + \mathbf{N}\begin{bmatrix} \boldsymbol{w} \\ \boldsymbol{u}_2 \end{bmatrix} \\ &= \mathbf{M}\boldsymbol{x}_2 + \mathbf{N}_1\boldsymbol{w} + \mathbf{n}_2\boldsymbol{u}_2 \end{aligned} \tag{D.1.5}$$

Combine Equations D.1.2 to D.1.5 to form a system with input vector $[\boldsymbol{u}_1; \boldsymbol{u}_2]$, state vector $[\boldsymbol{x}_1; \boldsymbol{x}_2]$ and output vector $[\boldsymbol{y}_1; \boldsymbol{y}_2]$.

$$\begin{bmatrix} \dot{\boldsymbol{x}}_1 \\ \dot{\boldsymbol{x}}_2 \end{bmatrix} = \begin{bmatrix} \mathbf{A} & \mathbf{0} \\ \mathbf{0} & \mathbf{K} \end{bmatrix}\begin{bmatrix} \boldsymbol{x}_1 \\ \boldsymbol{x}_2 \end{bmatrix} + \begin{bmatrix} \mathbf{B} & \mathbf{0} \\ \mathbf{0} & \mathbf{L}_2 \end{bmatrix}\begin{bmatrix} \boldsymbol{u}_1 \\ \boldsymbol{u}_2 \end{bmatrix} + \begin{bmatrix} \mathbf{0} \\ \mathbf{L}_1 \end{bmatrix}\boldsymbol{w} \tag{D.1.6}$$

$$\begin{bmatrix} \boldsymbol{y}_1 \\ \boldsymbol{y}_2 \end{bmatrix} = \begin{bmatrix} \mathbf{C}_1 & \mathbf{0} \\ \mathbf{0} & \mathbf{M} \end{bmatrix}\begin{bmatrix} \boldsymbol{x}_1 \\ \boldsymbol{x}_2 \end{bmatrix} + \begin{bmatrix} \mathbf{D}_1 & \mathbf{0} \\ \mathbf{0} & \mathbf{N}_2 \end{bmatrix}\begin{bmatrix} \boldsymbol{u}_1 \\ \boldsymbol{u}_2 \end{bmatrix} + \begin{bmatrix} \mathbf{0} \\ \mathbf{N}_1 \end{bmatrix}\boldsymbol{w} \tag{D.1.7}$$

Remove the linked input/output $\boldsymbol{w}$ to get the final combined model by substituting with Equation D.1.3:

$$\begin{bmatrix} \dot{\boldsymbol{x}}_1 \\ \dot{\boldsymbol{x}}_2 \end{bmatrix} = \begin{bmatrix} \mathbf{A} & \mathbf{0} \\ \mathbf{L}_1\mathbf{C}_2 & \mathbf{K} \end{bmatrix}\begin{bmatrix} \boldsymbol{x}_1 \\ \boldsymbol{x}_2 \end{bmatrix} + \begin{bmatrix} \mathbf{B} & \mathbf{0} \\ \mathbf{L}_1\mathbf{D}_2 & \mathbf{L}_2 \end{bmatrix}\begin{bmatrix} \boldsymbol{u}_1 \\ \boldsymbol{u}_2 \end{bmatrix} \tag{D.1.8}$$

$$\begin{bmatrix} \boldsymbol{y}_1 \\ \boldsymbol{y}_2 \end{bmatrix} = \begin{bmatrix} \mathbf{C}_1 & \mathbf{0} \\ \mathbf{N}_1\mathbf{C}_2 & \mathbf{M} \end{bmatrix}\begin{bmatrix} \boldsymbol{x}_1 \\ \boldsymbol{x}_2 \end{bmatrix} + \begin{bmatrix} \mathbf{D}_1 & \mathbf{0} \\ \mathbf{N}_1\mathbf{D}_2 & \mathbf{N}_2 \end{bmatrix}\begin{bmatrix} \boldsymbol{u}_1 \\ \boldsymbol{u}_2 \end{bmatrix} \tag{D.1.9}$$

## D.2 Feedback

A general representation of feedback is shown in Figure D.2. The input and output matrices corresponding to $\boldsymbol{u}_2$ and $\boldsymbol{y}_2$ are calculated so that the correct signals are fed back, and that the correct type of feedback, e.g. positive or negative feedback, is accomplished.

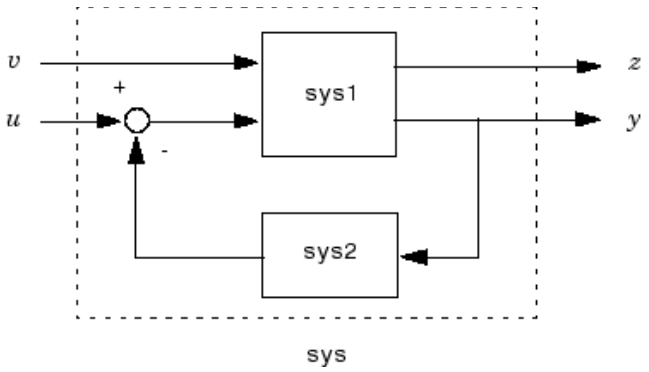


**Figure D.2** – General representation of the feedback of signals

The state-space system takes on the form

$$\dot{\boldsymbol{x}} = \mathbf{A}\boldsymbol{x} + \begin{bmatrix}\mathbf{B}_1 & \mathbf{B}_2\end{bmatrix}\begin{bmatrix}\boldsymbol{u}_1 \\ \boldsymbol{u}_2\end{bmatrix} \tag{D.2.1}$$

$$\begin{bmatrix}\boldsymbol{y}_1 \\ \boldsymbol{y}_2\end{bmatrix} = \begin{bmatrix}\mathbf{C}_1 \\ \mathbf{C}_2\end{bmatrix}\boldsymbol{x} + \begin{bmatrix}\mathbf{D}_{11} & \mathbf{D}_{12} \\ \mathbf{D}_{21} & \mathbf{D}_{22}\end{bmatrix}\begin{bmatrix}\boldsymbol{u}_1 \\ \boldsymbol{u}_2\end{bmatrix} \tag{D.2.2}$$

$$\text{so that } \boldsymbol{y}_1 = \mathbf{C}_1\boldsymbol{x} + \mathbf{D}_{11}\boldsymbol{u}_1 + \mathbf{D}_{12}\boldsymbol{u}_2 \tag{D.2.3}$$

$$\text{and } \boldsymbol{y}_2 = \mathbf{C}_2\boldsymbol{x} + \mathbf{D}_{21}\boldsymbol{u}_1 + \mathbf{D}_{22}\boldsymbol{u}_2 \tag{D.2.4}$$

$$\text{but } \boldsymbol{u}_2 = \boldsymbol{y}_2 \tag{D.2.5}$$

$$= \mathbf{C}_2\boldsymbol{x} + \mathbf{D}_{21}\boldsymbol{u}_1 + \mathbf{D}_{22}\boldsymbol{u}_2 \tag{D.2.6}$$

$$= (\mathbf{I} - \mathbf{D}_{22})^{-1}(\mathbf{C}_2\boldsymbol{x} + \mathbf{D}_{21}\boldsymbol{u}_1) \tag{D.2.7}$$

$$\text{Define } \mathbf{H} = (\mathbf{I} - \mathbf{D}_{22})^{-1} \tag{D.2.8}$$

$$\text{then } \boldsymbol{u}_2 = \mathbf{H}\mathbf{C}_2\boldsymbol{x} + \mathbf{H}\mathbf{D}_{21}\boldsymbol{u}_1 \tag{D.2.9}$$

Substitute this into Equations D.2.1 and D.2.3 to determine the new model.

$$\dot{\boldsymbol{x}} = (\mathbf{A} + \mathbf{B}_2\mathbf{H}\mathbf{C}_2)\boldsymbol{x} + (\mathbf{B}_1 + \mathbf{B}_2\mathbf{H}\mathbf{D}_{21})\boldsymbol{u}_1 \tag{D.2.10}$$

$$\text{and } \boldsymbol{y}_1 = (\mathbf{C}_1 + \mathbf{D}_{12}\mathbf{H}\mathbf{C}_2)\boldsymbol{x} + (\mathbf{D}_{11} + \mathbf{D}_{12}\mathbf{H}\mathbf{D}_{21})\boldsymbol{u}_1 \tag{D.2.11}$$

# Appendix E

# Lateral Aircraft Model with Manual Control Laws

$$\dot{\boldsymbol{x}} = \mathbf{A}\boldsymbol{x} + \mathbf{B}\boldsymbol{u}$$
$$\boldsymbol{y} = \mathbf{C}\boldsymbol{x} + \mathbf{D}\boldsymbol{u} \tag{E.0.1}$$

with

$$\mathbf{A} = \begin{bmatrix}
-0.0987 & 0.0488 & -0.992 & 0.0519 & 0 & -0.0002 & 0 & 0 & 0.0004 & 0 & 0 & 0 & 0 & 0 & 0 \\
-4.51 & -1.53 & 0.251 & 0 & 0 & -0.07 & 0 & 0 & 0.0037 & 0 & 0 & 0 & 0 & 0 & 0 \\
0.729 & -0.125 & -0.215 & 0 & 0 & -0.0023 & 0 & 0 & -0.0139 & 0 & 0 & 0 & 0 & 0 & 0 \\
0 & 1 & 0.0379 & 0 & 0 & 0 & 0 & 0 & 0 & 0 & 0 & 0 & 0 & 0 & 0 \\
0 & 0 & 1 & 0 & 0 & 0 & 0 & 0 & 0 & 0 & 0 & 0 & 0 & 0 & 0 \\
0 & 0 & 0 & 0 & 0 & 0 & 1 & 0 & 0 & 0 & 0 & 0 & 0 & 0 & 0 \\
0 & 0 & 0 & 531 & 0 & -43.5 & -6.9 & 43.5 & 0 & 0 & 0 & 9.28 & 9.9 & 0 & 0 \\
0 & 0 & 0 & 0 & 0 & 0 & 0 & -1 & 0 & 0 & 0 & 0 & 0 & 0 & 0 \\
0 & 0 & 0 & 0 & 0 & 0 & 0 & 0 & 0 & 1 & 0 & 0 & 0 & 0 & 0 \\
0 & 0 & 0 & 82.1 & 0 & 0 & 0 & 0 & -43.5 & -6.9 & -4.43 & 0 & -0.822 & 24.3 & 12.4 \\
0 & 0 & 0 & 0 & 0 & 0 & 0 & 0 & 0 & 0 & -3.33 & -3.33 & 0 & 0 & 0 \\
0 & 0 & 0 & 0 & 0 & 0 & 0 & 0 & 0 & 0 & 0 & 0 & 0 & 0 & 0 \\
0 & 573 & 0 & 0 & 0 & 0 & 0 & 0 & 0 & 0 & 0 & 0 & -10 & 0 & 0 \\
0 & 0 & 573 & 0 & 0 & 0 & 0 & 0 & 0 & 0 & 0 & 0 & 0 & -10 & 0 \\
573 & 0 & 0 & 0 & 0 & 0 & 0 & 0 & 0 & 0 & 0 & 0 & 0 & 0 & -10
\end{bmatrix}$$

$$\mathbf{B} = \begin{bmatrix} 0 & 0.0004 \\ 0 & 0.0033 \\ 0 & -0.0125 \\ 0 & 0 \\ 0 & 0 \\ 0 & 0 \\ 6.42 & 0 \\ 0 & 0 \\ 0 & 0 \\ 0 & 0 \\ -2.31 & 0 \\ 0.769 & 0 \\ 0 & 0 \\ 0 & 0 \\ 0 & 0 \end{bmatrix} \quad \text{with } \boldsymbol{x} = \begin{bmatrix} beta \\ p \\ r \\ phi \\ psi \\ Tch1 \\ Tch2 \\ beta_{slow} \\ x9 \\ x10 \\ x11 \\ dpm_{int} \\ p_{f_{d}eg} \\ r_{f_{d}eg} \\ beta_{f_{d}eg} \end{bmatrix} \qquad \boldsymbol{u} = \begin{bmatrix} dpm \\ drm \end{bmatrix} \quad \text{and} \quad \boldsymbol{y} = \boldsymbol{x}$$

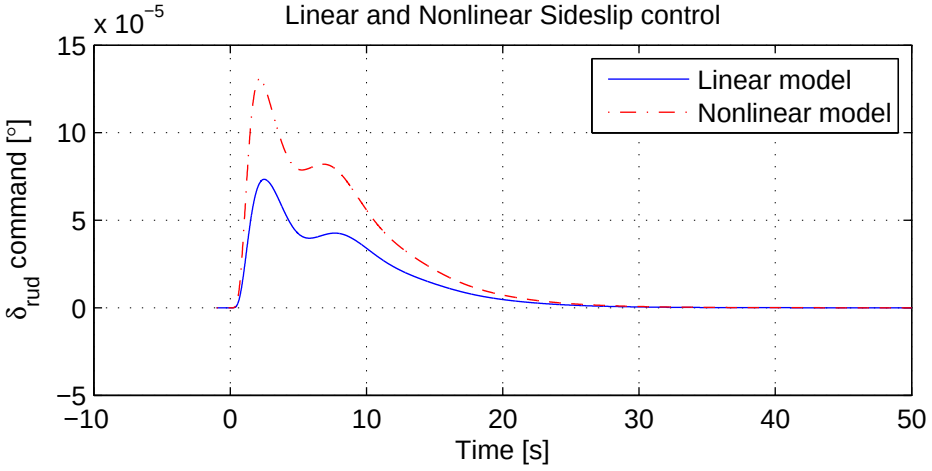


**Figure E.1** – Comparison of linear and non-linear FBW model side-slip control rudder command.

# Bibliography

[1] Engelbrecht, L.: Beyond the a400m. November 2009.
Available at: http://www.defenceweb.co.za/

[2] Anonymous: *Flying Qualities of Piloted Aircraft, MIL-HDBK-1797*. Department of Defense, USA, 1997.

[3] Peddle, I.K.: *Autonomous Flight of a Model aircraft*. Master's thesis, Stellenbosch University, 2005.

[4] S.C.Kriel: Explanation of nonlinear engine model derived from test data, 2010. Verbal and written communication about PhD research.

[5] Jaquet, C.: *Control surfaces in confined spaces: The optimisation of trailing edge tabs to reduce control surface hinge moments*. Master's thesis, Stellenbosch University, 2010.

[6] Rupert, F.: *Control of surfaces in confined spaces: Tab-aileron control system development*. Master's thesis, Stellenbosch University, 2010.

[7] Runhaar, A.: *Autonomous Airborne Refuelling: Relative State Estimation*. Master's thesis, University of Stellenbosch, 2011.

[8] Mao, W. and Eke, F.: A survey of the dynamics and control of aircraft during aerial refueling. *Nonlinear dynamics and systems theory*, p. 375, 2008.

[9] Refuelling boom news. *Journal of the Franklin Institute*, p. 106, 1950.

[10] Bloy, A., Lamont, P., Abu-Assaf, H. and Ali, K.: The lateral dynamic stability and control of a large receiver aircraft during air-to-air refuelling. *Aeronautical Journal*, vol. 90, pp. 237–243, 1986.

[11] Bloy, A., West, M. and Lea, K.: Lateral aerodynamics interference between tanker and receiver in air-to-air refueling. *Journal of Aircraft*, vol. 30, no. 5, pp. 705–710, 1993.

[12] Bloy, A. and Lea, K.: Directional stability of a large receiver aircraft in air-to-air refueling. *Journal of aircraft*, vol. 32, no. 2, pp. 453–455, 1995.

[13] Bloy, A. and Jouma'a, M.: Lateral and directional stability and control in air-to-air refuelling. *ARCHIVE: Proceedings of the Institution of Mechanical Engineers, Part G: Journal of Aerospace Engineering 1989-1996 (vols 203-210)*, vol. 209, no. 47, pp. 299–305, 1995.

[14] Bloy, A. and Khan, M.: Modeling of the receiver aircraft in air-to-air refueling. *Journal of Aircraft*, vol. 38, no. 2, pp. 393–396, 2001.

[15] Atilla Dogan, S.V. and Blake, W.: Modeling of aerodynamic coupling between aircraft in close proximity. *Journal of Aircraft*, vol. 42, pp. 941–955, 2005.

[16] Hansen, M. and Campos: The nasa dryden flight test approach to an aerial refueling system.

[17] Atilla Dogan, S.S. and Blake, W.: Flight control and simulation for aerial refueling. *AIAA Guidance, Navigation and Control Conference and Exhibit*, vol. 6264, pp. 1–15, 2005.

[18] Pachter, H. and Trosen: Design of an air-to-air automatic refueling flight control system using quantitative feedback theory. *International Journal of Robust and Nonlinear Control*, vol. 7, pp. 561–580, 1997.

[19] Bennington and Visser: Aerial refueling implications for commercial aviation. *Journal of Aircraft*, vol. 42, pp. 366–375, 2005.

[20] Cortet, E.: Flight control laws basic dynamics and limits. Tech. Rep., Airbus, 2008.

[21] Franklin, G., Workman, M. and Powell, D.: *Digital control of dynamic systems*. Addison-Wesley Longman Publishing Co., Inc., 1997.

[22] Etkin, B. and Teichmann, T.: *Dynamics of Flight: Stability and Control*, vol. 12. 1959.

[23] Gauvain, J.: Definition of an autonomous air-to-air refueling mode for the a330 mrtt during receiver's phases. Tech. Rep., Airbus France, 2007.

[24] Kriel, S.: The influence of receptacle position on control design, 2010. Verbal and written communication. Similar article submitted for peer review in 2011.